

https://dspace.org/

Three dimensional shock wave/boundary layer interactions

Mowatt, Sean

2011-11-02
http://hdl.handle.net/10539/10680

Downloaded from a DSpace repository. https://dspace.org/

THREE DIMENSIONAL SHOCK WAVE/BOUNDARY LAYER INTERACTIONS

Sean Mowatt

A dissertation submitted to the Faculty of Engineering and the Built Environment, University of the Witwatersrand, Johannesburg, in fulfilment of the requirements for the degree of Master of Science in Engineering

Johannesburg 2011

Declaration

I declare that this dissertation is my own unaided work. It is being submitted to the Degree of Master of Science to the University of the Witwatersrand, Johannesburg. It has not been submitted before for any degree or examination to any other University.

……..……..……..……..

(Signature of Candidate)

…….. day of…….. year……..

Abstract

An investigation into a three-dimensional, curved shock wave interacting with a three-dimensional, curved boundary layer on a slender body is presented. Three different nose profiles mounted on a cylindrical body were tested in a supersonic wind tunnel and numerically simulated by solving the Navier-Stokes equations. The conical and hemispherical nose profiles tested were found to generate shock waves of sufficient strength to separate the boundary layer on the cylinder, while the shock wave generated by the ogival profile did not separate the boundary layer. For the separated flow, separation was found to occur predominantly on the windward side of the cylinder with the lee-side remaining shielded from the direct impact of the incident shock wave. A thickening of the boundary layer on the lee-side of all the profiles was observed. In the conical and hemispherical cases this leads to the re-formation of the incident shock wave some distance away from the surface of the cylinder. A complex reflection pattern off the shock wave/boundary layer interaction (SWBLI) was also identified for the separated flow cases. For comparative purposes an inviscid simulation was performed using the hemispherical profile. Significant differences between the viscous and inviscid results were noted including the absence of the boundary layer leading to a simplified shock wave reflection pattern forming. The behaviour of the incident shock wave on the lee-side of the cylinder was also affected with the shock wave amalgamating on the surface of the cylinder instead of away from the surface as per the viscous case. Test data from the wind tunnel identified two separation lines present on the cylindrical surface of the hemispherical SWBLI generator. The pair of lines were not explicitly evident in the original CFD simulations run, but were later identified in a high resolution simulation.

Table of Contents

Declaration i

Abstract ii

Table of Contents iii

List of Figures vi

List of Tables xi

List of Symbols xii

1 Introduction 1

1.1 Background 1

2 Objectives 3

3 Literature Review 4

3.1 Oblique Shock Waves 4

3.2 Prandtl-Meyer Expansion Waves 6

3.3 Supersonic Flow Past Bodies of Revolution 6

3.3.1 Conical Bodies of Revolution 6

3.3.2 Ogival Bodies of Revolution 8

3.3.3 Hemispherical Bodies of Revolution 9

3.4 Shock Wave Reflections 9

3.5 The Structure of a Boundary Layer 11

3.6 Cylindrical Boundary Layers in Axial Flow 12

3.7 Shock Wave Interaction with a Cylindrical Body 13

3.8 Anatomy of Shock Wave/Boundary Layer Interactions 14

3.8.1 SWBLI with Separation – Strongly Interacting Flows 14

3.8.2 SWBLI without Separation – Weakly Interacting Flows 16

3.9 Three-Dimensional SWBLI Investigations 17
3.9.1 Conical Shock Wave/Planar Boundary Layer 17
3.9.2 Planar Shock Wave/Cylindrical Boundary Layer 19
3.9.3 Conical Shock Wave/Cylindrical Boundary Layer 21

4 Facilities and Methodology 24
4.1 Experimental Facilities and Methodology 24
4.1.1 Supersonic Wind Tunnel 24
4.1.2 Flow Visualisation – Schlieren Photography 34
4.1.3 Flow Visualisation - Oil Surface Flow Visualisation 36
4.1.4 Test Specimens 37
4.2 Numerical Facilities and Methodology 39
4.2.1 Mesh 39
4.2.2 Turbulence Model 42
4.2.3 Solver Type 42

5 Procedure 43
5.1 Pressurising the Storage Vessel 43
5.2 Pre-test Procedure 43
5.3 Wind Tunnel Blow Down 44
5.4 Wind Tunnel Shut Down 45
5.5 Precautions 45

6 Presentation and Analysis of Results 46
6.1 Pressure, Mach and Reynolds Number Traces 46
6.2 Experimental and Numerical Results 49
6.2.1 Overview 49
6.2.2 Flow Visualisation 50
6.2.3 Surface Flow Patterns 60
6.2.4 Surface Pressure Measurements 74
6.2.5 Lee-side Effects and Reflected Shock Wave Phenomena 80
6.2.6 High Resolution CFD – Hemisphere 99

7 Conclusions 108

8 Recommendations 111

9 References 112

Appendix A: Wind Tunnel Overhaul 114

A.1 February 2008 114

A.2 May 2008 115

A.3 July 2008 116

A.4 October 2008 117

A.5 December 2008 – January 2009 118

A.6 March 2009 119

A.7 August 2009 120

A.8 December 2009 122

Appendix B: Derivations 125

B.1 Derivation of Wind Tunnel Mach Number 125

B.2 Derivation of Wind Tunnel Reynolds Number 127

Appendix C: Test Model Manufacturing Drawings 130

List of Figures

Figure 3.1: Supersonic compressible flow over a concave corner 4

Figure 3.2: Supersonic compressible flow over a convex corner 6

Figure 3.3: Supersonic flow past a cone 7

Figure 3.4: Shock attachment criteria, (NACA, 1953) 8

Figure 3.5: Supersonic flow past an ogive 8

Figure 3.6: Supersonic flow past a hemisphere 9

Figure 3.7: Regular reflection wave configuration 10

Figure 3.8: Mach reflection wave configuration 10

Figure 3.9: The multi-layer structure within a boundary layer (Delery and Dussauge, 2009) 11

Figure 3.10: Three-dimensional shock wave reflection and diffraction around an oblique cylinder ... 14

Figure 3.11: Anatomy of a SWBLI with separation 15

Figure 3.12: Anatomy of a SWBLI without separation 17

Figure 3.13: Schematic of a conical shock wave interacting with a planar boundary layer 18

Figure 3.14: Schematic of a planar shock wave interacting with a cylindrical boundary layer 19

Figure 3.15: Experimental apparatus used by Kussoy et al (1980) 22

Figure 4.1: Schematic layout of the supersonic wind tunnel 24

Figure 4.2: Air dryer unit 26

Figure 4.3: Supersonic wind tunnel storage vessel 27

Figure 4.4: Sectional view of the settling chamber 27

Figure 4.5: Minimum Stagnation Pressure Curve 28

Figure 4.6: Schematic representation of the sliding block first throat 29

Figure 4.7: Mach number calibration curve 29

Figure 4.8: Pneumatic layout for the pressure control system 31

Figure 4.9: Pressure transducer calibration curve 34

Figure 4.10: Schlieren photography layout 35

Figure 4.11: Oil surface flow mixture when applied to the models 37

Figure 4.12: SWBLI generators and mounting bracket 38
Figure 4.13: Shock wave generator profiles 39
Figure 4.14: Mesh adaption scheme illustration 40
Figure 4.15: Star-CCM+ structured mesh 41
Figure 4.16: CFD symmetry plane illustration 41
Figure 6.1: Settling chamber and test section pressure curves during a blow-down (M = 3.0) 47
Figure 6.2: Mach and Reynolds number curves during a blow down (M = 3.0) 47
Figure 6.3: Meridian angle convention 49
Figure 6.4: SWBLI on the 0° meridian, Ogive 50
Figure 6.5: Magnified SWBLI on the 0° meridian, Ogive 50
Figure 6.6: Mach number contour line plots transverse to the axis of the cylinder, Ogive (sub-captions indicate the axial distances from the nose) 51
Figure 6.7: SWBLI on the 0° meridian, Cone 51
Figure 6.8: Magnified SWBLI on the 0° meridian, Cone 52
Figure 6.9: SWBLI on the 90° and 135° meridians, schlieren images, Cone 52
Figure 6.10: Mach number contour line plots transverse to the axis of the cylinder, Cone 53
Figure 6.11: SWBLI on the 0° meridian, Hemisphere 53
Figure 6.12: Magnified SWBLI on the 0° meridian, Hemisphere 54
Figure 6.13: Mach number contour line plots transverse to the axis of the cylinder, Hemisphere 54
Figure 6.14: SWBLI overview for the separated flows 55
Figure 6.15: Upstream influence of the SWBLI, Hemisphere 56
Figure 6.16: Variation of the nondimensional boundary layer parameter (ξ) along the length of the cylinder 58
Figure 6.17: Oil surface flow visualisation, Ogive 60
Figure 6.18: CFD Surface flow visualisation, Ogive 61
Figure 6.19: CFD Surface flow streamlines, Ogive 61
Figure 6.20: Oil surface flow visualisation, Cone 62
Figure 6.21: CFD surface flow visualisation, Cone 63

Figure 6.22: CFD Surface flow streamlines, Cone 63
Figure 6.23: Streamlines within the separated region, Cone 64
Figure 6.24: Oil surface flow visualisation, Hemisphere 65
Figure 6.25: Oil surface flow within the separated region, Hemisphere 66
Figure 6.26: Surface flow visualisation, Hemisphere 66
Figure 6.27: CFD Surface flow streamlines, Hemisphere 67
Figure 6.28: Streamlines within the separated region, Hemisphere 68
Figure 6.29: Separated region on the windward surface of the hemispherical SWBLI generator 69
Figure 6.30: Schematic illustration of the pressure gradients resulting from the SWBLI 71
Figure 6.31: Oil surface flow visualisation during a blow down, Hemisphere 72
Figure 6.32: Superposition of schlieren and oil surface flow images, Hemisphere 73
Figure 6.33: Surface pressure distribution, Ogive 74
Figure 6.34: Surface pressure distribution, Cone 75
Figure 6.35: Separation and attachment co-ordinates for SWBLI, Cone 75
Figure 6.36: Surface pressure distribution, Hemisphere 76
Figure 6.37: Separation and attachment co-ordinates for SWBLI, Hemisphere 76
Figure 6.38: Intersection of nose profile and cylindrical section forming an expansion fan 78
Figure 6.39: Secondary pressure bump location in pressure distribution curves 79
Figure 6.40: Separated region with meridian angles superimposed, Cone 80
Figure 6.41: Annotated Mach Number (M = 2.4) Iso-surface, Hemisphere 81
Figure 6.42: Mach number iso-surfaces 81
Figure 6.43: Viscous Simulation - Lee-side shock wave, Density gradient iso-surface, DG = 15000. 83
Figure 6.44: Viscous Simulation – Shock wave reflecting off surface of cylinder, Hemisphere 84
Figure 6.45: Sectioned iso-surfaces, Hemisphere 85
Figure 6.46: Effects of viscosity on the lee-side SWBLI, Hemisphere 86
Figure 6.47: Viscous simulation - density gradient contour lines 87
Figure 6.48: Viscous Simulation - sectioned density gradient iso-surfaces, DG = 10000 88
Figure 6.49: Inviscid simulation - density gradient contour lines 89

Figure 6.50: Inviscid Simulation - sectioned density gradient iso-surfaces, DG = 10000 90

Figure 6.51: Viscous Simulation - Annotated shock reflection structure, 32mm 91

Figure 6.52: Inviscid Simulation – Annotated shock reflection structure, 32mm 91

Figure 6.53: Comparison of SWBLI shock structure 93

Figure 6.54: Viscous Simulation – annotated Mach number and density gradient iso-surfaces, Hemisphere, 30mm 95

Figure 6.55: Viscous simulation - Mach number (M = 0.9) and sectioned density gradient (DG = 10000) iso-surfaces, Hemisphere 96

Figure 6.56: Lee-side (180° meridian) pressure distribution, Hemisphere 97

Figure 6.57: High resolution CFD SWBLI overview, Hemisphere 99

Figure 6.58: High resolution CFD Mach number contour line plots transverse to the axis of the cylinder, Hemisphere 100

Figure 6.59: High resolution CFD surface flow patterns, Mach number contours, Hemisphere 100

Figure 6.60: High resolution CFD annotated surface flow patterns, Mach number contours with measurement scale, Hemisphere 101

Figure 6.61: High resolution CFD surface flow patterns, Pressure (Pa) contours, Hemisphere 101

Figure 6.62: High resolution CFD streamlines within separated region, Hemisphere 102

Figure 6.63: Axial velocity variation within the boundary layer, 0° meridian, Hemisphere 103

Figure 6.64: Axial velocity variation within the boundary layer in the immediate vicinity of the SWBLI, 0° meridian, Hemisphere 103

Figure 6.65: Axial velocity variation within the boundary layer, 45° meridian, Hemisphere 104

Figure 6.66: Axial velocity variation within the boundary layer, 90° meridian, Hemisphere 104

Figure 6.67: Stagnation point caused by upstream influence 106

Figure 6.68: Superposition of the stagnation points and the flow within the separated region 107

Figure A 1: Sample image of the turbulent flow 114

Figure A 2: Sample image (shadowgraph) from xenon flash lamp 115

Figure A 3: Sample image from continuous projector lamp 116

Figure A 4: Mach number – throat veeder counter calibration curves 117

Figure A 5: Pressure trace from an unsuccessful test 118
Figure A 6: Pressure trace showing vibration (August 2009) 121
Figure A 7: Pressure trace showing vibration (December 2009) 122
Figure A 8: Processed pressure trace from successful wind tunnel test, Mach 3.0 123
Figure A 9: Mach and Reynolds number variation during a wind tunnel test, Mach 3.0 123

Figure C 1: Manufacturing drawings for the ogival SWBLI generator 131
Figure C 2: Manufacturing drawings for the conical SWBLI generator 132
Figure C 3: Manufacturing drawings for the hemispherical SWBLI generator 133

List of Tables

Table 4.1: Technical specification of the wind tunnel 25

Table 4.2: Technical specifications of the compressor 25

Table 4.3: Technical Specifications for the dryer 26

Table 4.4: Technical specifications of the storage vessel 26

Table 4.5: Specifications of the pressure control system 32

Table 4.6: Oscilloscope Specifications 33

Table 4.7: Pressure transducer details 33

Table A 1: Mesh specifications for turbulence reducing screens 114

Table A 2: Safety Solenoid Specifications (Circa 1982) 119

Table A 3: Pilot Valve Solenoid Specifications 119

Table A 4: Solenoid Specifications (Circa 2009) 120

Table A 5: Pilot Valve Solenoid Specifications (Circa 2009) 120

Table A 6: Repair Kit Contents for Main Control Valve 121

List of Symbols

θ	Wall turning angle [°]
β	Shock deflection angle [°]
M	Mach number
μ	Expansion fan turning angle [°], Dynamic viscosity [$kg.m^{-1}.s^{-1}$]
r	Radial distance measured from axis of cylinder / cone [mm]
U	Free-stream velocity [$m.s^{-1}$]
a	Radius of cylinder [mm], speed of sound [$m.s^{-1}$]
ν	Kinematic viscosity [$m^2.s^{-1}$]
Re	Reynolds number
φ	Meridian ray angle [°]
h	Enthalpy [J]
V	Volume [m^3]
T	Temperature [K]
P	Pressure [Pa]
C_P	Specific heat at constant pressure
ρ	Density [$kg.m^{-3}$]
R	Specific Rankine gas constant [$J.kg^{-1}.K^{-1}$]
γ	Ratio of specific heats
d	Diameter [mm]

Subscripts

1	Region of flow upstream of a shock wave
2	Region of flow downstream of a shock wave
MAX	Maximum value for the given parameter
C	Parameter pertaining to a cone
∞	Quantity pertaining to a free-stream value
T	Parameter pertaining to the wind tunnel settling chamber
0	Quantity pertaining to a reference value

1 Introduction

1.1 Background

Studies into shock wave/boundary layer interactions (SWBLI) pre-date the advent of supersonic flight. The earliest of these studies were conducted at transonic speeds and the SWBLI were difficult to investigate due to pockets of supersonic flow over the generally curved surfaces. To overcome these difficulties investigations were performed at supersonic velocities causing the shock waves to be the sole source of a pressure gradient. The geometries used in these studies (flat plates and external shock generators, flat plate ramps and steps, asymmetric bodies with flares and collars) provided information on parameters such as Mach and Reynolds numbers and the importance of the state of the incoming boundary layer. Several of these geometries are still used in modern day SWBLI studies (Dolling, 2001).

The knowledge and understanding harvested from SWBLI studies is vital given the omnipresent nature of SWBLI with high speed flight. Consider the example of two missiles flying in close proximity to each other, or that of the side intakes with centre bodies of a supersonic aircraft. Wing-body interactions, static probes in the presence of shock waves and even three-dimensional models inside closed supersonic wind tunnels are also applications where SWBLI exist (Migotsky and Morkovin, 1951).

SWBLI are generally viewed in a negative sense based on their adverse affect on various aerodynamic parameters and performance. Consider a turbulent boundary layer interacting with a shock wave; the shock wave enhances the production of turbulence which in turn amplifies the viscous dissipation resulting in a substantial increase in drag for profiles or wings. Should the shock wave be strong enough to cause the boundary layer to separate, the entire flow field can change dramatically with the formation of complex shock patterns and intense vortices. Shock-induced separation may even be severe enough to lead to large-scale unsteadiness, potentially damaging the vehicle and limiting its performance (Delery, 2001, Delery and Dussauge, 2009). The effects of SWBLI are not always negative. The increase in the fluctuation level stemming from the interaction can be used to enhance fuel-air mixing in the combustion chamber of scramjets. By combining a shock wave with boundary layer separation, the shock wave splits reducing the wave drag produced by the shock wave itself (Delery, 2001). Certain types of jet-engine exhaust nozzles' performance has also been enhanced by the correct use of SWBLI (Anderson, 2007).

Over the course of the last fifty years a firm understanding of SWBLI, both two- and three-dimensional, has been achieved. A majority of the studies undertaken have been limited to so-called

glancing or swept-shock interactions which covered a plethora of aerospace applications in the past (Gai and The, 2000). With the evolution of aerospace geometries and flight regimes, SWBLI will become more complicated and an understanding of a general interaction, between a three-dimensional non-planar shock wave and three-dimensional non-planar boundary layer for example, will be required (Dolling, 2001).

2 Objectives

The objectives of this study are to:

- Investigate and characterise the case of a curved shock wave interacting with a curved (cylindrical) boundary layer utilising experimental and numerical experimentation techniques.
- Determine the effect that varying the intensity of the incident shock wave has on the interaction.
- Characterise the flowfield on the leeward side of the cylinder with respect to the SWBLI.

3 Literature Review

A large portion of the standard material presented in the following section is taken from NACA Report 1135 (1953): Equations, tables and charts for compressible flow (NACA, 1953). Any other references used will be cited accordingly.

3.1 Oblique Shock Waves

When a supersonic compressible flow is turned through a concave corner an oblique shock wave occurs. For illustration purposes consider the situation depicted in Figure 3.1. An initially supersonic flow is turned through an angle of θ by means of a rigid wall. Due to the supersonic nature of the flow, the presence of the corner is not detected by the upstream flow and hence the flow changes its direction by means of an oblique shock wave. Since the flow is being turned through a concave corner, the oblique shock is a compressive shock wave. Compressive shock waves generate higher static temperatures and pressure while simultaneously causing a drop in Mach number.

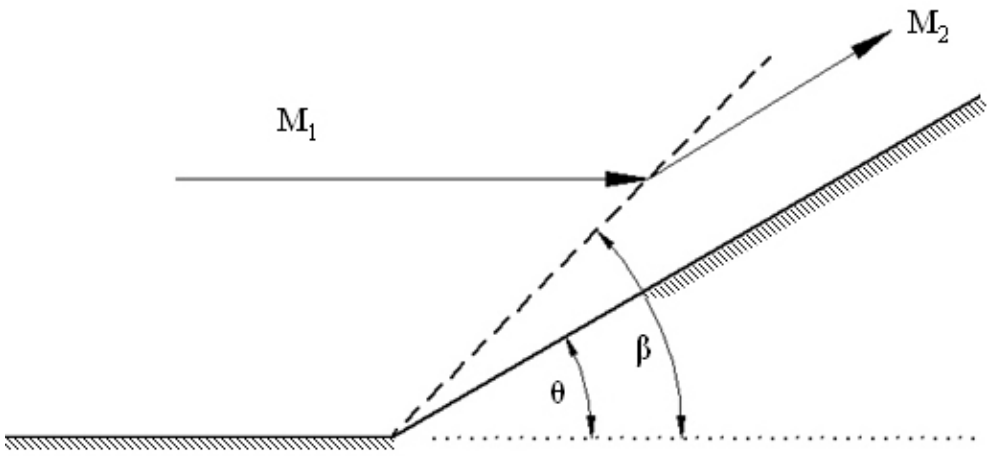


Figure 3.1: Supersonic compressible flow over a concave corner

The relationship between θ and β is given by the following equation:

$$\tan(\theta) = 2\cot(\beta)\left[\frac{M_1^2 \sin^2\beta - 1}{M_1^2\left(\gamma + \cos(2\beta)\right) + 2}\right] \qquad [3.1]$$

For every incoming Mach number (M_1) there exists a maximum deflection angle, θ_{max}. If the geometry dictates that the flow should be turned through an angle greater than θ_{max}, then no solution exists for a

straight oblique shock wave and instead the shock wave detaches and becomes curved in nature. The maximum values for θ are shown (as a function of Mach number) in Figure 3.4 for a conical shock wave (cone) and for a planar shock wave (wedge).

If the deflection is less than that of the prescribed maximum value, then two values of β exist; the strong shock and the weak shock. As the value for β increases the changes across the shock wave become more severe and the larger value for β is known as the strong shock. Conversely the smaller value of β is known as the weak shock. Generally the weak shock will occur in preference to the strong shock, however instances do occur where the back pressure is high enough and the strong shock is forced to occur. For strong shocks the downstream Mach number (M_2) is subsonic, whereas for weak shocks M_2 is supersonic unless the deflection angle is close to the maximum permissible value for that Mach number. For a fixed value of θ, if the free stream Mach number is decreased, the shock angle increases (for the weak shock solution). If the Mach number is decreased to a low enough value no solution at all will be possible and the shock wave will detach.

Calculation of the maximum turning angle is achieved by means of differentiating equation [3.1] with respect to β and noting that when shock detachment occurs $d\theta/d\beta = 0$. A complete derivation of the maximum turning angle can be found in countless papers and is deemed to be outside the scope of the current work.

When shock detachment occurs, the shock moves ahead of the corner (or wedge/cone) and immediately forms a normal shock leaving subsonic flow behind it. The normal shock is then curved implying that each streamline encounters a different shock angle and deflects accordingly. Based on the varying deflection of the shock wave, the property changes across it are no longer constant. Furthermore the flowfield behind the shock is not at constant entropy and is rotational (whereas the flow upstream of the detached plane oblique shock is irrotational in nature) and thus viscous stresses become important.

Consider the situation where two oblique shock waves intersect each other. After the intersection, the (oblique) shock waves continue as refracted shock waves which turn the flow in a different direction to that of the original deflection caused by the original oblique shock wave. The resulting flow (downstream of the intersection) is separated into two regions of parallel flow, each with a different entropy value.

3.2 Prandtl-Meyer Expansion Waves

When a compressible supersonic flow is turned through a convex corner, an expansion wave is formed and is shown schematically in Figure 3.2. This is the converse of an oblique shock wave which results from a flow turning through a concave corner (as described previously).

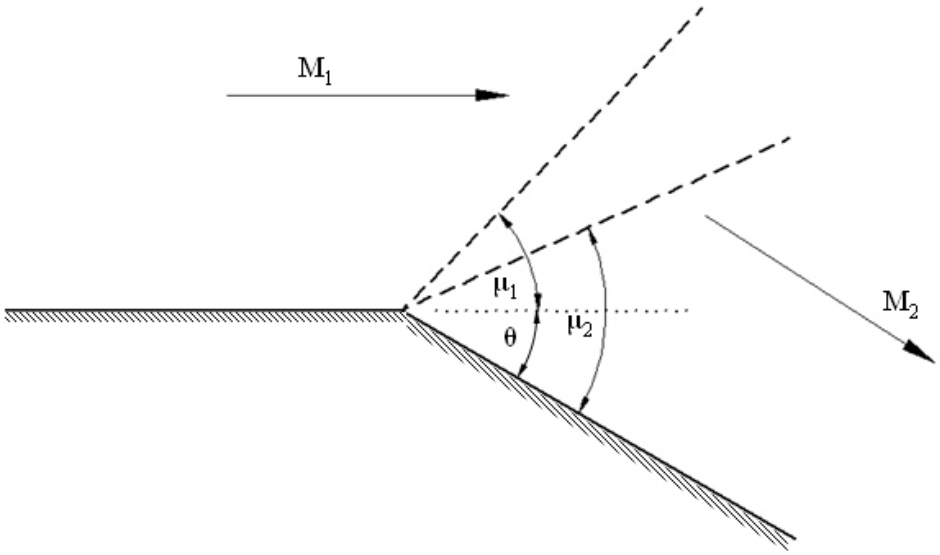


Figure 3.2: Supersonic compressible flow over a convex corner

Expansion waves differ from oblique shock waves in their effect on the parameters of the gas through the wave. Firstly, the Mach number of the flow increases through the wave, i.e. $M_2 > M_1$. Secondly the static properties of the gas decrease through an expansion wave. Thirdly, the expansion fan (the region from where the flow first begins to turn through a convex angle to where it settles to a final deflection angle, i.e. the region bounded by μ_1 and μ_2 in Figure 3.2) is a continuous region comprising of an infinite number of Mach waves. The streamlines through the expansion fan are smooth curved lines. Finally, the expansion occurs through a continuous succession on Mach waves and is therefore isentropic. As is the case with oblique shock waves, a maximum turning angle also exists for expansion waves; however the derivation of such an equation is not relevant to the current study.

3.3 Supersonic Flow Past Bodies of Revolution

3.3.1 Conical Bodies of Revolution

Consider the case of a sharp solid cone with a semi-vertex angle of θ_C in a supersonic free stream as shown in Figure 3.3. A bow shock forms on the vertex of the cone, maintaining a fixed position relative to the body if the flow is steady, and remains attached as long as θ_C is lower than a prescribed

maximum value (θ_{MAX}). If the bow shock is attached to the vertex of the cone, then the shock too has the form of a circular cone.

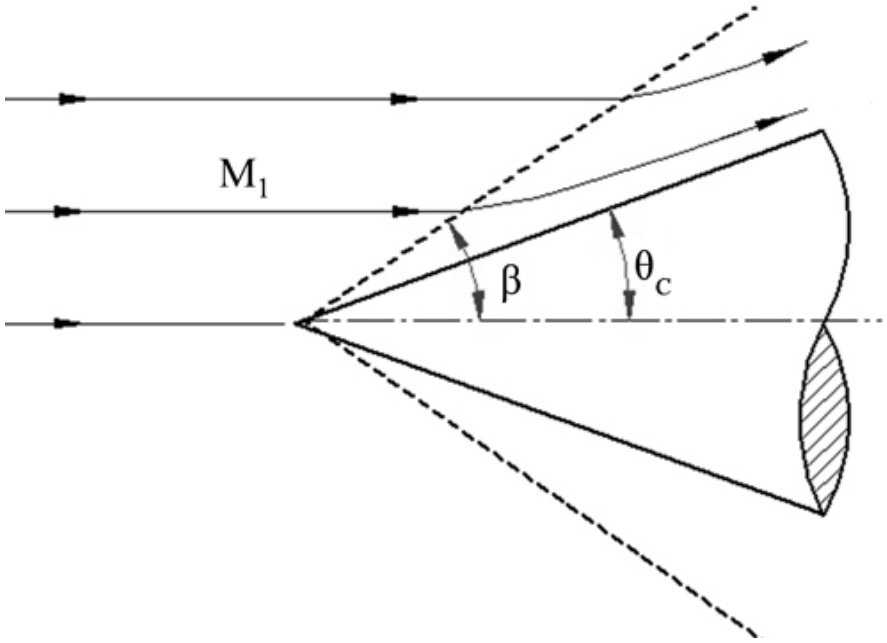


Figure 3.3: Supersonic flow past a cone

Inspection of the streamlines illustrated in Figure 3.3 shows an initial (discontinuous) deflection across the shock wave, before the streamlines curve continuously downstream of the shock wave to satisfy the continuity equation. The streamlines ultimately become parallel (asymptotically) to the surface of the cone (Irving Brown, 2002). The resultant flow between the shock wave and the surface of the cone changes from a uniform flow parallel to the free stream, to one which is irrotational and conical in nature.

The flow between the shock wave and the surface of the cone is characterised by a series of concentric surfaces. On each of these surfaces the flow quantities (pressure, density and temperature for example) remain constant, and thus depend only on one space variable. The transition across the shock wave is governed by the oblique shock relations described in section 3.1 and is followed by a continuous isentropic compression to surface conditions. This isentropic compression results in the shock wave detaching from the vertex of the cone at a much larger value for θ_C (for a given Mach number) compared to that of a wedge. The variation of θ_{MAX} with cone/wedge angle and free stream Mach number is shown in Figure 3.4 (NACA, 1953). Also shown is the condition for the transition from supersonic to subsonic flow along the surface of the cone (ignoring boundary layer effects). The increase in detachment angle of the cone compared to that of a wedge for any given Mach number is also shown.

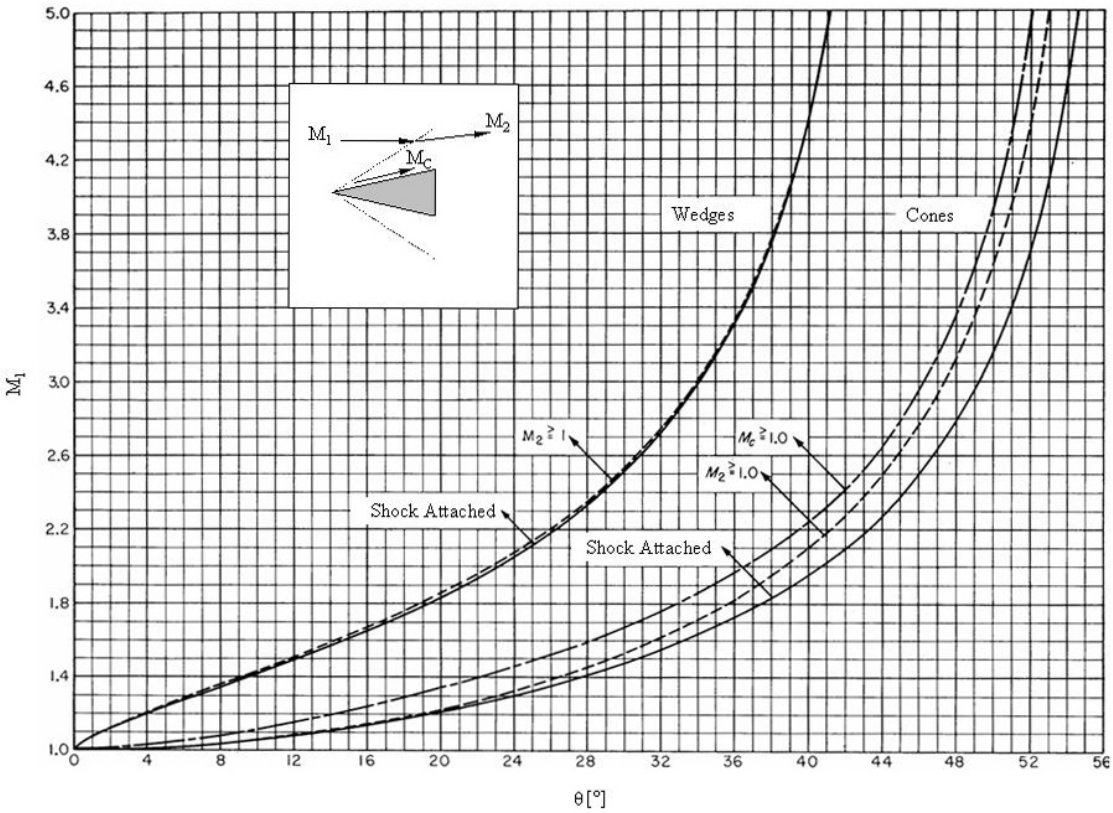


Figure 3.4: Shock attachment criteria, (NACA, 1953)

3.3.2 Ogival Bodies of Revolution

The flowfield around an ogival nose profile is largely the same as the conical case above and is shown schematically in Figure 3.5. The separation and attachment criteria for the conical profiles (Figure 3.4) can also be applied to an ogival profile.

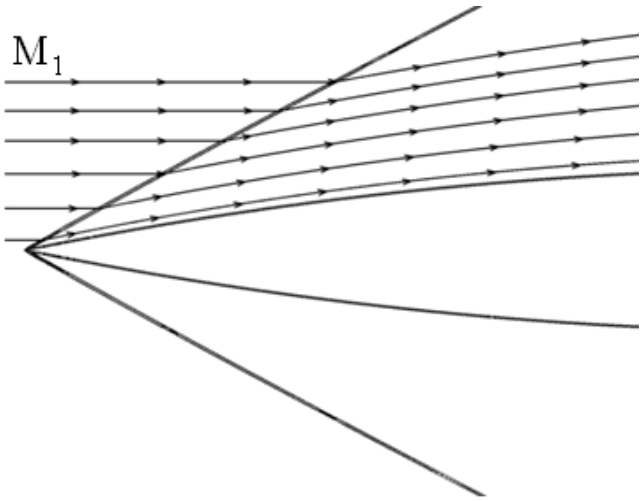


Figure 3.5: Supersonic flow past an ogive

3.3.3 Hemispherical Bodies of Revolution

The fundamental differences between a conical or ogival flowfields and a hemispherical flowfield is i) the detachment of the incident shock wave from the leading edge of the profile and ii) the presence of a stagnation bubble at the leading edge of the nose profile. The flowfield around the hemisphere is shown schematically in Figure 3.6.

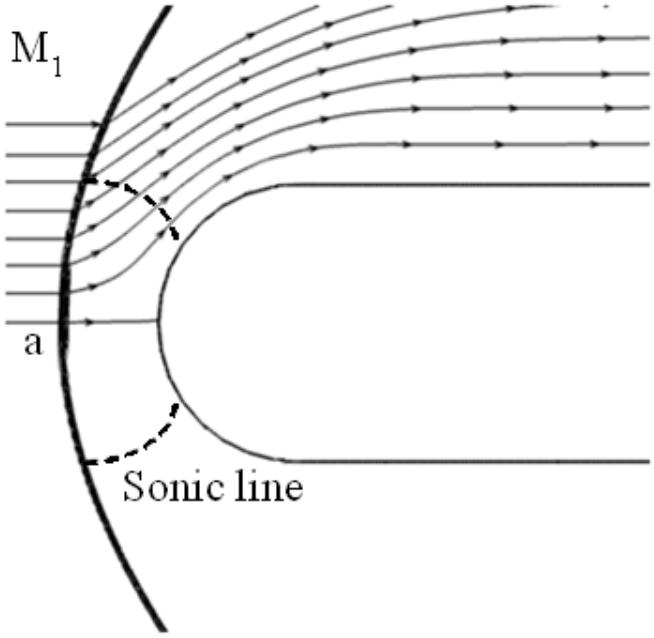


Figure 3.6: Supersonic flow past a hemisphere

The sonic line demarcates the stagnation bubble in which the Mach number is less than 1. At Point 'a' on Figure 3.6 the shock wave is normal to the upstream flow and hence corresponds to a normal shock wave. Away from point 'a' the shock wave becomes curved and weaker.

3.4 Shock Wave Reflections

Consider a shock wave propagating through one medium and encountering another medium obliquely. The result will be a reflection of the shock wave known as an oblique shock wave reflection (Zucrow and Hoffman, 1976).

These reflections will generally be categorised as either regular reflections (RR) or irregular reflections (IR). The RR case consists of two shock waves, the incident (i) and the reflected (r) waves, which meet on the reflecting surface at the reflection point (R), as shown in Figure 3.7. In the IR case, a subset of IR known as Mach Reflection (MR) is shown in Figure 3.8. For the MR case a three-wave system is established consisting of the incident wave (i), reflected wave (r), a Mach stem (m) and a

slipstream (s). These four discontinuities all meet above the reflecting surface at the triple point (T). The point at which the Mach stem touches the reflecting surface is called the reflection point (R).

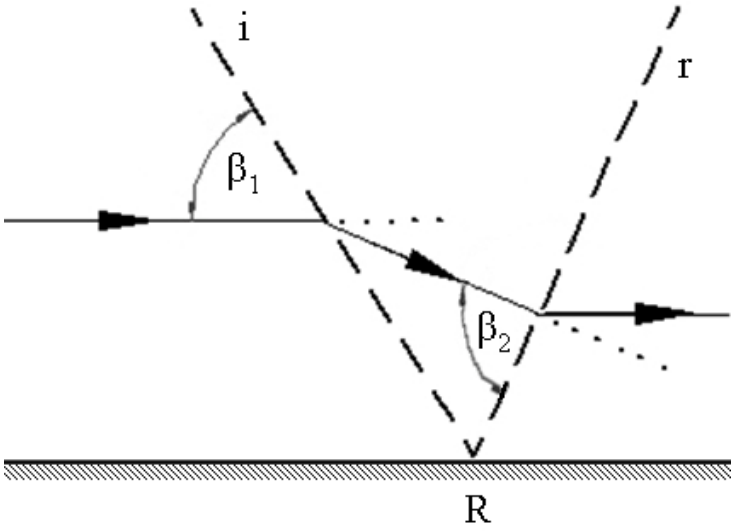


Figure 3.7: Regular reflection wave configuration

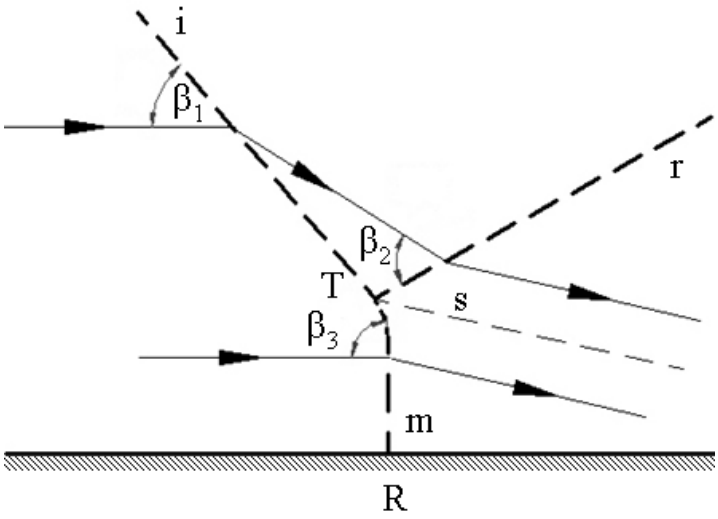


Figure 3.8: Mach reflection wave configuration

The transition from RR to MR occurs when the strength of the incident shock wave increases, causing the strength of the reflected shock to simultaneously increase, to a point at which the reflected shock can no longer deflect the flow parallel to the wall. This phenomenon is similar to the issue of shock detachment described in section 3.1. The point at which the aforementioned occurs is called the 'Transition Point' and the criteria governing the onset of MR are known as the 'Transition Criteria' (Scott, 1994). Both of these conditions have been the study of many studies and are considered to be outside the scope of this work.

When two incident shocks of exactly the same strength reflect off each other, the overall flow field is identical to the case described above (an incident shock wave reflecting of a solid surface); however the issue of SWBLI along the reflecting surface can be negated. Instead of a solid reflecting surface, the incident shock waves simply reflect off each other along the line of symmetry of the interaction (Scott, 1994). The criteria for RR relaxes (with respect to maximum turning angle) with increasing free stream Mach number and a dual solution domain exists in which either RR or MR can occur. Hysteresis effects determine which of the reflections occurs. If the dual solution domain is approached from the RR domain, then RR will occur in the dual solution domain until the MR threshold is crossed. Conversely, if the dual solution domain is approached from the MR domain, then MR will persist until RR occurs.

3.5 The Structure of a Boundary Layer

The flow within a boundary layer along a solid surface can be viewed as a multi-layered structure as shown in Figure 3.9 below (Delery and Dussauge, 2009):

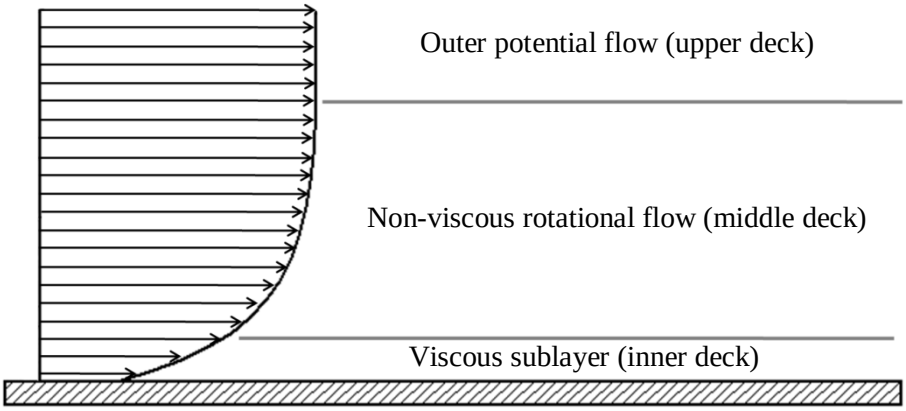


Figure 3.9: The multi-layer structure within a boundary layer (Delery and Dussauge, 2009)

Each of the three layers in the sketch responds differently when acted upon by a rapid pressure gradient (such as a shock wave). Some of the basic characteristics of the different layers are as follows (Delery and Dussauge, 2009):

1. The outer inviscid layer (labelled the upper deck in Figure 3.9) is usually irrotational (i.e. isentropic) and thus obeys the Euler and potential equations. There are instances where this layer is rotational such as downstream of the curved shock wave formed ahead of a blunted leading edge/nose. In this instance what is referred to as an ‘entropy layer’ is formed.
2. Closer to the surface a region exists where the flow can be considered inviscid but still rotational (labelled the middle deck in Figure 3.9). In this part of the flow the viscosity contributed to entropy creation which consequently leads to the creation of vorticity. This layer

is a region where the stagnation pressure is variable but the stagnation temperature is nearly constant.

3. The third layer, or inner deck, is in direct contact with the wall and is necessary for the transition between the middle deck and the surface. This viscous layer is required to avoid any inconsistencies as it is not possible for an inviscid flow to reduce its velocity without a corresponding rise in static pressure. The stagnation pressure and the static pressure are equal at the wall due to the velocity at the wall being equal to zero – a requirement of the no-slip (friction) condition.

3.6 Cylindrical Boundary Layers in Axial Flow

Boundary layers forming along flat plates have been researched extensively and are very well understood. The simplest example of this is the Blasius case in which the flow is over a flat plate aligned with the flow in which the pressure gradient is zero. For the case of cylindrical boundary layers, that level of research and understanding is not as well developed. Consider a solid circular cylinder axially aligned to the free stream. The circular profile of the cylinder will require the flow to adjust to the presence of the cylinder and a nonzero pressure gradient will be established which decays asymptotically along the length of the cylinder (Tutty, Price and Parsons, 2002). Cylindrical boundary layers, despite their relatively simple geometries do not have a universal similarity solution due to the variation in space co-ordinates used within the boundary layer. The two choices for the space geometries are either *x, y* or *x, r*. The choice of co-ordinates is dependant on the thickness of the boundary layer; if the boundary layer thickness is small in comparison with the radius if the cylinder (known as the Blasius case) then the *x* and *y* co-ordinates should be selected, while if the thickness of the boundary layer is large in comparison with the radius of the cylinder (known as the needle case) then *x* and *r* should be utilised (Sawchuk and Zamir, 1992).

Quantifying the limits in a more tangible manner can be done by means of a non-dimensional parameter from the work of Sawchuk and Zamir (1992):

$$\xi = 4\left(\frac{x}{a}\right)^{1/2}\left(\frac{Ua}{\nu}\right)^{-1/2} = 4\left(\frac{x}{a}\right)^{1/2}\left(\mathrm{Re}\right)^{-1/2} \qquad [3.2]$$

As the value of ξ tends to infinity the needle limit is approached, while as ξ tends to zero the Blasius limit is approached.

Near the front of the cylinder the boundary layer is very thin when compared to the diameter of the cylinder and the boundary layer takes on characteristics very similar to a Blasius case. This is evident

upon inspection of equation [3.2]; the nearer the front of the boundary layer (i.e. the smaller the x value) the smaller the value of ξ and hence the layer tends towards the Blasius case. Further downstream the Blasius solution begins to become inadequate as the curvature of the boundary layer becomes prominent and a series of numerical methods are required to fully characterise the boundary layer (Tutty et al., 2002). The boundary layer that forms on a cylinder is generally thinner than that of a Blasius boundary layer forming on a flat plate and contains smaller radial velocities. The reduced boundary layer thickness on the cylinder causes the skin friction value to be larger. It has been shown that as one moves down the surface of a cylinder, the skin friction can be as much as 20 times higher than it is on a flat plate. It is worth noting that this value is heavily dependant on both the definition of the characteristics selected for the Reynolds number, as well as the axial location of the calculation (Sawchuk and Zamir, 1992). The combination of the thinner boundary layer and higher skin friction value suggests that the boundary layer on a circular cylinder is a very stable one. Tutty et al. (2002) have indeed shown that for low Reynolds numbers the flow within the cylindrical boundary layer is unconditionally stable.

3.7 Shock Wave Interaction with a Cylindrical Body

The reflection and diffraction of shock waves off and around wedges and corners is very well documented due to the many works on the subject over the years. In contrast relatively few studies have been undertaken into the interaction of a shock wave with a cylinder. Due to this limited availability, at the time of writing no study was found that detailed the interaction of conical shock wave and a cylinder – the underlying geometry of the current study. As a result only studies with geometries that roughly approximated that of the current work were available for comparison. One such case was the interaction of a three-dimensional unsteady shock wave with an oblique cylinder (Timofeev et al., 1997). This investigation involved the numerical and experimental investigation of an initially plane shock wave reflecting of an oblique cylinder. The Mach number of the incident shock wave varied from 1.2 to 3. Due to the high Reynold number of the flow an Eulerian inviscd gas model was used for the numerical simulations.

The shocked flow around the cylinder was found to be a truly three-dimensional, unsteady flow with quantitive parameters that differed from the associated planar and axisymmetrical cases. Both regular and Mach reflection was found to occur simultaneously on the surface of the cylinder with a complex three-dimensional Mach stem of variable curvature. The triple point line was found to be tangential to the cylinder wall resulting in difficulties (both experimentally and numerically) in measuring the exact location of the transition point. A plan view of the flow development is given schematically in Figure 3.10 below (Timofeev et al., 1997):

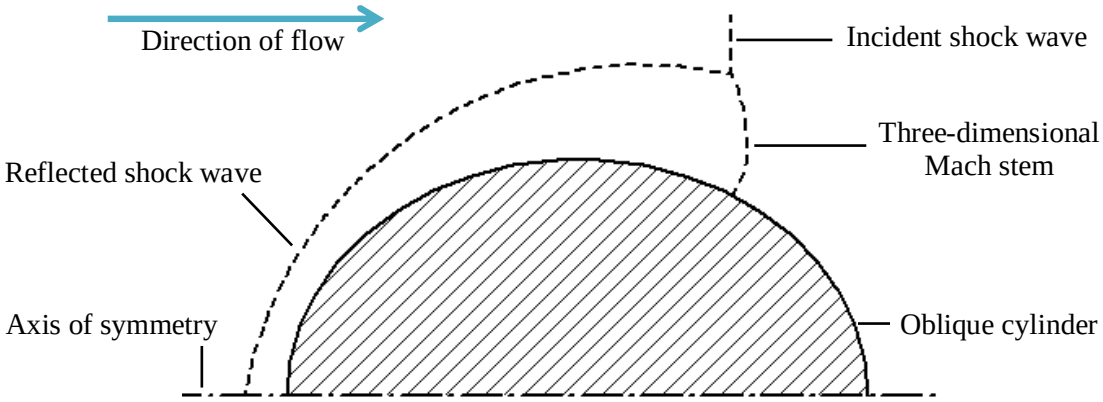


Figure 3.10: Three-dimensional shock wave reflection and diffraction around an oblique cylinder

3.8 Anatomy of Shock Wave/Boundary Layer Interactions

3.8.1 SWBLI with Separation – Strongly Interacting Flows

Consider a supersonic flow over a surface, along which a boundary layer has formed, wherein an oblique shock wave impinges on that surface (see Figure 3.11, Anderson, 2007). At the point of impingement, the boundary layer would experience an infinitely large adverse pressure gradient arising from a discontinuous pressure increase. This pressure discontinuity is a result of the combination of the pressure increase across both the incident and reflected shock waves at the point of impingement. When a boundary layer experiences a large pressure gradient it separates from the surface along which it had been hitherto attached. The resultant flow field in the vicinity of the shock wave impingement becomes one of mutual interaction between the shock wave and boundary layer (Anderson, 2007). It is worth noting at this point that the behaviour of the separating boundary layer in a compressible flow is largely the same as that of an incompressible separation. It has even been suggested that shock-induced separation is merely the compressible facet of a general separation phenomenon, with the shock being the epiphenomenon of the process. The most prominent feature of the shock separation is the associated shock patterns and their affect on the entire flow field (Delery, 2001).

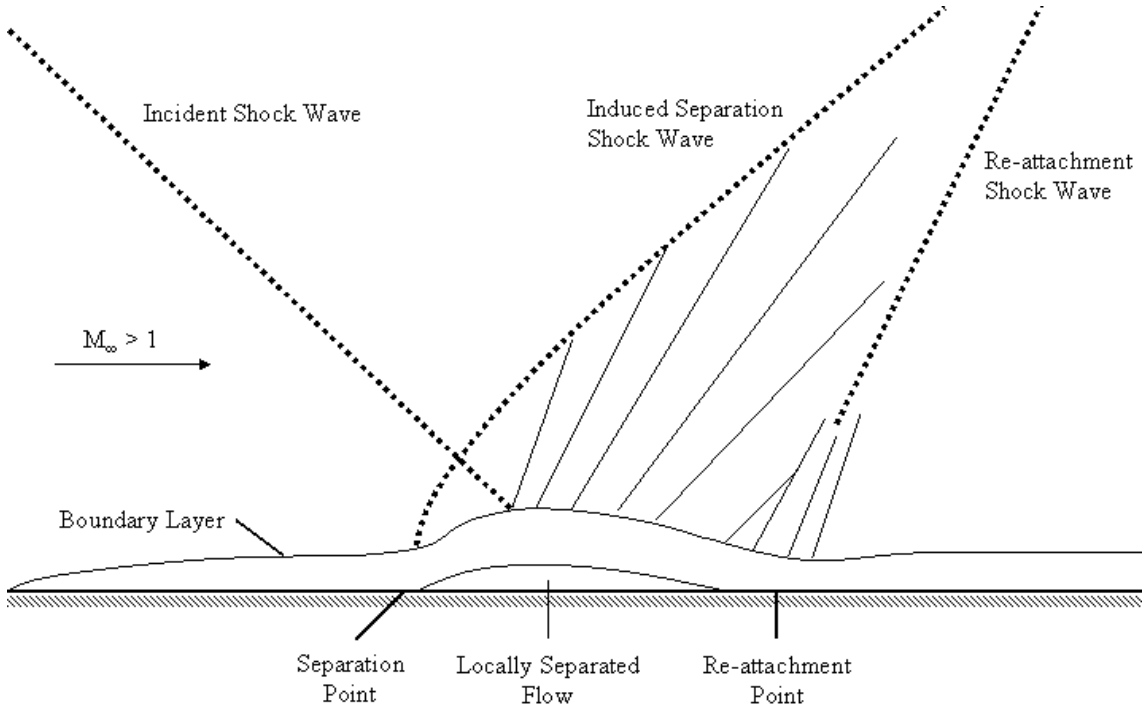


Figure 3.11: Anatomy of a SWBLI with separation

Due to the supersonic nature of this flow, the velocity profile of the boundary layer will be subsonic near the wall and supersonic near the outer edge. As the incident shock impinges on the boundary layer, a large pressure gradient is formed by the pressure rise across the shock. This pressure gradient causes the boundary layer to (locally) separate from the surface. The high pressure gradient also causes the high pressure behind the shock to propagate upstream through the subsonic portion of the boundary layer, and hence the separation occurs upstream of the theoretical inviscid flow impingement point. The separated boundary layer then deflects the external supersonic flow through a concave angle and thus causes a second shock wave, labelled in the Figure 3.11 as the induced separation shock wave. Subsequently, the separated boundary layer turns back towards the plate and reattaches to the plate at some downstream location. This reattachment also induces a shock wave called the reattachment shock. In the region between the separation shocks, the supersonic flow is tuning back towards the plate and an expansion fan is generated. At the point of reattachment the boundary layer has become relatively thin, the pressure is high and thus a region of high local aerodynamic heating is formed. Further away from the plate and the interaction region the separation and reattachment shocks will merge together and the flowfield resembles an inviscid scenario similar to that of Figure 3.7 (Anderson, 2007).

The scale and severity of the interaction is largely dependant on the nature of the incoming boundary layer, i.e. is the boundary layer laminar or turbulent? A laminar boundary layer will generally separate more easily than a turbulent boundary layer, thus a laminar interaction will occur more readily with

more severe consequences than the turbulent interaction. The overall qualitative aspects of both types of boundary layer remain unchanged (Anderson, 2007).

Parameters affected by SWBLI include the pressure, shear stress and heat-transfer distributions. On the subject of the latter, local heat-transfer rates have shown to increase substantially at the reattachment point and at hypersonic speeds can grow to be an entire order of magnitude larger than at neighbouring locations. As an example of the effect on the pressure distribution along a flat plate, consider the work of Baldwin and Lomax (1978). With an external Mach number of 3 ahead of the incident shock, it was found that pressure increase occurred as much as four times the boundary layer thickness ahead of the theoretical inviscid impingement point. With respect to shear stress along the surface it was observed that in the region of separated flow the shear stress value became small and reversed its direction due to the re-circulating flow.

3.8.2 SWBLI without Separation – Weakly Interacting Flows

When the incident shock wave impinging on the boundary layer lacks the necessary intensity to separate the boundary layer, a weak interaction occurs as sketched in Figure 3.12. In this instance the incident shock wave penetrates the boundary layer and progressively bends towards the surface due to the local decrease in Mach number. Correspondingly the shock wave weakens and eventually disappears when it reaches the sonic line within the boundary layer. The pressure rise across the incident shock is felt upstream in the same manner as for the SWBLI with separation case described in section 3.8.1 above. The overall shock pattern that results does not depart from the inviscid solution (a simple incident-reflection pattern) dramatically and hence the interaction is said to be a weak interaction insofar as the flow is weakly affected by the viscosity of the air (Delery and Dussauge, 2009). The adverse pressure gradient across the incident shock wave dilates the subsonic portion of the boundary layer which acts as a ramp for the supersonic outer region of the boundary layer. This ramp forms compression waves which ultimately coalesce to form the reflected shock wave shown in Figure 3.12.

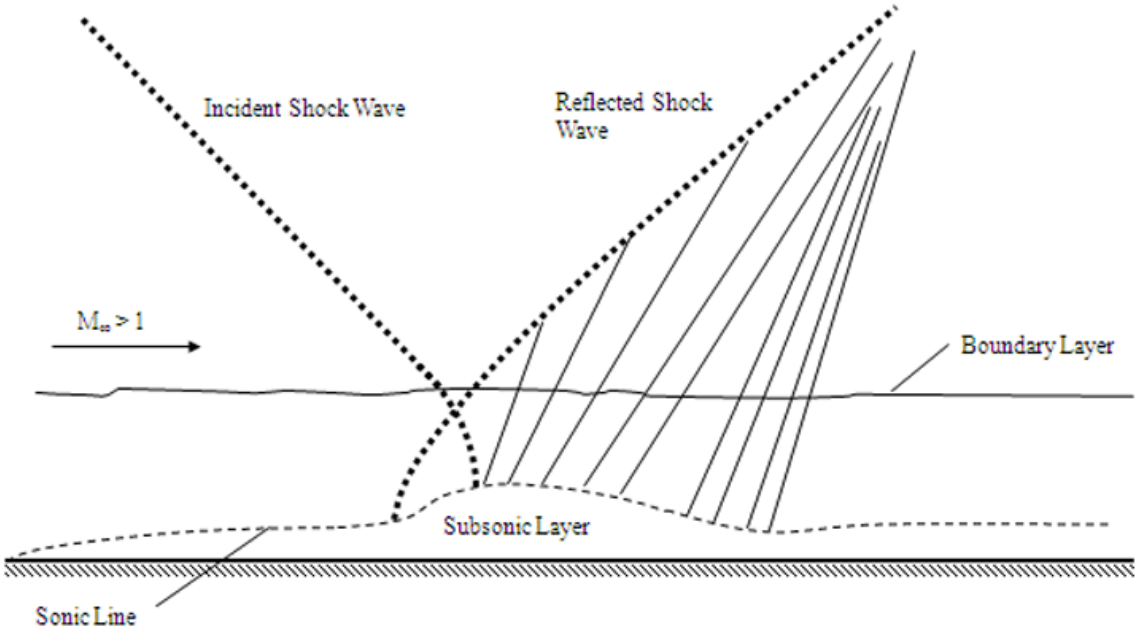


Figure 3.12: Anatomy of a SWBLI without separation

3.9 Three-Dimensional SWBLI Investigations

As highlighted previously, the investigations into three-dimensional SWBLI that have been undertaken have generally been limited to glancing or swept-shock interactions, whereby a shock generator is used to generate a planar shock that sweeps across a planar boundary layer. These types of configurations are by definition three-dimensional since the interaction will take place in three mutually perpendicular directions; however the shock waves and boundary layers involved are still planar in nature.

3.9.1 Conical Shock Wave/Planar Boundary Layer

An interesting three-dimensional SWBLI is that between a conical shock wave and a planar boundary layer, as investigated by Gai and Teh (2000) and Panov (1968) and illustrated in Figure 3.13. It is of interest to note that due to the underlying similarities in their geometries, it has been proposed that a conical shock wave interacting with a planar boundary layer, and a planar shock wave interacting with a cylindrical boundary layer are identical, albeit in the absence of a boundary layer (Migotsky and Morkovin, 1951). Gai and Teh (2000) testing at a Mach number of 2.0 initially found that as the strength of the shock wave increased (in this instance an increase in shock strength was achieved by increasing the cone angle of the shock generator as well as the height of the cone above the flat plate), the reflected shock's origin moves further upstream with respect to the rest of the interaction. This movement of the reflected shock was attributed to an increase in size (again proportionately to the strength of the shock wave) in the separation bubble occurring within the boundary layer. The

reflected shock was also found to be the result of the coalescence of the compression waves within the boundary layer and formed ahead of the incident shock. All of the aforementioned features closely matched those identified by Panov (1968) in an earlier study into SWBLI using the same conical shock and planar boundary layer configuration at Mach 2.87.

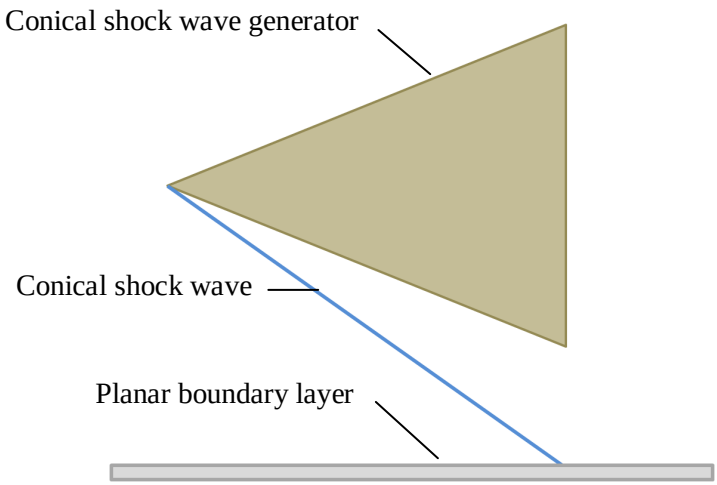


Figure 3.13: Schematic of a conical shock wave interacting with a planar boundary layer

The surface oil-flow patterns presented in Gai and Teh's work showed a curved separation that reduced in size as the interaction weakened moving away from the plane of symmetry of the interaction. It was also observed that for larger cone half-angles (26° for example) there existed not only a primary separated zone, but also a secondary separation embedded within the primary separation zone. No definite explanation was offered for this phenomenon. For smaller cone angles (16°) no separation lines were noted on the plate. When separation did occur it was observed to be curved in nature. The axis of the curvature was normal to the flow direction at the plane of symmetry of the interaction, and bended in a spanwise direction until ultimately becoming parallel to the freestream flow. It was this curvature that Gai and Teh attribute to the generation of a horseshoe vortex forming on either side of the axis of symmetry.

Gai and Teh (2000) also found that the cone half-angle that would lead to the onset of incipient separation could be estimated by normalising the measured separation length with respect to the height of the boundary layer. Plotting the results as a function of cone half-angle and extrapolating the data to where the normalised separation length is equal to zero suggests that incipient separation would occur for a cone half-angle of approximately 17°. Doubling this gives a full cone angle of 35° and a corresponding pressure ratio of 1.4. While this latter value was found to be lower than that for a swept-shock and/or two-dimensional SWBLI, it is consistent with the fact that in general the incipient separation pressure in three-dimensional separation is less than that of its two-dimensional counterpart. Another parameter affecting the incipient separation pressure in this particular

configuration is that of the cone height above the flat plate. This was initially proposed by Panov (1968) and acknowledged by Gai and Teh (2000), who stated that for a two dimensional interaction, the critical pressure ratio for a constant Mach number is independent of the height of the shock generator, whereas for a three-dimensional case varying the height does have an effect on the critical pressure.

Surface pressure measurements were also taken by Gai and Teh (2000) by means of an interaction grid consisting of pressure orifices spaced between 2mm and 4mm apart. It was noted that even at the minimum pitch of the pressure orifices (2mm), the resolution of the grid was still of the order of the boundary layer thickness (2.4mm) and hence too coarse to capture some of the finer aspects of the SWBLI. In general the surface pressure data gathered at the various stations showed a rise from the reference free stream pressure, to a maximum value after passing through the incident-reflected shock system at the surface of the plate. A decrease in the peak pressure values with spanwise position was noted as was the lack of a pressure plateau – a characteristic often associated with flow separation.

3.9.2 Planar Shock Wave/Cylindrical Boundary Layer

Another type of SWBLI that has been investigated is that of an interaction between planar shock waves and cylindrical bodies as shown in Figure 3.14. Such a study was undertaken by Morkovin et al. (1952) investigating both a laminar and turbulent boundary layer at a Mach number of 1.90. Of primary interest in this study was the anomalous reflection patterns predicted by the non-viscous theory; however the more general flow features and pressure distributions associated with SWBLI were also examined.

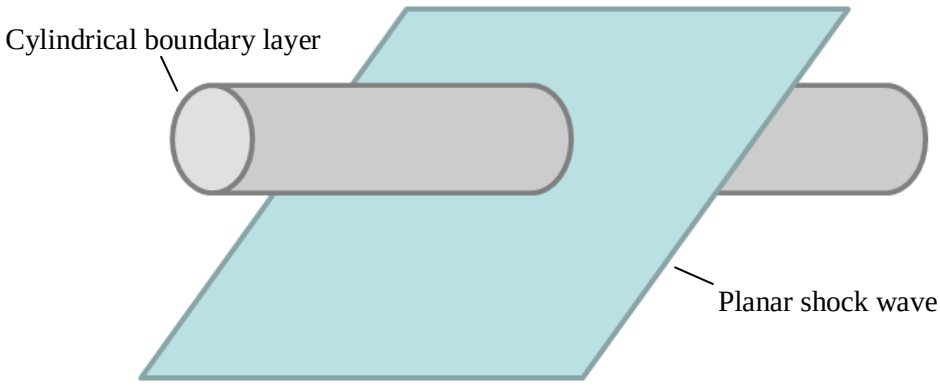


Figure 3.14: Schematic of a planar shock wave interacting with a cylindrical boundary layer

On the subject of the flow features it was found that boundary layer cross-flows (boundary layer flow across meridional planes) were ubiquitous for all configurations examined and result from the pressure gradient formed by the impinging shock wave. Boundary layer cross-flows modify the

effective boundary (or shape) of the three-dimensional surface. The cross-flows are an important aspect of the three-dimensional nature of the problem, and thin the boundary layer downstream from the point of incidence (Morkovin et al., 1952).

The pressure distributions recorded by Morkovin et al. show that the net pressure rise resulting from the SWBLI is smaller for a thicker boundary layer with the effects of the net pressure rise felt further upstream. For a thinner boundary layer the converse is true. This phenomenon is due to the subsonic layer that exists within the boundary layer; a thicker boundary layer will have a thicker subsonic layer and thus will allow more information pertaining to the adverse pressure gradient etc., to be propagated upstream. It was also found that the maximal values of the net pressure rises fell short of those predicted by theory. This anomaly was ascribed to the thickness of the boundary layer which could accommodate large scale radial pressure gradients and to the three-dimensional effects of the boundary layer cross-flows (Morkovin et al., 1952).

One of the most notable and important features of the pressure distributions was the bump just forward of a pre-defined datum point for the strong shock case. The pre-defined datum point in this case was the pressure orifice located on the 90° meridian and 0.29 inches (7.37mm) forward of the centreline of the window. This bump was found to occur up to 1.2 inches (30.48mm) forward of the datum point and was attributed to the boundary layer cross-flows on the incident side of the impingement point. Another interesting result was the behaviour of the pressure rise as the lee-side of the cylinder was approached. Instead of the forward bump preceding a much larger pressure rise that occurred approximately half an inch (12 mm) downstream of the impingement point, as the lee-side of the cylinder was approached the forward bump became the main pressure peak. Despite the fact that the lee-side of the cylinder is shielded from the incident shock wave, a pressure rise still occurs there because of the cross flows within the boundary (Morkovin et al., 1952).

Another pertinant study was carried out by Brosh et al. (Brosh et al., 1985) and detailed the impingement of an oblique shock wave (generated using a wedge of vertex angle 16°) on a cylinder. Experimental work was undertaken in a supersonic wind tunnel at a freestream Mach number of 3.0, corresponding to a freestream Reynolds number of $18 \cdot 10^6$ per meter. Experimental measurements were compared with numerical computations due to the complex nature of the flows.

Brosh et al. found that the flowfield around the cylindrical body could be divided into four different sections:

i. The windward region where the incident shock wave impinges on the cylinder. This region is governed by sever pressure gradients and shear stresses caused by the impinging shock wave.

ii. The leeward region where the flow is generally separated. This region is governed by the cross flows and thickening of the boundary layer.
iii. The upstream region ahead of the incident shock wave. This region is undisturbed, parallel to the cylindrical body's axis and at a Mach number of 3.
iv. The downstream region behind the expansion fan caused by the convex corner of the wedge. In this region the flow is straightened by the expansion fan caused by the wedge although the difference in boundary layer thicknesses between the windward and leeward sides still causes some cross flows to develop.

The surface flow pattern generated on the cylinder showed two separation lines as well as a point of reattachment. The most upstream of the two separation lines was found to terminate on the leeward side of the cylinder. The other separation line wrapped itself around the cylindrical body while changing its yaw angle from lateral to axial in the process. This separation line became the primary leeward separation line. A secondary leeward separation line was also observed. Intense cross flows of the same magnitude as the freestream axial flow were noted between the 10° and the 100° meridians.

The leeward interaction showed three distinct regions. The first of these was the most upstream region and was characterised by a thick boundary layer, the flow within almost being stagnant. The next region (downstream of the former region) was characterised by the two separation lines mentioned above. The third, and final, region was the most downstream of the three regions and was heavily affected by the expansion fan generated by the wedge and thus of less interest. The straightening of the flow by means of the expansion fan served to weaken the separation lines which eventually disappeared.

3.9.3 Conical Shock Wave/Cylindrical Boundary Layer

An investigation into the SWBLI generated by a conical shock wave impinging onto a cylindrical boundary layer was carried out by Kussoy et al. (1980). Even though the experiment was described as a "three-dimensional shock wave separating a *two-dimensional* turbulent boundary layer", the resultant interaction is described as being highly three-dimensional. The experimental setup, shown in Figure 3.15, involved a conical shock wave generator (cone half-angle of 15°) at an angle of attack of 15° located concentrically within a tube, which was fitted with various measuring stations at certain axial and azimuth positions. Tests were run at a free stream Mach number of 2.2.

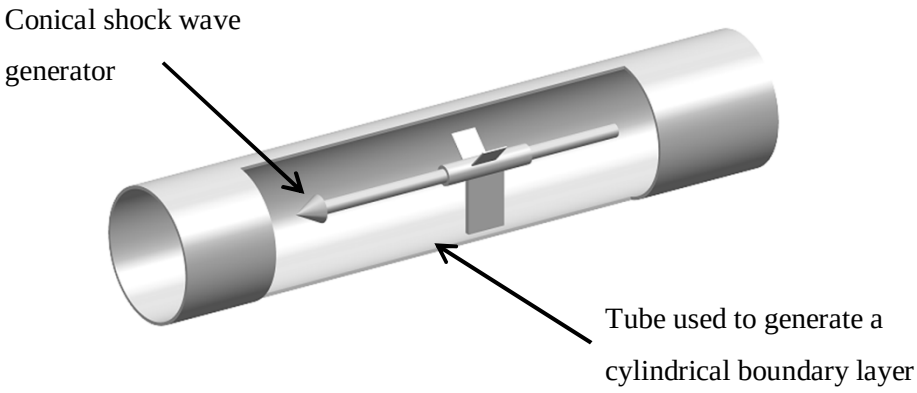


Figure 3.15: Experimental apparatus used by Kussoy et al (1980)

Based on the surface oil-flow patterns gathered from experimentation, Kussoy et al. (1980) were able to identify the shock trace footprint of the interaction. A horseshoe shaped trace was evident which eventually disappeared on the leeward side of the area under investigation. This horseshoe shape arises from the sweep of the conical shock wave. At azimuth positions of approximately +135° and -135° the trace of the shock wave turns parallel to the flow direction. A separation bubble approximately 28mm in length was measured along the windward ray (0°) of the cylinder. Significant yawing of the flow was noted in the relatively thin layer close to the surface where the low momentum (low velocity) fluid resides in a turbulent boundary layer.

The data collected from the pressure measurements shows that initial rise in surface pressure varies with azimuth and axial position; along the 0° ray the pressure rise occurred approximately 100mm from the leading edge of the cylinder, while along the 180° ray the rise only occurred at a distance of 180mm. The magnitude of the pressure rises (the ratio of maximum wall pressure to the free stream wall pressure upstream of the interaction) was also found to vary azimuthally from 1.8 to 1.5 from 0° to 180° respectively. A surface pressure plateau, often used to imply the existence of streamwise separation, was not evident along any of the meridian rays (Kussoy et al., 1980).

Kussoy et al. (1980) performed numerical simulations of the interaction by means of solving the Navier-Stokes equations for a compressible fluid. The overall behaviour of the pressure with varying position was found to be well predicted by the numerical results, as was the magnitude of the pressure rise along each of the azimuth rays. The accuracy of the streamwise location of the pressure rises was found to be insufficient for the smaller values of the azimuth angle. The calculations were found to under predict the initial pressure rise on the leeward side of the cone and over predict on the windward side. The resultant shock footprint of the measured shock (relative to the computed shock)

would reveal a more curved horseshoe shapes shock trace, i.e. the pressure rise would begin further upstream for smaller values of φ, and further downstream for larger values of φ. These quantitative differences between the measured and computed data was attributed to the simple turbulence model (turbulence effects were described using an equilibrium algebraic eddy viscosity model) used in the study.

At the time of writing no other work on fully three-dimensional SWBLI has been located in the open literature.

4 Facilities and Methodology

All experimental data was gathered using the supersonic wind tunnel facility located in the Barloworld Laboratories, North West Engineering at The University of the Witwatersrand. Numerical experimentation was performed using The Universities' Computational Mechanics Laboratory, also located in the Barloworld Laboratories.

4.1 Experimental Facilities and Methodology

4.1.1 Supersonic Wind Tunnel

The supersonic wind tunnel used for the testing consisted of the primary sections, namely the collection tank / reservoir, the test section and the exhaust. Auxiliary to this was the compressor that was used to pressurise the reservoir.

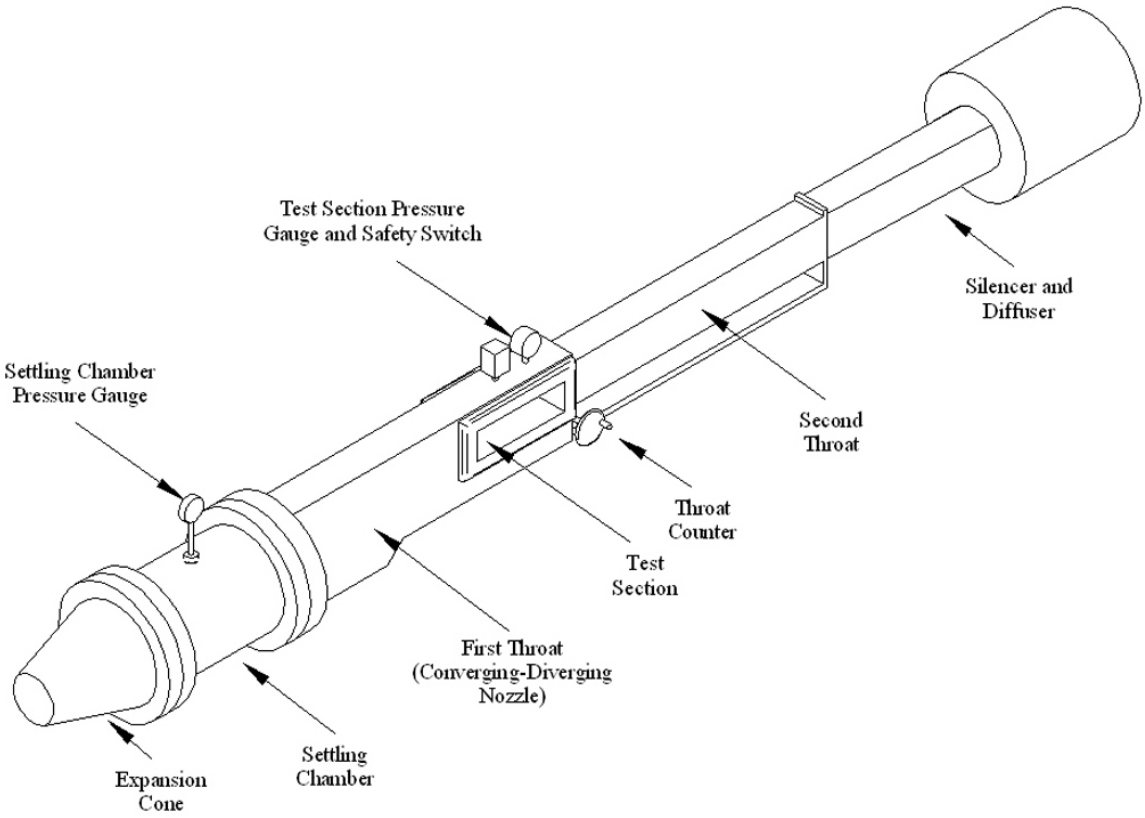


Figure 4.1: Schematic layout of the supersonic wind tunnel

The supersonic wind tunnel was extensively overhauled by the author before any consistent and meaningful results could be collected from it. The overhaul included regular maintenance on several of the internal components as well as replacement of certain parts where necessary. A full description of the overhaul can be found in Appendix A: Wind Tunnel Overhaul.

Table 4.1: Technical specification of the wind tunnel

Manufacturer:	Aero Lab
Test Section Dimensions [mm × mm]:	101.6 × 101.6
Test Section Area [mm^2]:	10322.56
Mach Number Range:	1.5 – 3.5
Maximum Supply Pressure [kPa]:	965
Maximum Test Pressure [MPa]:	3.08
Maximum Operating Temperature [°C]:	112
Maximum Blow Time [s]:	±15
Second Throat Area [mm^2]:	9460

Compressor

To provide the necessary pressure for the operation of the wind tunnel, the storage vessel is filled by means of an electronically driven reciprocating compressor. The compressor is automatically switched off when the pressure in the storage vessel reaches above 1.5MPa, the oil pressure in the compressor drops below a pre-determined value or when the cooling water supply's flow rate is too low.

Table 4.2: Technical specifications of the compressor

Manufacturer:	Reavell & Co.
Model:	CSA 4
Maximum Operating Speed [rpm]:	1000
Regular / Normal Operating Speed [rpm]:	960
Maximum Delivery Pressure [MPa]:	1.5
Maximum Design Pressure [MPa]:	3.1
Maximum Power [kW]:	18.7

Dryer

The air supplied to the storage vessel from the compressor is done so via a dryer unit which removes moisture from the air entering the tank. It is important that all moisture is removed from the air so as to prevent a condensation shock from forming during the start-up of the tunnel. The dryer consists of a series of oil and water filters, followed by the main unit which is a pressure vessel containing small pellets of silica crystal which absorb the remaining moisture from the air. By absorbing the moisture from the air, the silica crystals become saturated and must be dried themselves. This process is known as 'regenerating' the dryer. Regeneration of the dryer is achieved by blowing hot air through the dryer over the crystals for a period of 3 hours, a process controlled by a thermocouple and relays switch attached to the dryer housing.

Table 4.3: Technical Specifications for the dryer

Manufacturer:	Arlec Engineering Works CC.
Design Pressure [kPa]:	2136
Working Pressure [kPa]:	2136
Working Temperature [°C]:	100
Test Pressure [kPa]:	2777
Test Temperature [°C]:	100



Figure 4.2: Air dryer unit

Storage Vessel

Table 4.4: Technical specifications of the storage vessel

Manufacturer:	Kies & Travers Ltd
Storage Volume [m^3]:	9.04
Operating Pressure [MPa]:	1.5
Operating Temperature [°C]:	122
Operating Design Pressure [MPa]:	2.07



Figure 4.3: Supersonic wind tunnel storage vessel

Settling Chamber

The settling chamber is located downstream of the main control valve and eliminates any large scale pressure fluctuations and turbulence arising from the passage of the flow through the main control valve. The chamber consists of a flow distribution (baffle) cone and three stainless steel screens downstream of the distribution plate. A sectioned, schematic of the settling chamber is given in Figure 4.4 below.

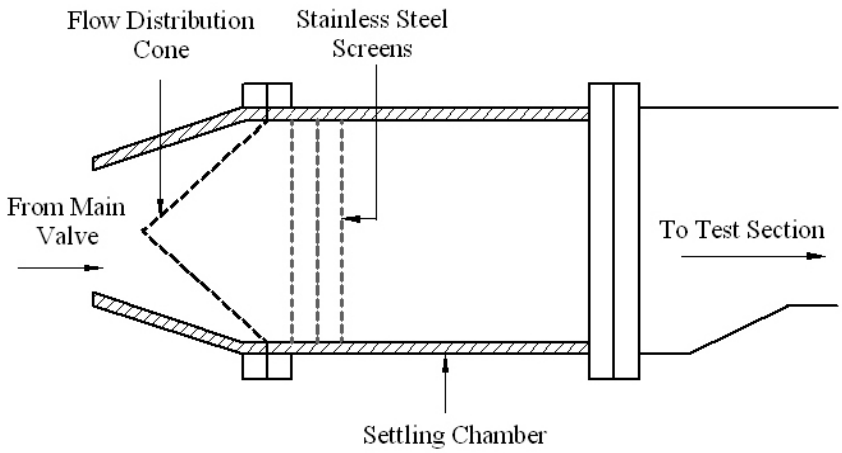


Figure 4.4: Sectional view of the settling chamber

During operation of the tunnel, the air in the settling chamber can be assumed to be at zero velocity. For this reason the stagnation pressure is measured by measuring the static pressure in the settling chamber. The required stagnation pressure within the settling chamber is set at the wind tunnel control panel located in the wind tunnel control room. The stagnation pressure must exceed a certain value (depending on Mach number) for the flow within the test section of the tunnel to go supersonic.

Figure 4.5 was generated by calculating the various pressure loading values across the pilot and main control valves for each different Mach number.

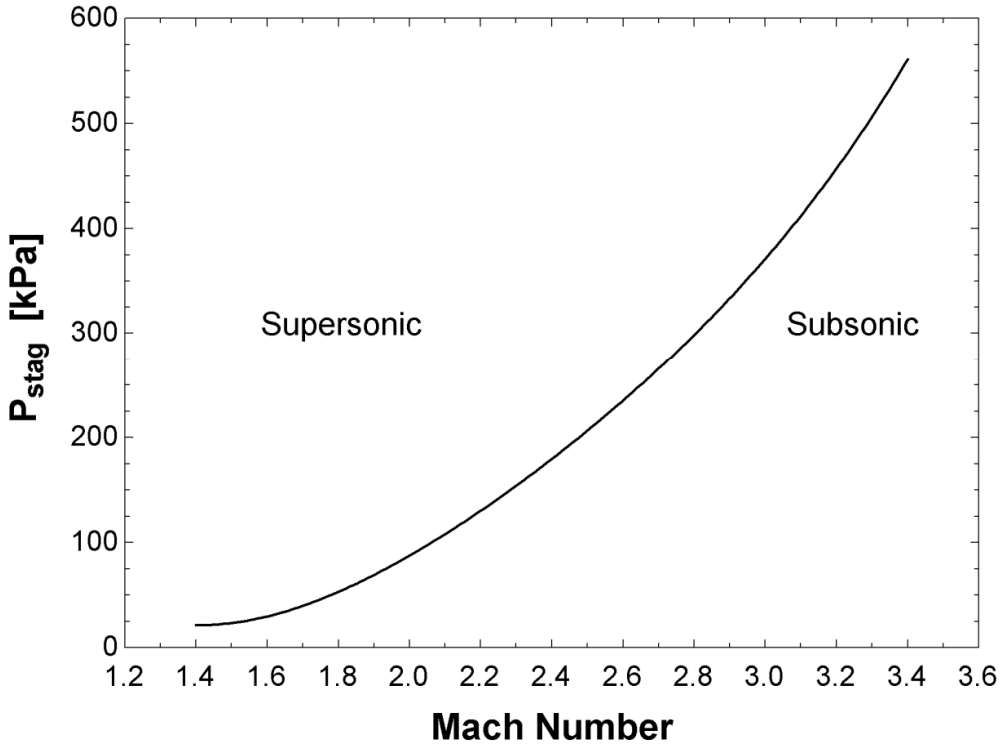


Figure 4.5: Minimum Stagnation Pressure Curve

First Throat

The first throat of the wind tunnel consists of a sliding block used give a stepless change in Mach number from 1.5 to 3.5. The area of the throat is determined by the relative position of two blocks; an upper block, fixed in position and forming the roof of the tunnel, and a sliding lower block which is the floor of the tunnel. This configuration is shown schematically in Figure 4.6.

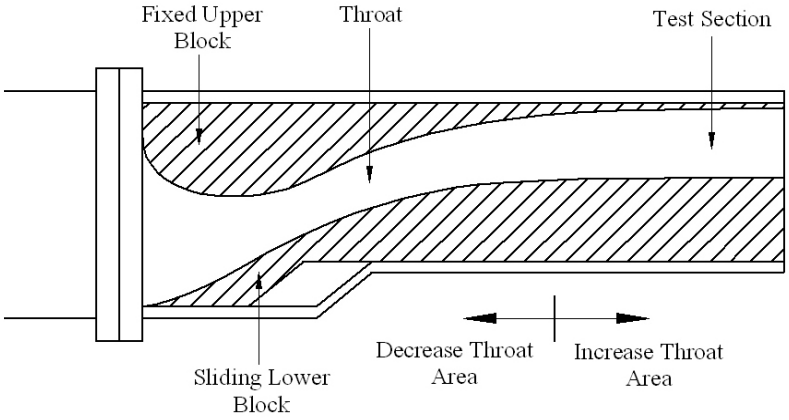


Figure 4.6: Schematic representation of the sliding block first throat

The Mach number in the test section is a function of the ratios of the area of the test section to that of the first throat. Sliding the block forward (thereby decreasing the throat area) increases the Mach number in the test section, while sliding the block backwards (increasing the throat area) decreases the test section Mach number. The position of the block is adjusted by means of a hand wheel that is attached to a veeder counter which shows the relative position of the sliding block. The value of the veeder counter is therefore used to obtain the required Mach number in the test section. A calibration of counter reading versus Mach number is thus necessary, and is given in Figure 4.7 below. A detailed explanation of the calibration is given in section A.3 of Appendix A.

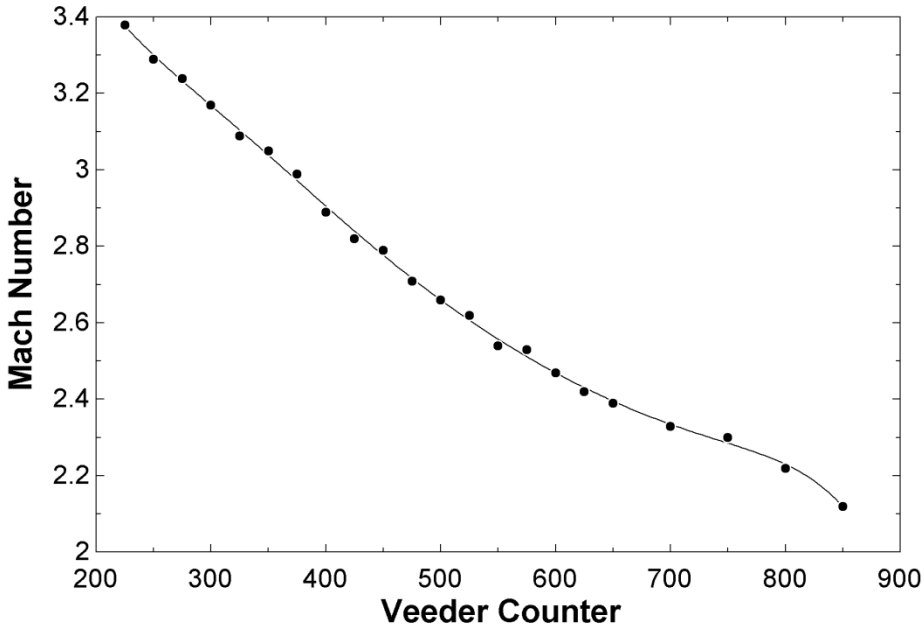


Figure 4.7: Mach number calibration curve

Test Section

The test section of the tunnel has a working area 4" x 4" (101.6mm x 101.6mm), allowing for a maximum model cross-sectional area of approximately 700mm^2. Two schlieren quality rectangular windows (in removable frames) form the side walls of the test section. Five static pressure ports are located on the upper wall of the test section, the middle of which presently houses the safety switch. The pressure transducer measuring the pressure in the test section is located in another of the ports as is a gauge for an instantaneous readout of the pressure in the test section.

Second Throat

Downstream of the test section is the second throat of the wind tunnel. The second throat is designed to bring the flow back to subsonic conditions from the supersonic velocities within the test section. This is achieved simply by means of a hump located on the floor of the tunnel, contracting the area of the tunnel by 8.5%. Due to the fixed nature of the contraction, the second throat must be designed for the lowest operational Mach number of the tunnel. Under these conditions (i.e. at Mach 1.5) the flow becomes subsonic across a weak shock wave located immediately downstream of the second throat. As the Mach number increases, the flow only slows down through the second throat before accelerating again, and returns to subsonic flow (across a stronger shock) at a location further downstream.

Pressure Control System

In order for the flow in the tunnel to become supersonic, a certain minimum stagnation pressure is required. Furthermore it is required that this pressure be kept as close to constant as possible for the duration of the test so as to prevent fluctuations in the Reynolds number of the mean flow. The stagnation pressure is kept constant using a self-regulating, pneumatic system the layout of which is shown Figure 4.8. During the initial phase of a test the stagnation pressure varies as a damped sinusoid and takes up to 10s to settle.

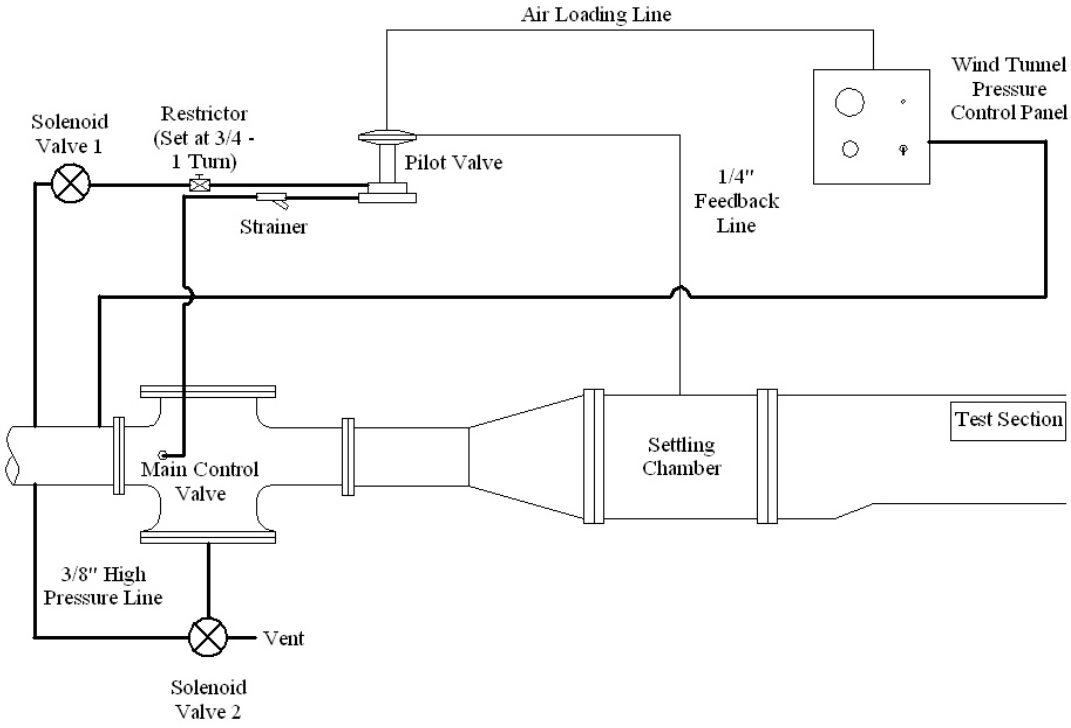


Figure 4.8: Pneumatic layout for the pressure control system

The control system uses air tapped off the main control valve located immediately downstream of the reservoir, and is fed to both the control panel (housing a direct reading pressure gauge and a regulator) and the pilot valve. The regulator located within the control panel sets the pressure in the air loading line to the diaphragm of the pilot valve, while the direct reading pressure gauge indicates the pressure being supplied to the pilot valve. With pressure above the diaphragm, the pilot valve opens and high pressure air flows through the high pressure line to the first solenoid valve. This action effectively primes the wind tunnel for a blow down. Pressing the 'Tunnel Run' button on the control panel opens the first solenoid valve allowing the high pressure air to load the diaphragm of the main control valve. The main control valve is then opened and air flows into the settling chamber of the tunnel. As the pressure in the settling chamber increases the feedback line from the settling chamber to the pilot valve loads the underside of the diaphragm of the pilot valve, and the pilot valve partially closes. This partial closure of the pilot valve lowers the pressure of the air supplying the main control valve, and that in turn partially closes and the flow into the settling chamber is subsequently reduced. This process continues (in the damped sinusoid mentioned above) until the desired pressure is achieved and maintained.

A critically important aspect of the pressure control system is the safety shut-off system. This system consists of a single pressure switch (introduced previously and detailed in Table 4.5) that supplies power to solenoid valve (SV) 1, located at the pilot valve, and SV2, located at the main control valve.

Should the static pressure in the test section rise above a set level, the safety switch will cut-off the power supply to SV1 causing it to shut, while simultaneously energising SV2 allowing it to open. The result is that the high pressure air supplied to the main control valve is terminated at SV1 and any air remaining in the pressure line from the pilot valve to the main control valve is vented to atmosphere through SV2, shutting-down the wind tunnel rapidly. It is recommended that the safety shut-off system be tested approximately every three months to ensure it is operating correctly (Scott, 1994). Tests are performed by applying a known load to the switch and seeing at what pressure the solenoid valves are activated.

Table 4.5: Specifications of the pressure control system

Main Control Valve	
Manufacturer and Type:	Spence Engineering 6" Type E Pressure Reducing Regulator
Operating Pressure Range [kPa]:	0-450
Pilot Valve	
Manufacturer and Type	Spence Engineering Type A85 Air Adjusted Pilot Valve
Operating Pressure Range [kPa]:	0-450
Solenoid Valve – Main Control Valve*	
Manufacturer and Type	ASCO SC B321A002
Differential Pressure [kPa]:	70-1400
Solenoid Valve – Pilot Valve*	
Manufacturer and Type	ASCO SC B320A182
Differential Pressure [kPa]:	0-1700
Safety Switch	
Manufacturer and Type	ASCO Tri-point PB10A
Operating Pressure Range [kPa]:	0-420

* A full specification listing of the solenoid valves is available in Table A 4 and Table A 5 in Appendix A: Wind Tunnel Overhaul.

Data Acquisition System

The Data Acquisition System (DAQ) used consisted of the following components:

- Front end pressure transducers
- Single unit power supply
- Amplifier
- Oscilloscope
- Computer based DAQ software package

Table 4.6: Oscilloscope Specifications

Manufacturer:	Yokogawa
Model:	DL1200A Digital Oscilloscope
Number of channels:	4
Operating Frequency [MHz]:	100

Pressure Transducers

The tunnel is currently fitted with two electrical pressure transducers. One is fitted to the settling chamber (representing the stagnation pressure) and the other to the test section (representing the static pressure) of the tunnel. Both of the transducers are Kyowa PG-type strain gauge pressure transducers which output a 2mV/V signal from a 10V power supply. This results in the maximum output of the transducers being a very small 20mV. Therefore an amplifier is used to boost the signal and reduce the noise in the signal.

Table 4.7: Pressure transducer details

	Settling Chamber Transducer	Test Section Transducer
Type	Kyowa PG-10KU	Kyowa PG-2KU
Maximum Pressure [kPa]	981	196
Maximum Overload Capabilities	150%	150%
Supply Voltage [V]	10	10
Full Scale Output [mV/V]	2.0	2.0

In view of the fact that the transducers output is given in Volts, a calibration converting the output voltage to pressure (Pascals) is required. The calibration curves for each of the transducers are given in Figure 4.9 below:

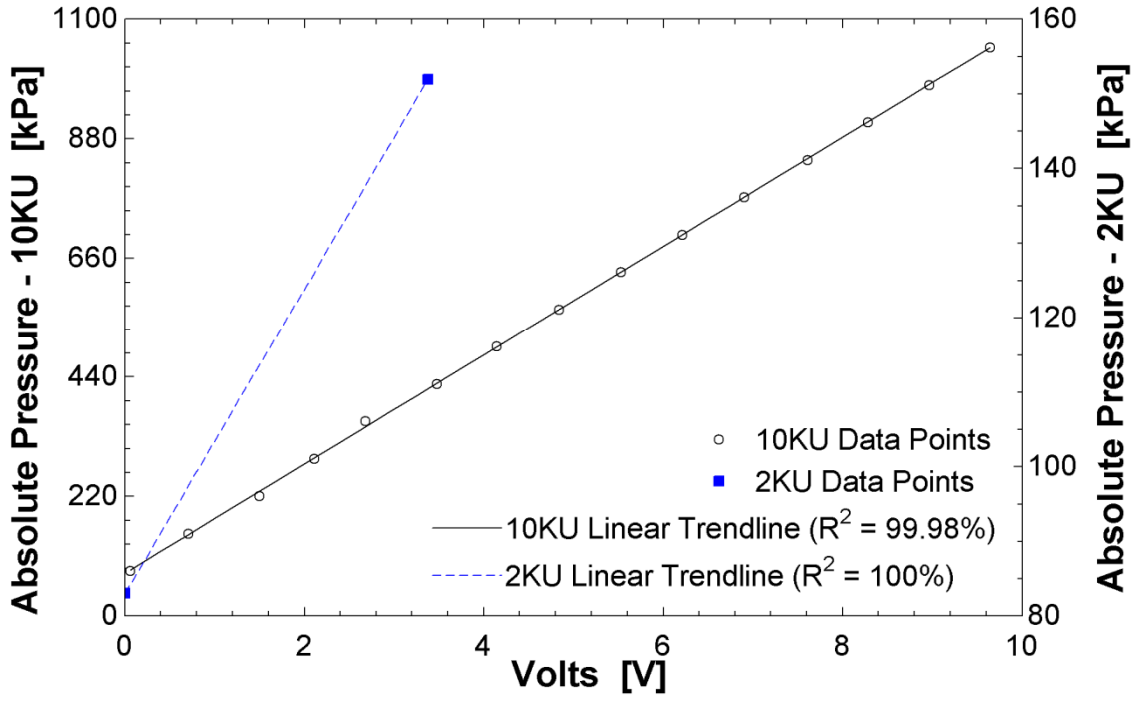


Figure 4.9: Pressure transducer calibration curve

Due to the limited range of the calibration weights available, the test section pressure transducer (2KU) could only be calibrated using two data points. In spite of this the calibration curve matched previous calibration data and gave satisfactory results when used to process raw data from the wind tunnel.

4.1.2 Flow Visualisation – Schlieren Photography

Schlieren is the succinct name given to imaging the gradient disturbances of inhomogeneous transparent media. Schlieren is an optical image which, via the level of illuminance, highlights the changes in the first derivative in the refractive index in the medium under investigation. The schlieren system is often favoured to the shadowgraph system as it is generally more sensitive to disturbances (Settles, 2001).

For the purposes of this study, a Z-Type two-mirror schlieren system was utilised. The Z was configured in the vertical plane (due to space restraints in the wind tunnel control room) using a vertical gantry. The configuration of the system can be changed to the shadowgraph technique by the simple removal of a single component.

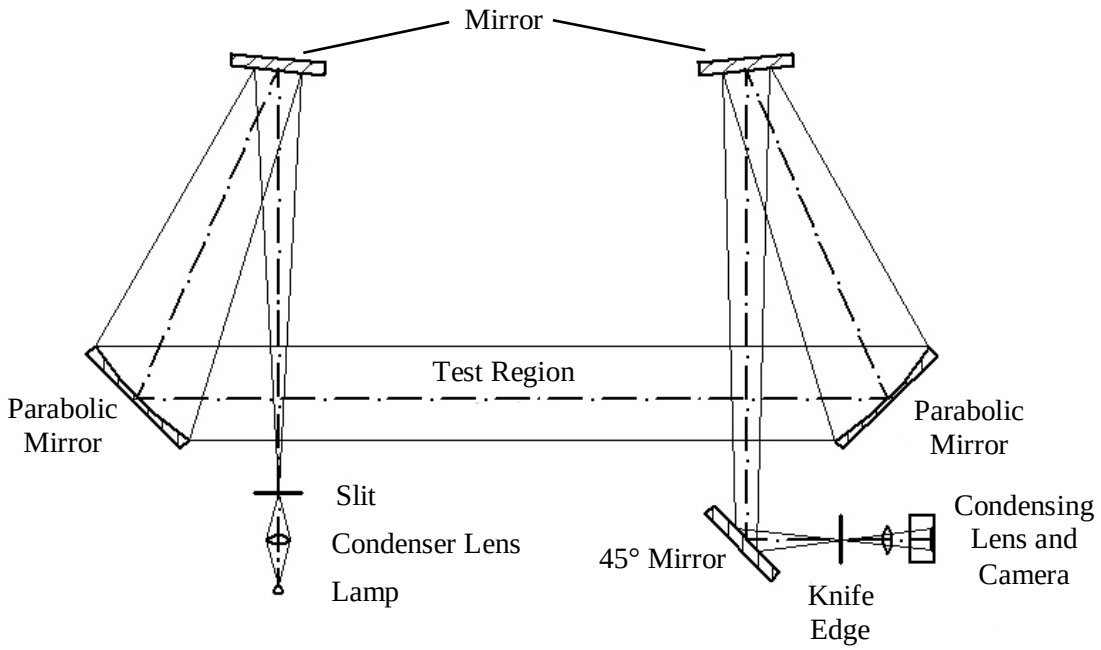


Figure 4.10: Schlieren photography layout

Light Source

The light source used was a continuous light source consisting of a General Electric 650W Halogen light bulb (as used in overhead projectors). The selection of a continuous light source over a flash lamp light source is explained in Appendix A: Wind Tunnel Overhaul. The lamp requires a 24V AC power supply, and due to its high power rating (650W) a cooling fan to prevent the bulb from overheating and possibly shattering. The light source was also fitted with a dimmer switch to adjust the intensity of the bulb.

The second component of the light source, the condenser lens, is a 30mm diameter lens with focal length of 40mm mounted onto the block housing the lamp to ensure that both the lamp and lens are axially aligned. The condenser lens is used to focus the light ray onto the source knife edge.

Mirrors

The Z-Type two-mirror schlieren system, as its name suggests, uses two mirrors as the schlieren heads. In this instance the mirrors used were two F8, 6” (152.4mm) diameter parabolic mirrors. The mirrors are surface coated and thus can be cleaned when necessary.

4.1.3 Flow Visualisation - Oil Surface Flow Visualisation

Oil surface flow visualisation was utilised as it would provide the most suitable illustration of the flow on the surface of the cylinder in the region of the SWBLI. Two mixtures were used for the flow visualisation, the first being a transformer oil based mixture. This mixture consisted of the following ingredients:

- 8 tsp Titanium dioxide
- 5 tsp Transformer oil
- 1-2 drops Oleic acid

The mixture that performed consistently the best was achieved by first mixing four teaspoons of the titanium dioxide with all five teaspoons of the transformer oil until a smooth paste forms. Another two teaspoons of the titanium dioxide were then added and mixed in thoroughly, followed by a small drop of the oleic acid. One more teaspoon of the titanium dioxide was then added and mixed followed by the second drop of the oleic acid. The oleic acid thins the mixture out very easily and so should be added very carefully as too much will ruin the mixture. The eight and final teaspoon of titanium dioxide was then added and mixed in thoroughly. The mixture should be of such a consistency and viscosity that it runs off the back of a spoon, but should still be able to adhere to the model when applied lightly.

The second mixture utilised was a paraffin based mixture consisting of the following ingredients:

- Paraffin
- Titanium Dioxide
- Transformer oil

The precise ratios of the above depend on the exact application and require some minor adjustments. In general a consistency similar to that of genuine maple syrup should be strived for.

For best results both mixtures were applied uniformly to the models using a sponge as shown in Figure 4.11.



Figure 4.11: Oil surface flow mixture when applied to the models

4.1.4 Test Specimens

In order to create the necessary shock waves and boundary layers, an apparatus from a previous study into SWBLI was modified for use. The apparatus is designed in such a manner so as to simultaneously generate a curved boundary layer and a curved shock wave to impinge on each of the two cylinders. An intrinsic aspect of the mounting system is its ability to rotate through 360° allowing the interactions to be viewed from all possible angles. The complete apparatus assembly is shown in Figure 4.12.

The test apparatus is slid into the test section and the rectangular support frame is fixed (externally) to the upper chord member of the test section by means of two cap screws. Two rubber gaskets are used to seal the join between the tunnel and the model support frame.

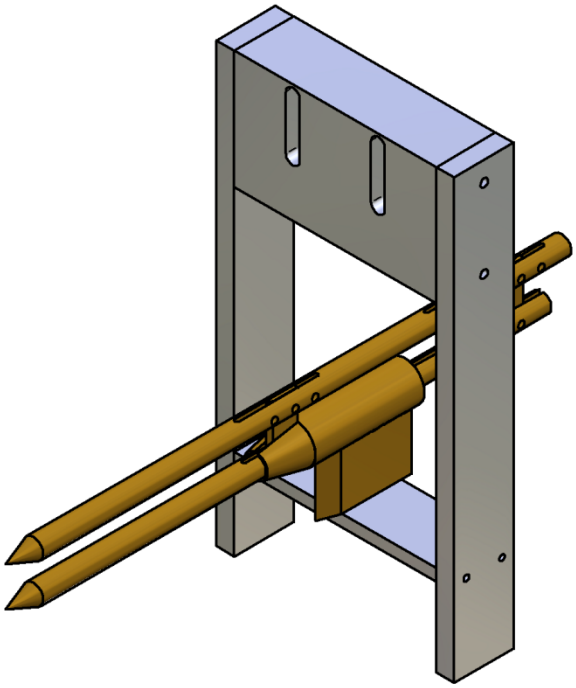
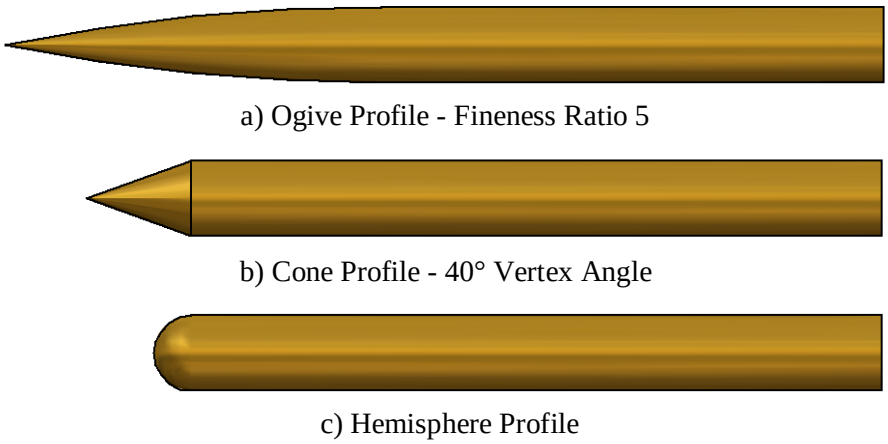


Figure 4.12: SWBLI generators and mounting bracket

One of the key aspects of this investigation is to characterise the nature of the SWBLI with varying (incident) shock strength. For this reason three different nose profiles (shown in Figure 4.13) were selected for testing:

- An ogive with a fineness ratio of 5.
- A cone with a vertex angle of 40°.
- A hemisphere with a radius equal to that of the cylinder.

The ogive profile has a large fineness ratio (5) compared to the other profiles (cone = 1.4, hemisphere = 1) and therefore is expected to produce the weakest shock wave of all. Conversely, the hemisphere will produce a strong, detached shock wave that should result in the strongest SWBLI of the three profiles.



a) Ogive Profile - Fineness Ratio 5

b) Cone Profile - 40° Vertex Angle

c) Hemisphere Profile

Figure 4.13: Shock wave generator profiles

4.2 Numerical Facilities and Methodology

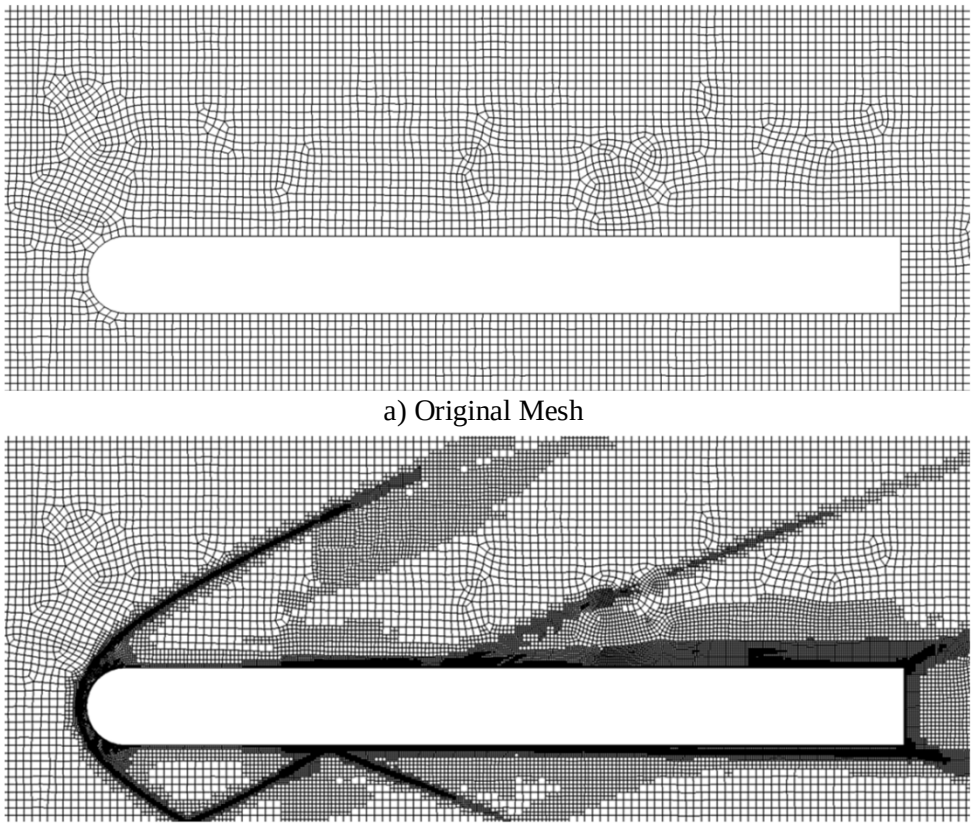
In addition to the data collected using the supersonic wind tunnel, a numerical analysis was performed by solving the Navier-Stokes equations using the commercially available Computational Fluid Dynamics (CFD) package Fluent v12.0.16. A quad core Intel Xeon 3.0 GHz processor and 8 GB of RAM running Windows 7 (64-bit) was utilised for the numerical work. Pre-processing work was carried out using Ansys Workbench v12.0.1, while post-processing work was undertaken using Tecplot 360 2009.

A high resolution simulation was run for the hemispherical SWBLI generator using the commercially available CFD package Star-CCM+ v4.06.11. This simulation was carried out using a more powerful computer than that used for the regular CFD consisting of two quad core Intel Xeon 2.66 GHz processors with 16GB of RAM running Windows 7 (64-bit). Pre-processing work for the high resolution case was carried out using Star-CCM+, while Tecplot 360 2010 was used to post-process the data.

4.2.1 Mesh

The flow fields created for the purposes of the general (Fluent) simulations were all meshed using quadrilateral cells. In the interests of computational efficiency a mesh adaption scheme was utilised so as to refine the pertinent features that existed in the flow field. Adaption was carried out using multiple criteria, the most common of which included density and pressure gradients and Mach number. An example of the grid pre- and post-adaption is given in Figure 4.14. In an effort to resolve the boundary layer sufficiently, the cells in the immediate vicinity of the walls of the SWBLI

generators were four times as fine as their far-field counterparts. All walls were modelled using the no-slip wall condition. Mesh independence was achieved due to the constant adaption of the mesh throughout the simulation, a result that is confirmed by the behaviour of the residuals over the course of the iterations. Immediately following each of adaption there was a sharp increase in the residuals before a mean value that did not vary with each subsequent adaption, was settled on.



a) Original Mesh

b) Adapted Mesh

Figure 4.14: Mesh adaption scheme illustration

The high resolution CFD model run in Star-CCM+ was meshed using polyhedral cells. The boundary layer was resolved using Star-CCM+'s prism layer meshing tool and consisted of several layers that thickened exponentially. The area of the SWBLI, as well as the region upstream of the SWBLI, was refined to investigate upstream affects of a SWBLI as shown in Figure 4.15. Mesh independence for the Star-CCM+ simulation was ensured by comparing the results and residuals of final high resolution model with the various lower resolution development models.

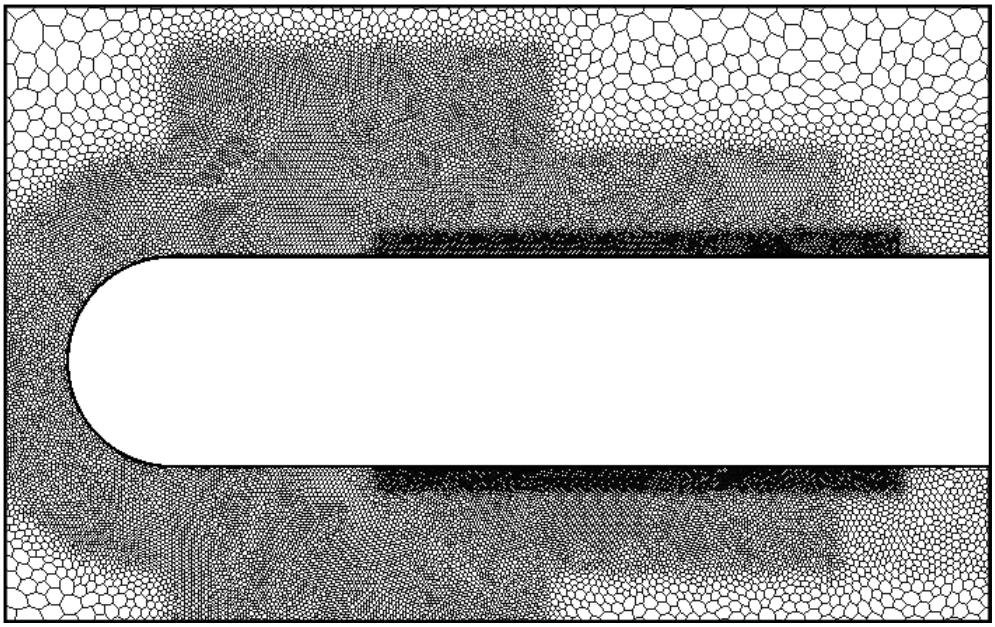


Figure 4.15: Star-CCM+ structured mesh

All of the simulations performed utilised a pair of symmetry planes so as to reduce the overall cell count, and hence computation time, of each of the simulations. The first symmetry plane was taken vertically through the axes of the SWBLI generators, while the second plane was taken horizontally at the mid-point between the two cylinders. The latter (horizontal) symmetry plane served as the reflection plane for the shock waves generated by the nose profiles of the SWBLI generators. The suitability of a symmetry plane being used as a reflecting surface was highlighted in section 3.4. Figure 4.16 shows the twin cylinder setup (viewed from the front) and the aforementioned symmetry planes.

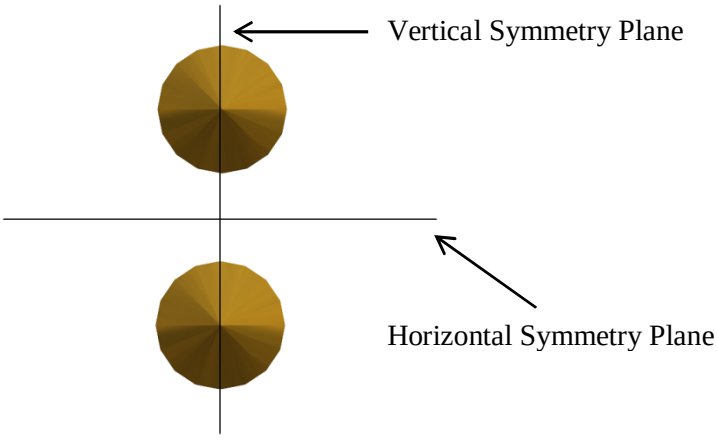


Figure 4.16: CFD symmetry plane illustration

4.2.2 Turbulence Model

Due to the turbulent nature of the boundary layer under investigation, a suitable turbulence model had to be selected for the CFD simulations. For all of the simulations undertaken, the K-Omega turbulence model was utilised. The K-Omega model is a two-equation solver, where the transport equations are solved for the kinetic energy and the specific dissipation rate, the latter being defined as the dissipation rate per unit turbulent kinetic energy. The K-Omega model was selected over other available models such as Spallart-Almaras and the K-Epsilon models for various reasons namely; Spallart-Almaras models generally are best suited for flows in which the flows remain largely attached. As highlighted in section 3.8.1, separation is a common occurrence in SWBLI and hence separation effects cannot be ignored. The K-Epsilon model is generally well-suited for most industrial applications; however the K-Omega offers improved performance (over K-Epsilon) for boundary layers under adverse pressure gradients. The greatest advantage however is that it (the K-Omega model) may be applied throughout the entire boundary layer, including the viscous-dominated region without any modification (Wilcox, 2004).

4.2.3 Solver Type

For the purposes of this study, all CFD simulations were run under steady state conditions. It is widely understood that SWBLI are in fact unsteady in nature, as shown in studies by Dussauge and Piponniau (2008), Dupont et al. (2005), Kussoy et al. (1988) among many others. A complete study of this unsteadiness is deemed to be outside of the scope of this work and thus will not be studied directly. It (the shock waves' unsteadiness) may be considered when comparing the numerical results to their experimental counterparts, as the latter will exhibit a degree of unsteadiness.

5 Procedure

5.1 Pressurising the Storage Vessel

In order to run the tunnel at the required supersonic speeds, the pressure in the reservoir has to be greater than 0.9 MPa, with the required pressure for three supersonic runs being 1.5 MPa. To operate the compressor used to pressurise the tunnel:

1. Close both of the bleed valves on the dryer; ensure that the dryer is switched off and that the impeller has stopped rotating.
2. Switch on the pressure vent solenoids.
3. Activate the water supply to the compressor by turning the valve one full revolution counter-clockwise. Once the flow of water is heard, close the valve one-quarter revolution clockwise.
4. Switch on the compressor at the electrical control board.

Once the reservoir had reached a pressure of 1.5 MPa, the compressor will automatically shut itself down to prevent the reservoir for being pressurised beyond its maximum pressure of 1.7 MPa. To complete the shutdown of the compressor and prepare the tunnel:

1. Switch off the compressor at the electrical control board. This will ensure that compressor does not restart when the pressure in the storage vessel drops during a test.
2. Turn off the water supply.
3. Switch off the pressure vent solenoids.
4. Starting with the top bleed valve, bleed the air in the dryer tank attached to the pressurised reservoir. This is done by **slowly** opening the top valve until all of the air has vented to atmosphere, and the accompanying pressure gauge reads zero. Thereafter open the lower valve fully.

5.2 Pre-test Procedure

1. Switch on the DAQ components approximately two hours before the commencement of testing. This will allow the system to warm up and for the fluctuations in the system, caused by the start-up, to stabilise.
2. Pressurise the storage vessel to 1.5MPa as explained previously.

5.3 Wind Tunnel Blow Down

Once the storage vessel has been pressurised sufficiently and the compressor has been completely shut down can the tunnel be safely run. The checklist for the operation of the supersonic wind tunnel is outlined below:

1. Set the Mach number by selecting the desired value on the throat veeder counter.
2. Ensure that the various locking nuts and screws on the models are securely tightened. Also ensure that the model is safely secured onto the mounting frame. The complete model assembly (cones, collar and mounting frame) must then be inserted into the test section of the tunnel. This should be done with care so as to ensure that no part of the assembly touches, possibly scratching, the windows and / or floor of the tunnel. The frame must be securely fastened to the upper chord member of the tunnel.
3. Slide the tunnel shut, and tighten the wing nuts located on the sides of the tunnel, aft the test section, so that the tunnel is completely sealed and that the sliding section is unable to open during the operation of the tunnel.
4. Switch on the wind tunnel control board, and open the valve until the stagnation pressure reaches the desired level.
5. Switch on the power supply to the warning siren.
6. Log all of the relevant information regarding the test (including tunnel parameters, models being tested, trigger voltages and delays etc.) into the wind tunnel logbook.
7. Sound the warning siren for **at least** 3 seconds.
8. Switch on the light source for the flow visualisation. Turn off the lights in the tunnel control room. ***Note:*** If any changes to the models have been made, the first test immediately thereafter must be performed with the control room lights on to ensure that all pieces within the test section are securely fastened and do not excessively move around during the blow down. For a 'lights on' test no image is captured and hence operation of the flow visualisation system is not required.
9. Run the tunnel by pressing (and holding) the appropriate button on the control board. The duration of the run should exceed 5 seconds so as to allow the fluctuations in the pressure control system to stabilise.
10. Take a photograph of the flowfield.
11. Stop the tunnel by releasing the tunnel run button.
12. Sign the logbook and note any important outcomes from the test.
13. Repeat steps 6-12 for each successive test conducted.

5.4 Wind Tunnel Shut Down

Once the three tests have been completed, the reservoir needs to be re-pressurised. This is done by:

1. Switching off the main power supply at the wind tunnel control box and at the warning siren. The stagnation pressure must also be returned to 0.
2. Ensure that the light source is switched off and unplugged.
3. Pressurise the reservoir as outlined in section 5.1.

At the end of every three or four reservoirs pressurisations the dryer must be regenerated, as explained in section 4.1.1. The dryer regenerator (heater) is operated as follows:

1. Switch on the power supply to the heater at the electrical control board. The switch is located to the left of the pressure vent solenoids switch.
2. Switch on the heater on the front panel of the dryer control unit (located underneath the dryer itself). The heater is programmed to run for an allotted period of time and will stop automatically. Once the heater has finished simply switch off the unit and the power supply to the unit.

5.5 Precautions

Several precautions must be adhered to at all times during the execution of the blow down of the tunnel:

- Care should be taken when bleeding the dryer tank as the air being bled is highly pressurised.
- Ear protection must be worn at all times during the blow down of the tunnel.
- The operator must stand clear of the test section during a blow down.
- The position of the optics system must not be altered until a complete series of tests have been completed.
- The light source must not be left on for extended periods of time. This will prevent the bulb from possibly exploding and the mounting box from overheating.

6 Presentation and Analysis of Results

6.1 Pressure, Mach and Reynolds Number Traces

Pressure readings were collected for each blow-down of the wind tunnel using the pressure transducers described in section 4.1.1. These readings were then processed into curves showing the settling chamber pressure, test section pressure, Mach and Reynolds number variation throughout a given test.

The formulae used to calculate the Mach and Reynolds numbers are (Scott, 1994):

$$M = \left(\frac{2}{\gamma - 1} \left[\left(\frac{P_T}{P} \right)^{\frac{\gamma - 1}{\gamma}} - 1 \right] \right)^{\frac{1}{2}} \qquad [6.1]$$

$$\mathrm{Re} = \frac{P^{\frac{5-\gamma}{4\gamma}} P_T^{\frac{5(\gamma-1)}{4\gamma}} dT_1^{\frac{3}{4}}}{\mu_0 T_A^{\frac{5}{4}}} \times \left[\left(\frac{2\gamma}{R(\gamma - 1)} \right) \times \left(\left(\frac{P_T}{P} \right)^{\frac{\gamma - 1}{\gamma}} - 1 \right) \right]^{\frac{1}{2}} \qquad [6.2]$$

A full derivation for both parameters (M and Re) is given in Appendix B: Derivations.

The pressure values shown in the curves represent absolute pressures since atmospheric pressure was accounted for in the calibration of the pressure transducers. The settling chamber pressure corresponds to the stagnation pressure, while the test section pressure corresponds to the static pressure of the system. The curves illustrate the variation of M and Re throughout the course of a test – the significance of which will be discussed further on.

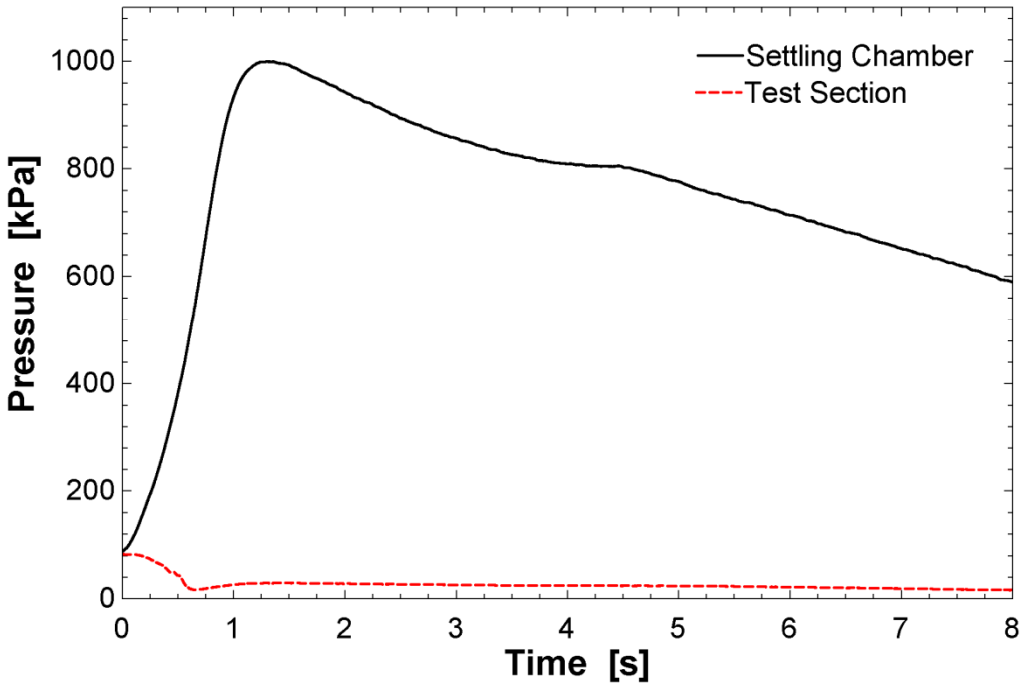


Figure 6.1: Settling chamber and test section pressure curves during a blow-down (M = 3.0)

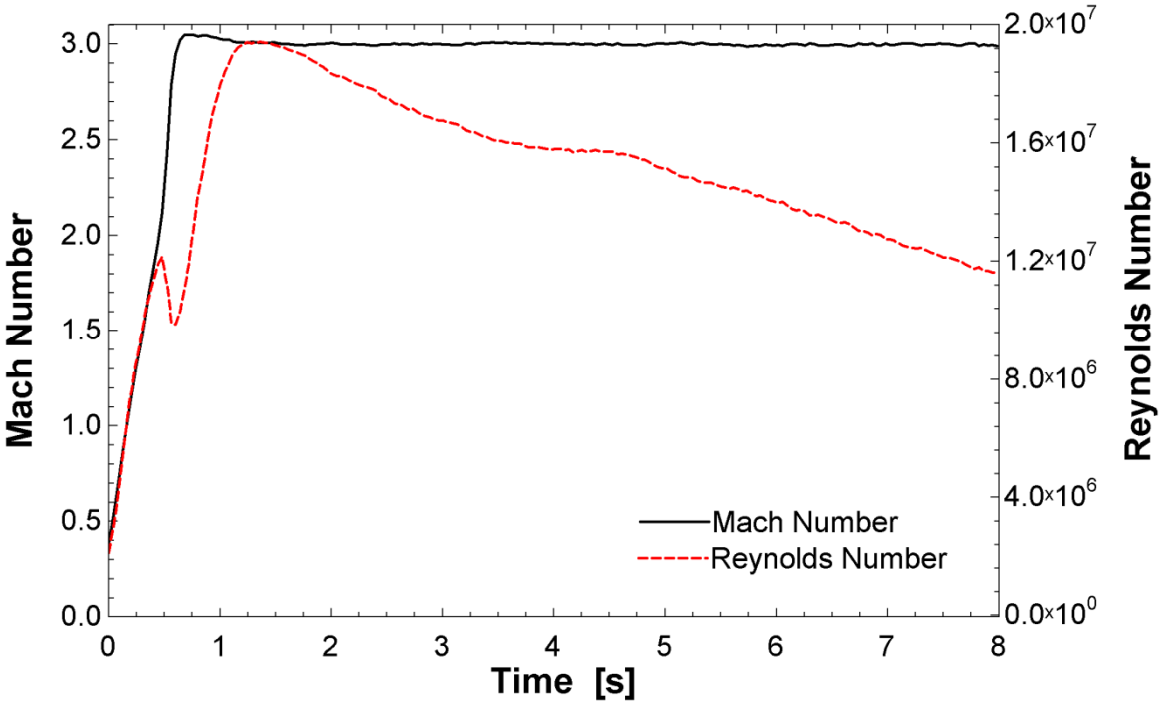


Figure 6.2: Mach and Reynolds number curves during a blow down (M = 3.0)

The Mach and Reynolds number curves generated in above serve to verify the results and offer an improved understanding of the operations of the supersonic wind tunnel. The Mach number curve was used to validate the Mach number set on the veeder counter of the wind tunnel. The curve also illustrates the change in Mach number over the course of a blow-down. If a large scale variation in Mach number was detected during a test, then the validity of the results of that test could be brought into question. The Reynolds number curve generated has a two-fold purpose; i) to offer an insight into the operation of the wind tunnel and, ii) to verify that the recent overhaul of the wind tunnel has not affected its fundamental operation. The pressure traces presented are intermediary steps in the calculation of the M and Re number. Both of the aforementioned parameters are functions of the stagnation and static pressures as shown in the conversion equations in section 6.1.

The overall behaviour of the pressure, Mach and Reynolds number was found to be relatively predictable given the form of the conversion equations in section 6.1. Some of the key features of the curves include:

- Following the rapid rise at the start of a blow-down, the settling chamber pressure decreases continuously throughout the test. The pressure within the test section responds by also decreasing continuously throughout the test, albeit at a markedly lower rate.
- Minor, small-scale oscillations are present in both the stagnation and static pressure curves. The minor oscillations are magnified in the M and Re curves.
- The Mach number remains almost perfectly constant throughout the course of a blow-down. The calculated Mach number also corresponds to the set/calibrated Mach number very well.
- The Reynolds number decreases continuously in a manner precisely the same as that of the settling chamber (stagnation) pressure.

These are all features that were noted by Scott (1994) in a previous study using the wind tunnel indicating that the fundamental operation of the wind tunnel has not been compromised since the completion of the recent overhaul. Scott (1994) also gives a detailed description of the minor oscillations in the pressure, Mach and Reynolds number curves which may be of interest to the reader.

6.2 Experimental and Numerical Results

6.2.1 Overview

The following section contains the results of the wind tunnel experiments as well as the numerical experiments (CFD simulations) performed. The wind tunnel and CFD results are presented simultaneously (where applicable) to highlight the similarities between the sets of data. The wind tunnel data is presented in the form of schlieren photographs and oil surface flow visualisation, while the CFD data is presented as contour plots, streamlines and plots of the various parameters pertaining to the flow.

All of the wind tunnel tests and CFD simulations performed were done at a free stream Mach number of 3.0. The three nose profiles introduced in section 4.1.4 were tested in all cases at a fixed distance of 30mm between axes. Throughout this section results are presented for various meridian angles around the cylindrical SWBLI generators. The labelling convention for these meridians is shown in Figure 6.3 below. The cone/cylinder shown here corresponds to the **bottom** cylinder shown in the full test apparatus illustrated in Figure 4.12.

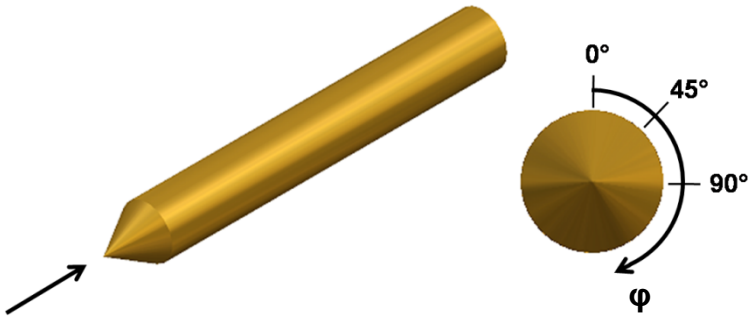
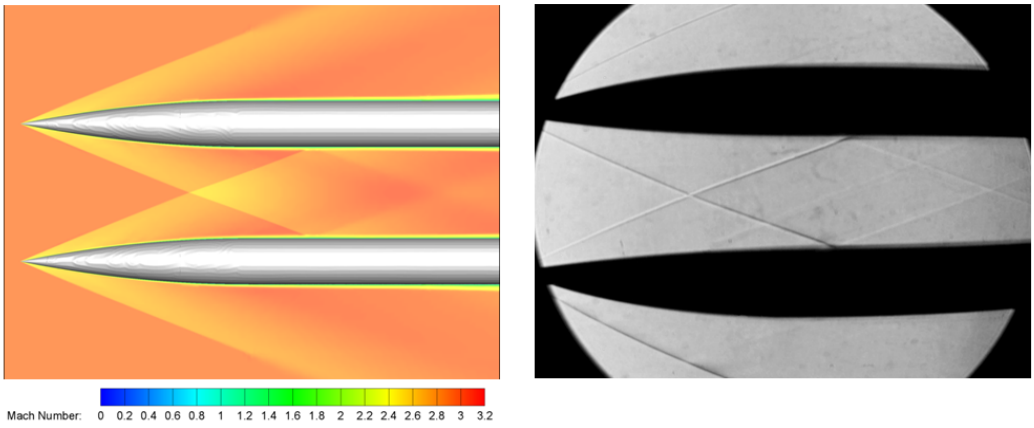


Figure 6.3: Meridian angle convention

The right hand side of Figure 6.3 represents the front view of the SWBLI generator as viewed in the direction of the arrow on the left hand side of Figure 6.3. The 0° position shown in Figure 6.3 is the windward plane as the SWBLI develops initially along this meridian (the term ‘meridian’ and ‘plane’ will be used interchangeably). Consequently the 180° meridian is defined as the lee side (leeward meridian) of the SWBLI generator as it is partially sheltered from the shock wave. Positive rotation is defined as clockwise rotation as shown in Figure 6.3.

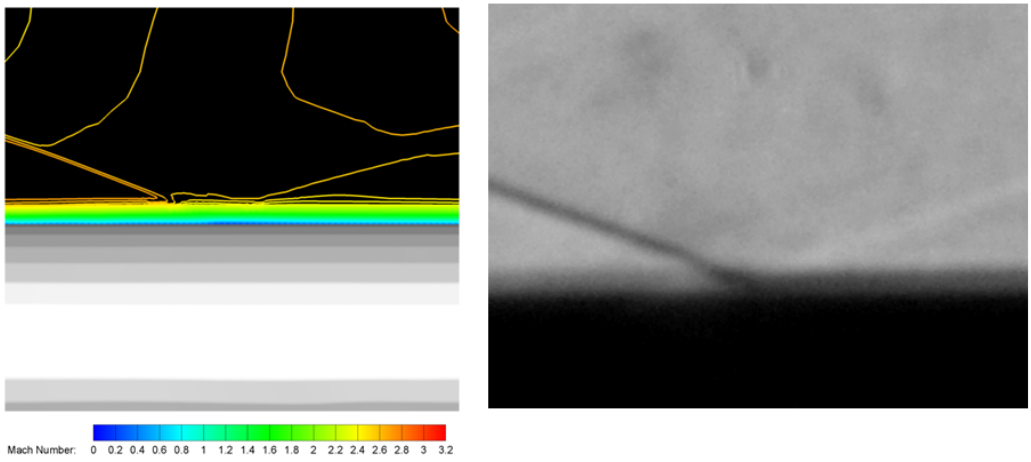
6.2.2 Flow Visualisation

Figure 6.4 through Figure 6.16 are the schlieren images collected from the supersonic wind tunnel and corresponding contour plots generated by the CFD simulations. A full discussion of the images in question is presented towards the end of this section (section 6.2.2).



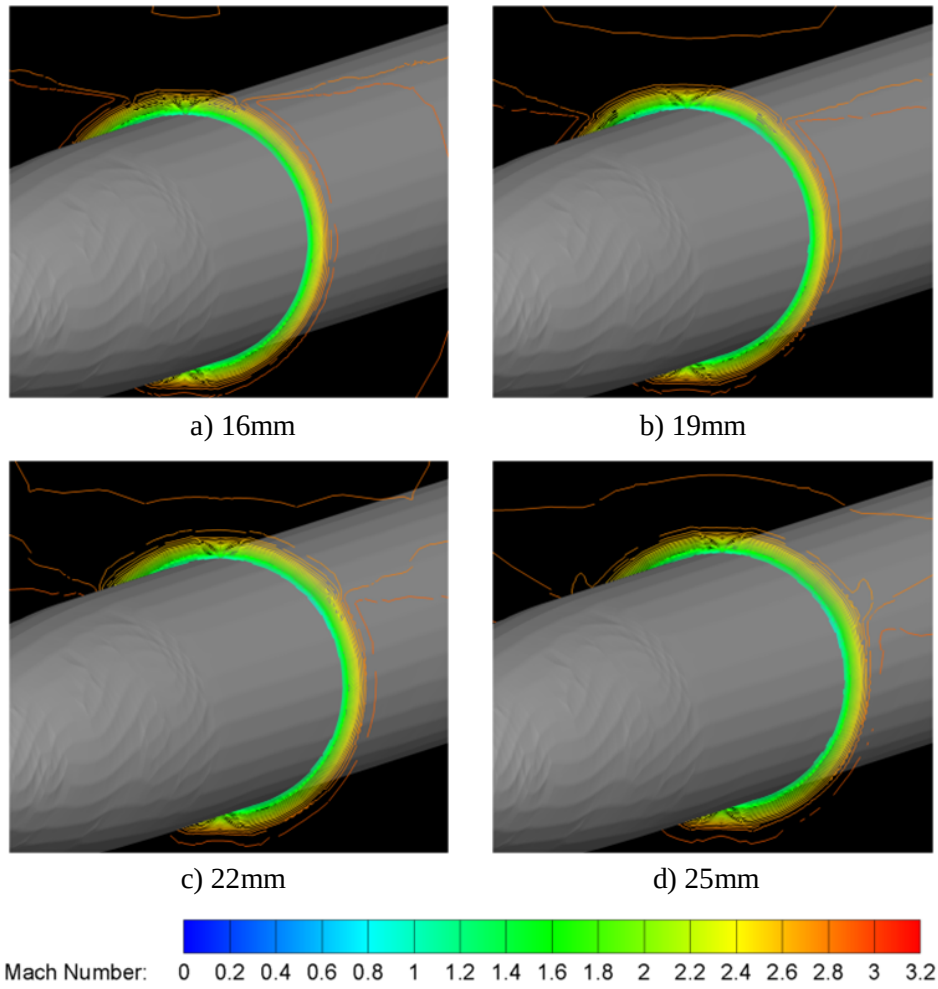
a) CFD Mach contour plot b) Schlieren

Figure 6.4: SWBLI on the 0° meridian, Ogive



a) CFD Mach contour plot b) Schlieren

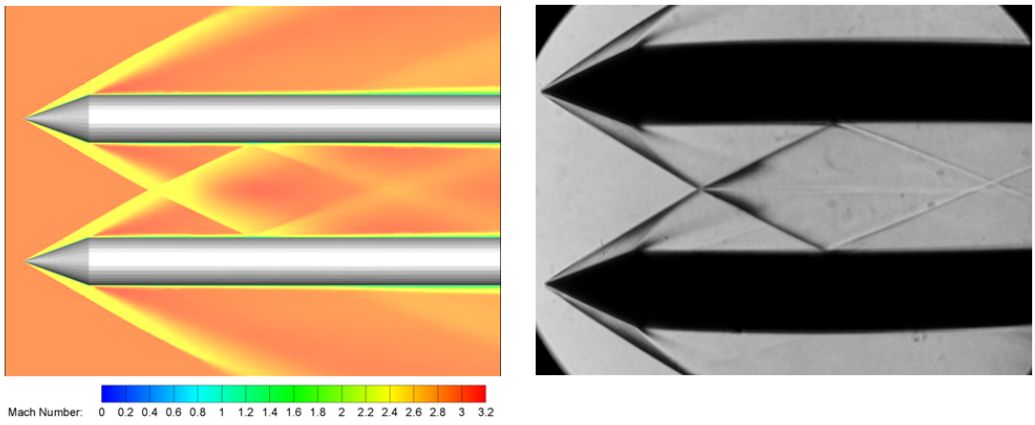
Figure 6.5: Magnified SWBLI on the 0° meridian, Ogive



a) 16mm b) 19mm

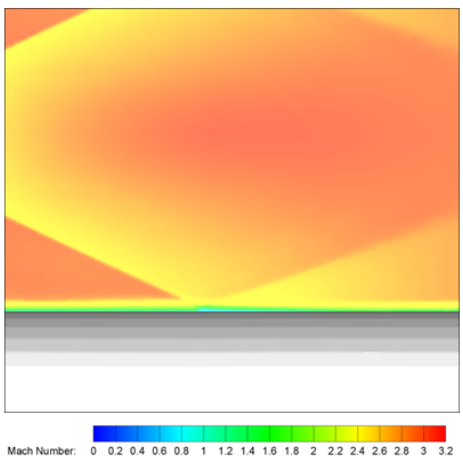
c) 22mm d) 25mm

Figure 6.6: Mach number contour line plots transverse to the axis of the cylinder, Ogive (sub-captions indicate the axial distances from the nose)



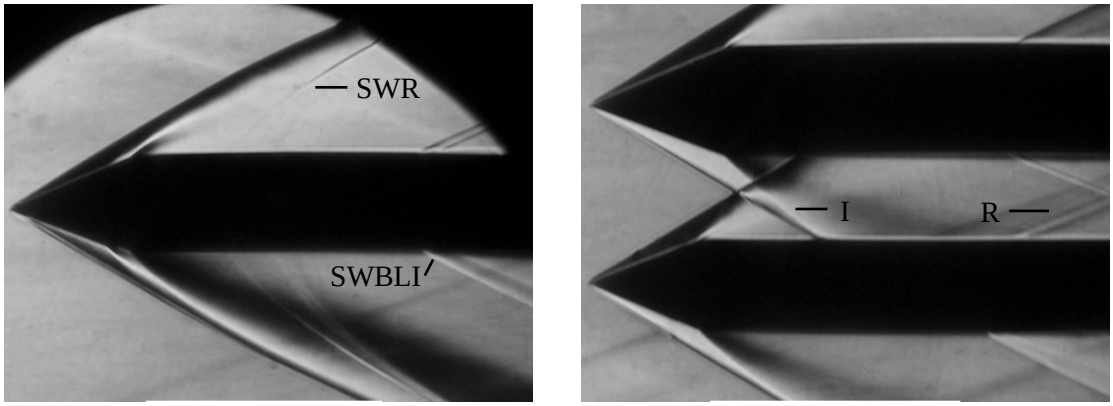
a) CFD Mach contour plot b) Schlieren

Figure 6.7: SWBLI on the 0° meridian, Cone



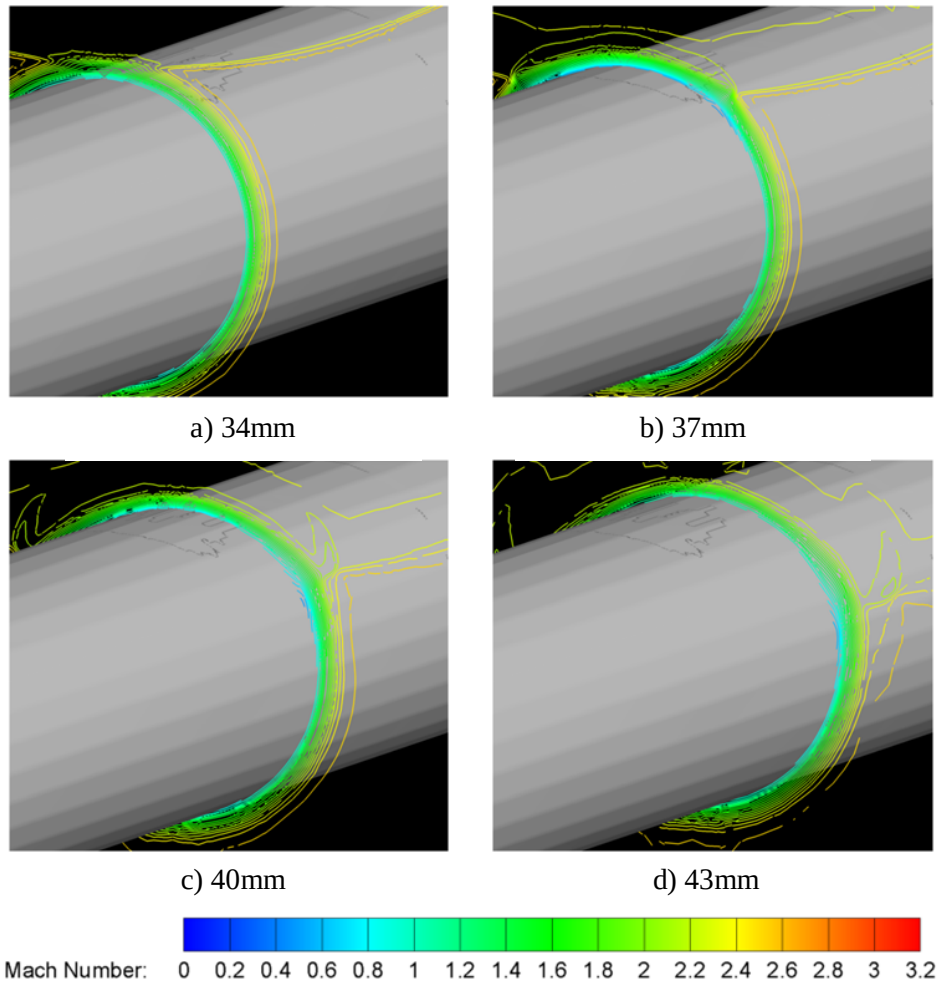
a) CFD Mach contour plot b) Schlieren

Figure 6.8: Magnified SWBLI on the 0° meridian, Cone



a) 90° meridian b) 135° meridian

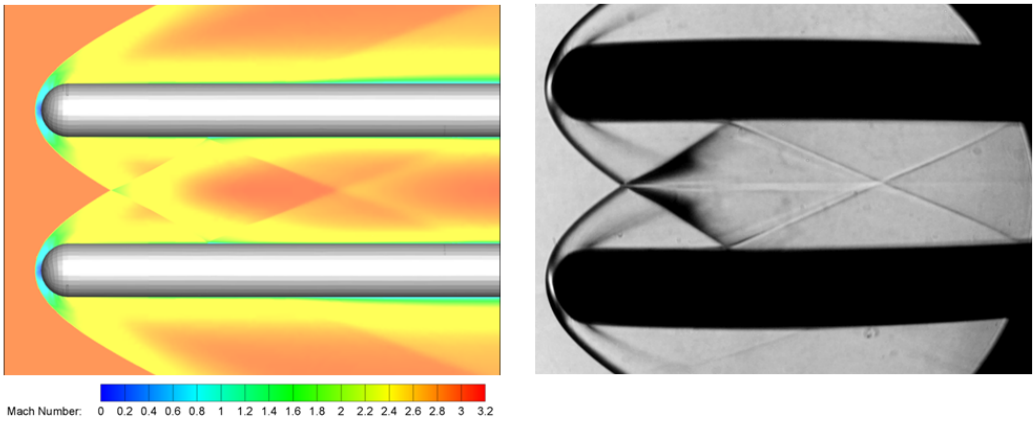
Figure 6.9: SWBLI on the 90° and 135° meridians, schlieren images, Cone



a) 34mm b) 37mm

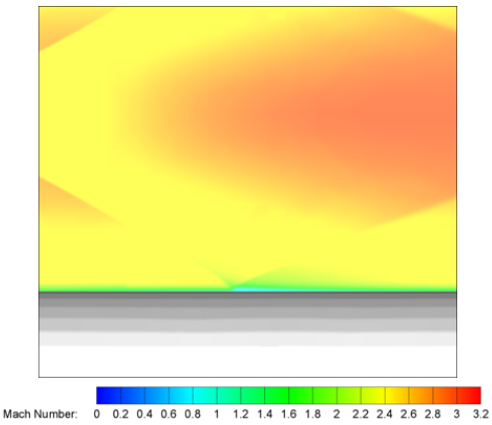
c) 40mm d) 43mm

Figure 6.10: Mach number contour line plots transverse to the axis of the cylinder, Cone



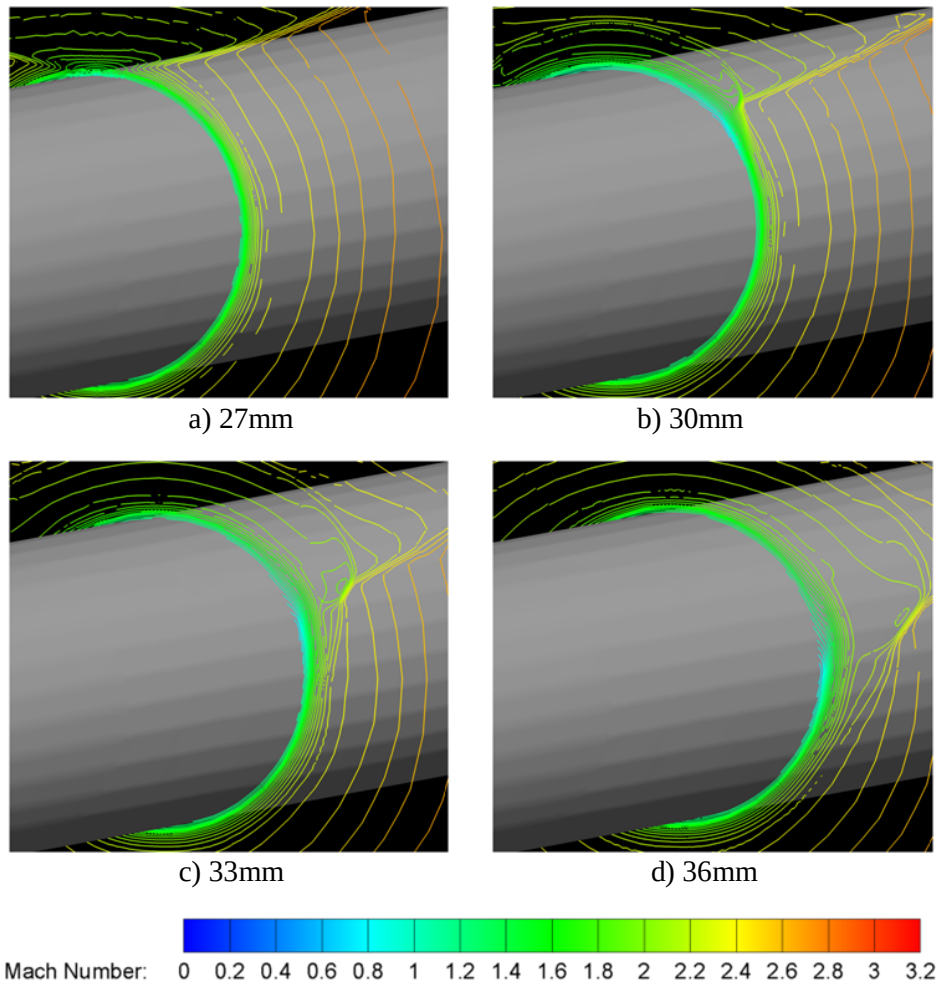
a) CFD Mach contour plot b) Schlieren

Figure 6.11: SWBLI on the 0° meridian, Hemisphere



a) CFD Mach contour plot b) Schlieren

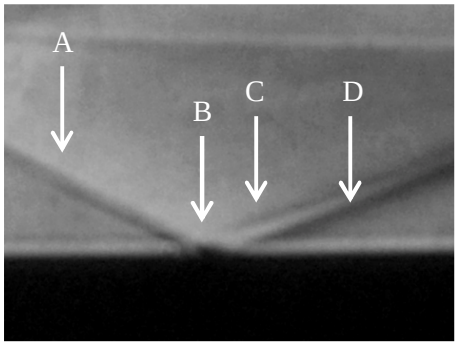
Figure 6.12: Magnified SWBLI on the 0° meridian, Hemisphere



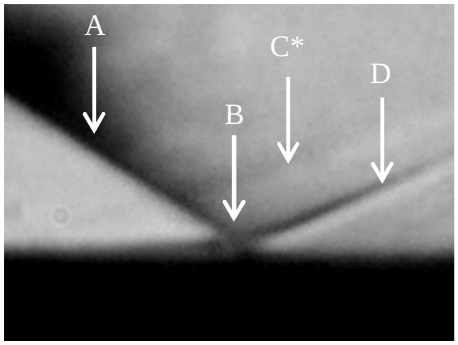
a) 27mm b) 30mm

c) 33mm d) 36mm

Figure 6.13: Mach number contour line plots transverse to the axis of the cylinder, Hemisphere



a) Cone



b) Hemisphere

A – Incident Shock Wave

B – Separation Bubble

C – Separation Shock Wave

D – Re-attachment Shock Wave

* The separation shock wave in this instance is a series of weak compression waves and hence is less visible than the other shock waves in the image.

Figure 6.14: SWBLI overview for the separated flows

Figure 6.14 shows a magnified view of the SWBLI generated by the conical (Figure 6.14a)) and hemispherical (Figure 6.14b)) nose profiles on the windward side of the cylinder. The numerical data for the conical (Figure 6.8a)) and hemispherical (Figure 6.12a)) shows good agreement with the wind tunnel data (Figure 6.8b) and Figure 6.12b)). All of the basic characteristics of an SWBLI presented in Figure 3.11 in section 3.8.1 are present in the SWBLI. The incident shock wave (A) impinges upon the boundary layer and causes the boundary layer to separate due to the adverse pressure gradient across the shock wave. The presence of subsonic flow within the boundary layer allows the higher pressure behind the shock wave to propagate upstream (flow reversal) which causes the boundary layer to separate upstream of the impingement point of the incident shock wave. The separation of the boundary layer temporarily alters the angle of inclination of the flow (with respect to the surface of the cylinder) and a shock wave, known as the separation shock wave (C) is formed. The separated flow (B) eventually re-attaches to the surface, altering the angle of inclination of the supersonic free stream, in the same way as the separation shock wave does, and another shock wave is formed (D). Due to their concave orientation, both the separation and re-attachment shock waves are compressive shock waves as shown in Figure 3.1 in section 3.1. The compressive nature of the shock is therefore responsible for the observed reduction in Mach number across the shock wave in the various CFD contour plots that have been presented.

As highlighted in the caption of Figure 6.14b) the separation shock wave resulting from the hemisphere SWBLI generator is not as well defined by the schlieren optical system as the corresponding shock wave generated by the conical SWBLI generator. The main reason for this lack of definition is the fact that for the conical case the separation shock wave is a single shock wave caused by the deformation of the boundary layer (the separation bubble). For the hemispherical case the change in the profile of the boundary layer is far less pronounced and hence a series of compression waves form rather than one solitary shock wave. A similar result was noted by Gai and Teh (2000) where the reflected shock wave off the SWBLI consisted of a coalescence of compression waves within the SWBLI. This graduated separation bubble is due the strong upstream influence of the SWBLI as seen in the thickening of the boundary layer upstream of the SWBLI in Figure 6.15.

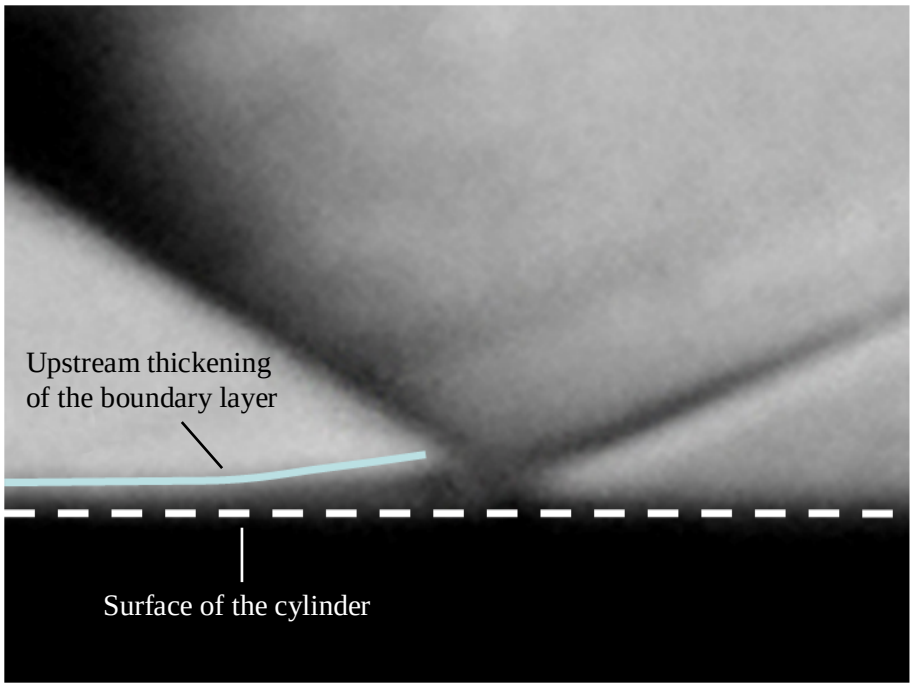


Figure 6.15: Upstream influence of the SWBLI, Hemisphere

The data for the ogival profile (Figure 6.4 and Figure 6.5) shows a weaker interaction more in keeping with the SWBLI shown in Figure 3.12. The weak nature of the incident shock wave does not separate the boundary layer and an incident-reflected shock wave pattern is established. This is also visible from the transverse contour plots of Figure 6.6 which show very little distortion of the boundary layer at any point on the cylinder, upstream or downstream of the shock impingement point.

For the conical SWBLI generator extra wind tunnel test were conducted with the models rotated so as to examine the flow field from differing angles. These results are presented in Figure 6.9 where the interaction is viewed from two different angles. In Figure 6.9a) the SWBLI along the 90° meridian is presented. The reflection (SWR) of the two conical shock waves (emanating from the two conical

SWBLI generators) is visible as is the SWBLI further downstream. When compared to the SWBLI along the 0° meridian (Figure 6.7) the interaction is less defined due to the diminishing strength of the incident shock wave as the leeward side of the cylinder is approached. Moving further around the cylinder to the 135° meridian (Figure 6.9b)) where an interesting observation can be made. The incident shock wave (I) is seen to impinge on the surface of the cylinder however there is no visible reflected wave off the surface. The reflected wave (R) that is visible is more than two cylinder diameters downstream of the impingement point and corresponds to the SWBLI occurring on the windward surface (0° meridian). The reflected wave corresponding to the appropriate incident shock wave is not visible because the viewing plane of the schlieren is tangential to that of the reflected wave.

The boundary layer on the surface of the cylinder shown in Figure 6.14 is observed to be considerably thinner when compared to boundary layers along flat surfaces at similar free stream Mach numbers. It is accepted that cylindrical boundary layers are generally thinner than boundary layers that develop on the surface of a flat plate (Tutty et al., 2002). At the leading edge of the cylinder the boundary layer will behave more like that of a Blasius flow while further downstream the boundary layer departs from the flat plate case. This can be shown graphically by solving and plotting the results of equation 3.2 for ξ, the nondimensional parameter quantifying the nature of the boundary layer, for the length of the cylinder common to all of the SWBLI generators.

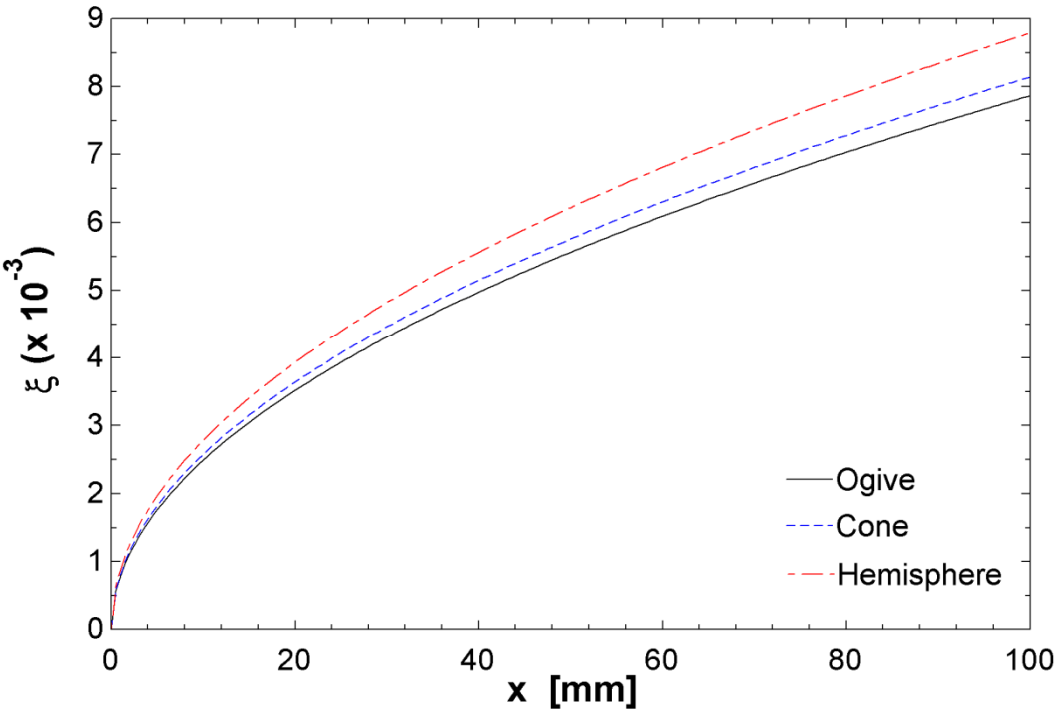


Figure 6.16: Variation of the nondimensional boundary layer parameter (ξ) along the length of the cylinder

Figure 6.16 shows a rapid rise in the value of ξ with axial position. This rise becomes more gradual as the boundary layer propagates down the cylinder. Since the Mach number behind the incident shock wave was different for each of the nose profiles, the Reynolds number (based on the aforementioned Mach number) will be different for each profile as well. Although the value of ξ may seem small ($8.8 \cdot 10^{-3}$ at its maximum for all three profiles) it is worthwhile to note the rapid change in the value of ξ corresponding to a change in the behaviour of the boundary layer from the Blasius to the cylindrical case.

The development of the interaction around the cylinder is shown in Figure 6.6, Figure 6.10 and Figure 6.13 by means of contour plots taken transverse to the axis of the cylinders. For the conical and hemispherical profiles, moving downstream and around the circumference of the cylinder yields a reduction in the size of the separated region until it is no longer visible at approximately the 135° ray. This reduction in separation can be attributed to the decreasing strength of the interaction towards the lee-side of the cylinder as follows: The conical shock wave impinges on the windward side of the cylinder and the induced velocities within the shock direct the flow onto the surface and a SWBLI occurs. As the shock moves around the cylinder (toward the lee-side) the velocity components of the flow within the shock direct the flow away from the surface of the cylinder resulting in a weaker shock wave interacting with the boundary layer. One of the main causes of boundary layer separation

is the adverse pressure gradient across the shock wave which causes flow reversal through the subsonic portion of the boundary layer (Anderson, 2007). As the adverse pressure gradient across the shock wave diminishes with shock strength, so will the likelihood of boundary layer separation. The lee-side effects are further explored in section 6.2.5.

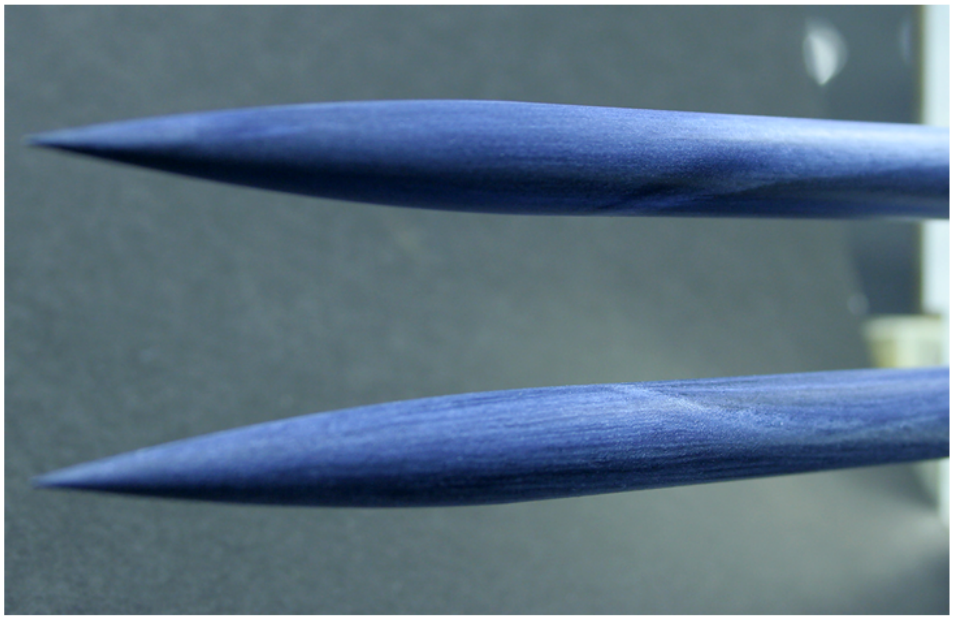
Another important feature shown in the transverse contour plots is the thickening of the boundary layer upstream of the shock wave impingement point. As shown in these plots, the boundary layer begins to thicken somewhere in the order of two boundary layer heights (± 3mm) upstream of the shock impingement point, a result of the upstream propagation of the high pressure behind the incident shock wave through the subsonic section of the boundary layer.

The incident shock waves generated by the ogival nose profiles are observed to be quite weak in nature, where the strength of the shock wave is defined as the magnitude of the pressure ratio across the shock, as seen in Figure 6.4 and Figure 6.5. The large fineness ratio of the ogival profile (outlined in section 4.1.4) deflects the flow by a shallower angle and results in a weaker shock wave forming. This result is shown graphically for conical shock waves (a cone simply being a specific body of revolution) in Figure 3.4. For any particular Mach number a shallower turning angle will result in an incident shock wave being less likely to detach from the nose of the profile due to its reduced strength. The larger fineness ratio also results in the reduction of the overall drag co-efficient of the profile (Morrison, 1962). A reduction in drag implies that the body disturbs the surrounding free stream less and hence a weaker shock wave is formed. It follows intuitively that a weak incident shock wave would result in a weaker SWBLI. Returning to the definition of the shock wave's strength being the magnitude of the pressure gradient across the shock, a weaker shock wave would generate a smaller adverse pressure gradient upon impingement on the boundary layer compared to a stronger shock. This diminished adverse pressure gradient would not cause the boundary layer to separate as readily and hence the whole SWBLI would become less pronounced. This result is evident in Figure 6.4 where very little interaction between the incident shock wave and boundary layer is visible.

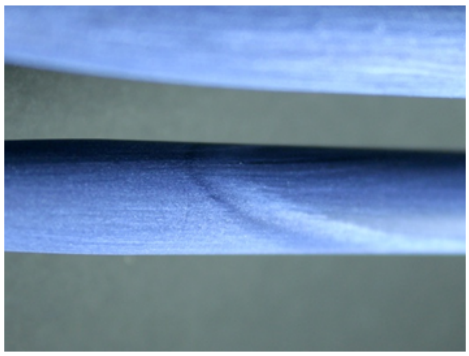
Figure 6.11 and Figure 6.12 show the SWBLI resulting from the hemispherical profiles. Immediately obvious is the strength of the incident shock waves formed by the spherical nature of the profiles, as well as the detached nature of the shock wave from the nose of the profile itself. This is an expected result due to the bluntness of the hemispherical profile as outlined in section 4.1.4. The large adverse pressure gradient established across the incident shock wave separates the boundary layer more readily than compared to the ogival and conical profiles. The resultant SWBLI is the largest and most pronounced of the three profiles – as seen from the large separated regions on the surface of the cylinder in Figure 6.11 - Figure 6.13.

6.2.3 Surface Flow Patterns

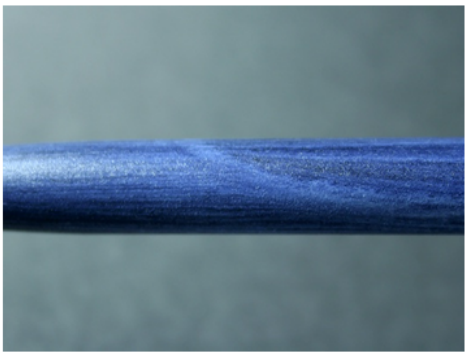
Figure 6.17 through Figure 6.32 are the oil-flow visualisation images collected from the supersonic wind tunnel and corresponding images generated by the CFD simulations. A full discussion of the images in question is presented towards the end of this section (section 6.2.3).



a) Oil surface flow overview



b) Windward view



c) Side view

Figure 6.17: Oil surface flow visualisation, Ogive

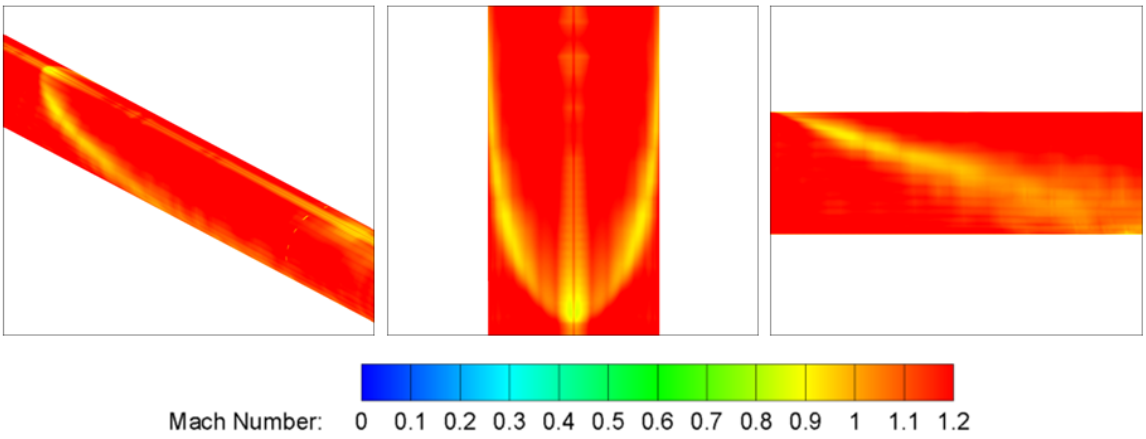
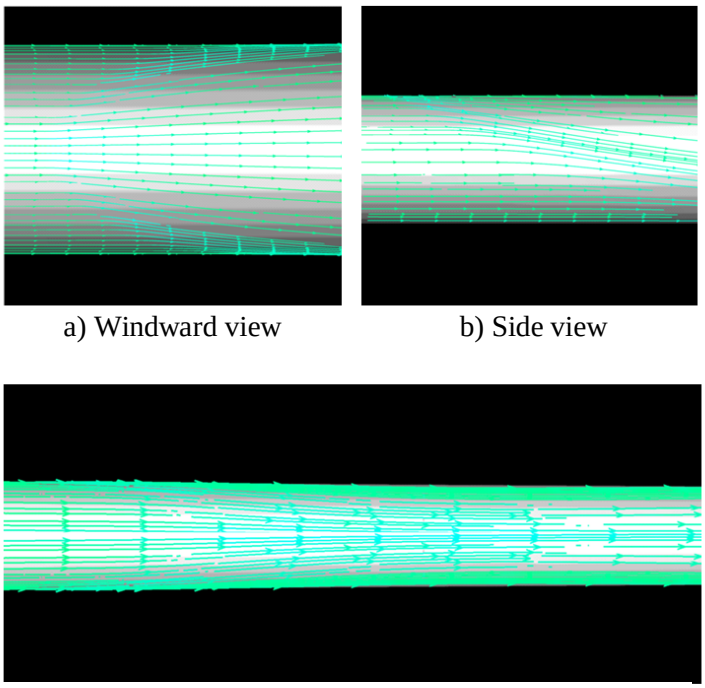


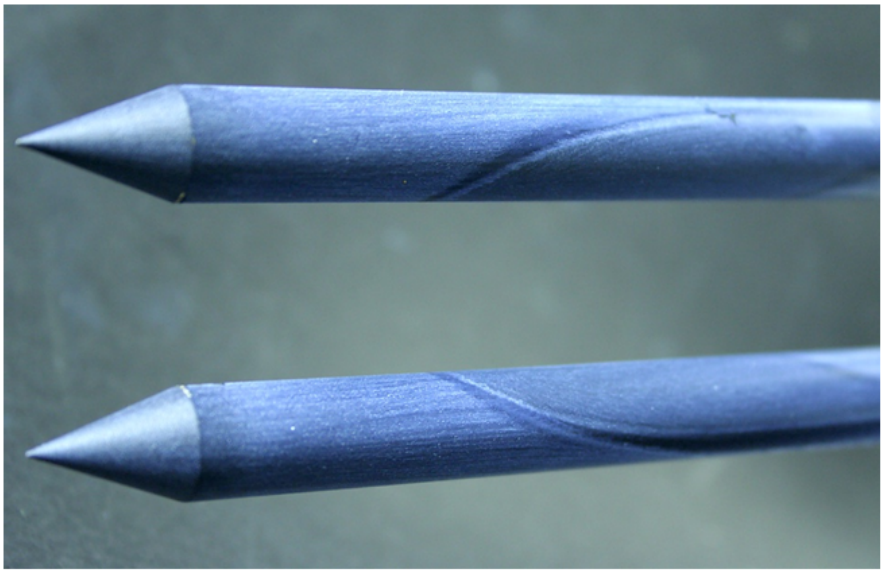
Figure 6.18: CFD Surface flow visualisation, Ogive



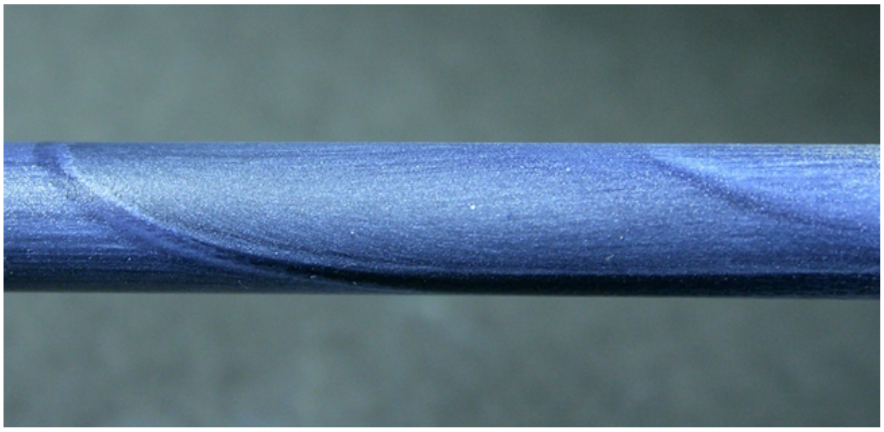
a) Windward view b) Side view

c) Leeward view

Figure 6.19: CFD Surface flow streamlines, Ogive



a) Oil surface flow overview



b) Side view



c) Windward view



d) Leeward view

Figure 6.20: Oil surface flow visualisation, Cone

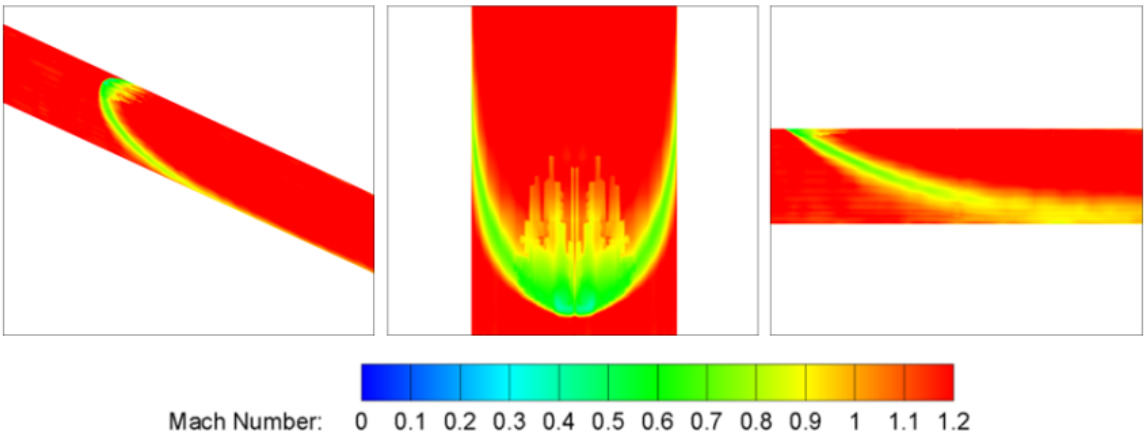
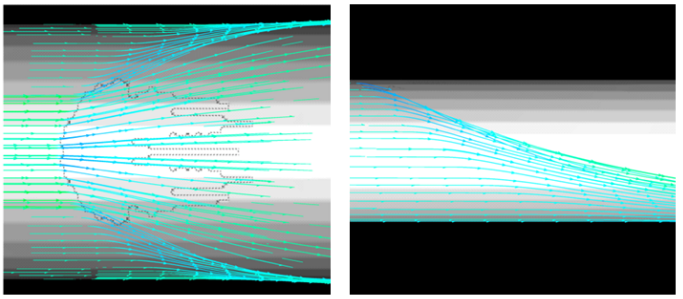
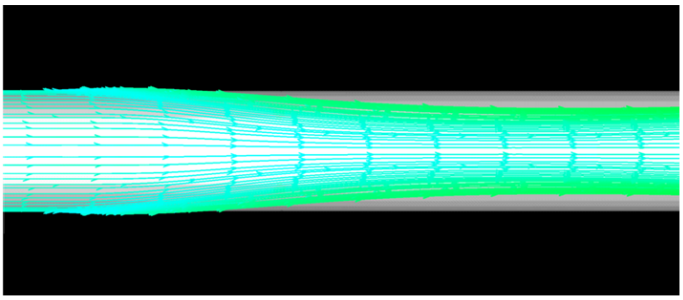


Figure 6.21: CFD surface flow visualisation, Cone



a) Windward View b) Side View



c) Leeward View

Figure 6.22: CFD Surface flow streamlines, Cone

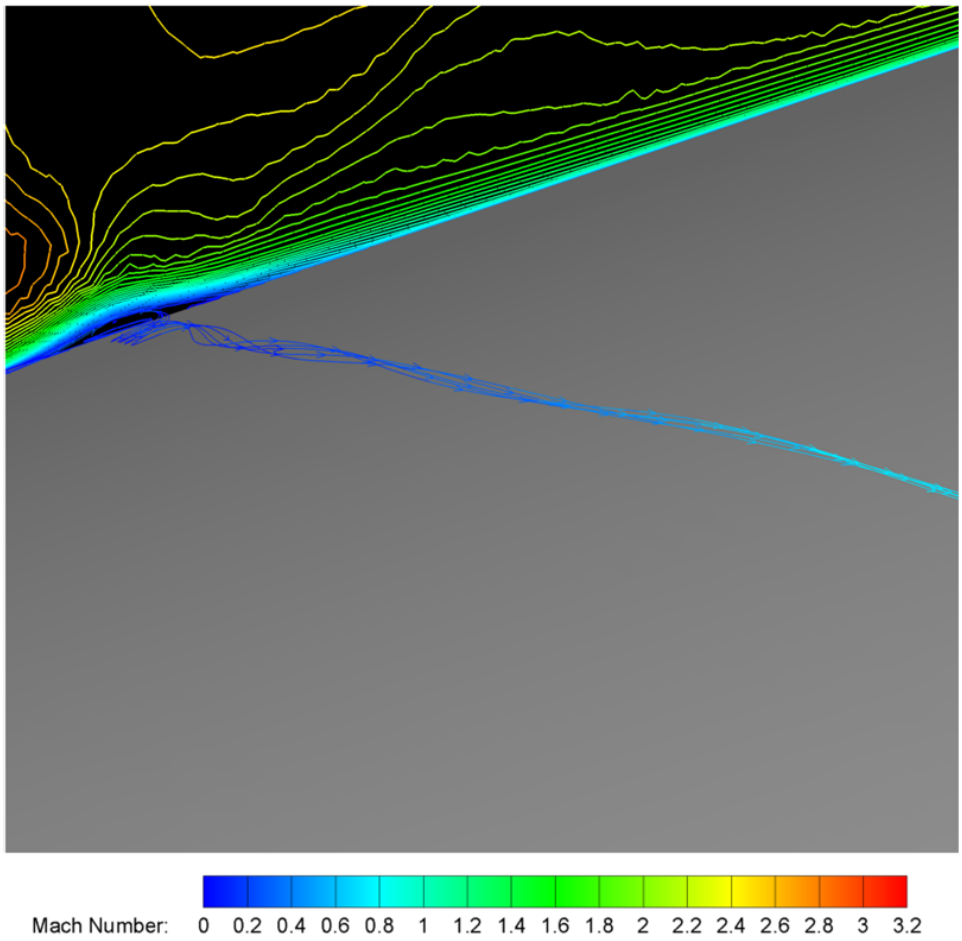
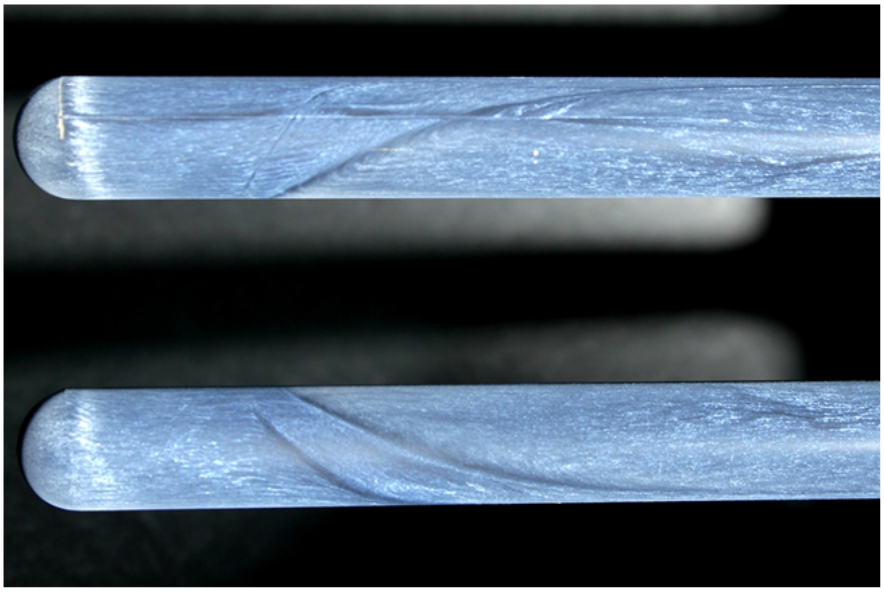
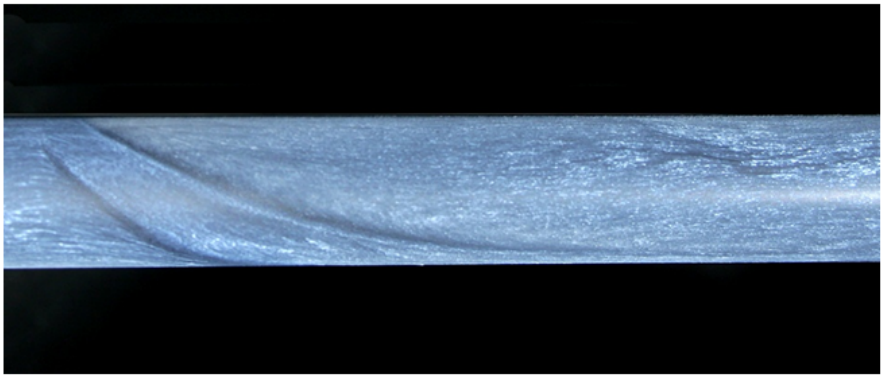


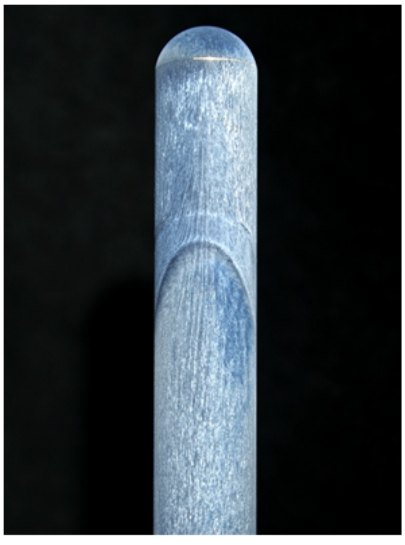
Figure 6.23: Streamlines within the separated region, Cone



a) Oil surface flow overview



b) Side view



c) Windward view



d) Leeward view

Figure 6.24: Oil surface flow visualisation, Hemisphere

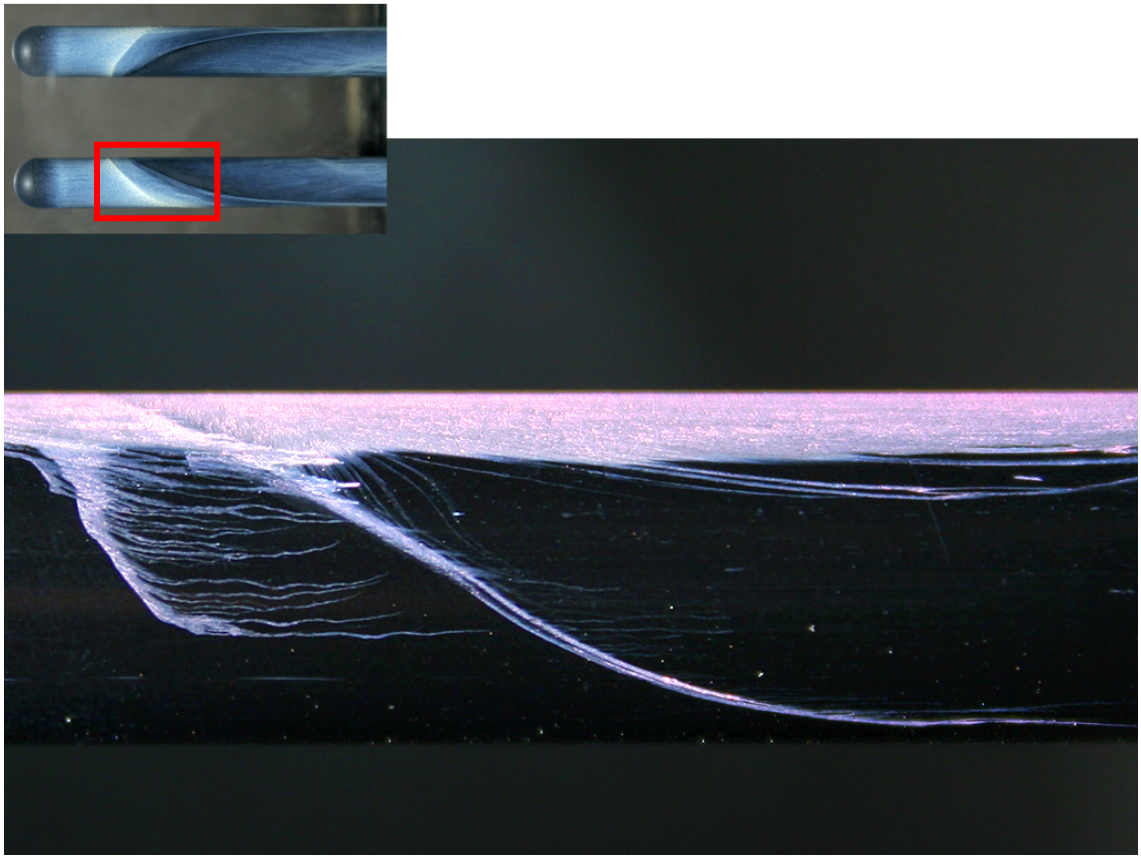


Figure 6.25: Oil surface flow within the separated region, Hemisphere

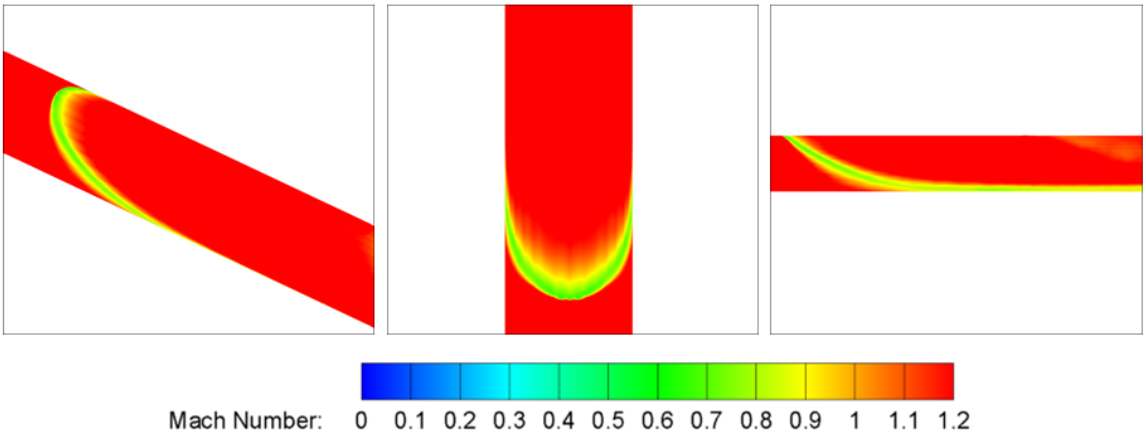
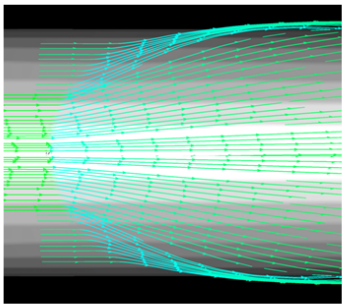
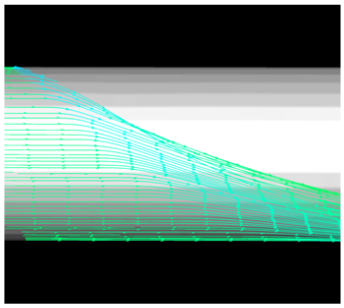


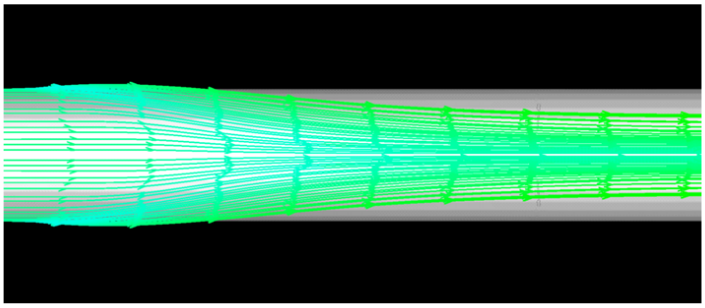
Figure 6.26: Surface flow visualisation, Hemisphere



a) Windward View



b) Side View



c) Leeward View

Figure 6.27: CFD Surface flow streamlines, Hemisphere

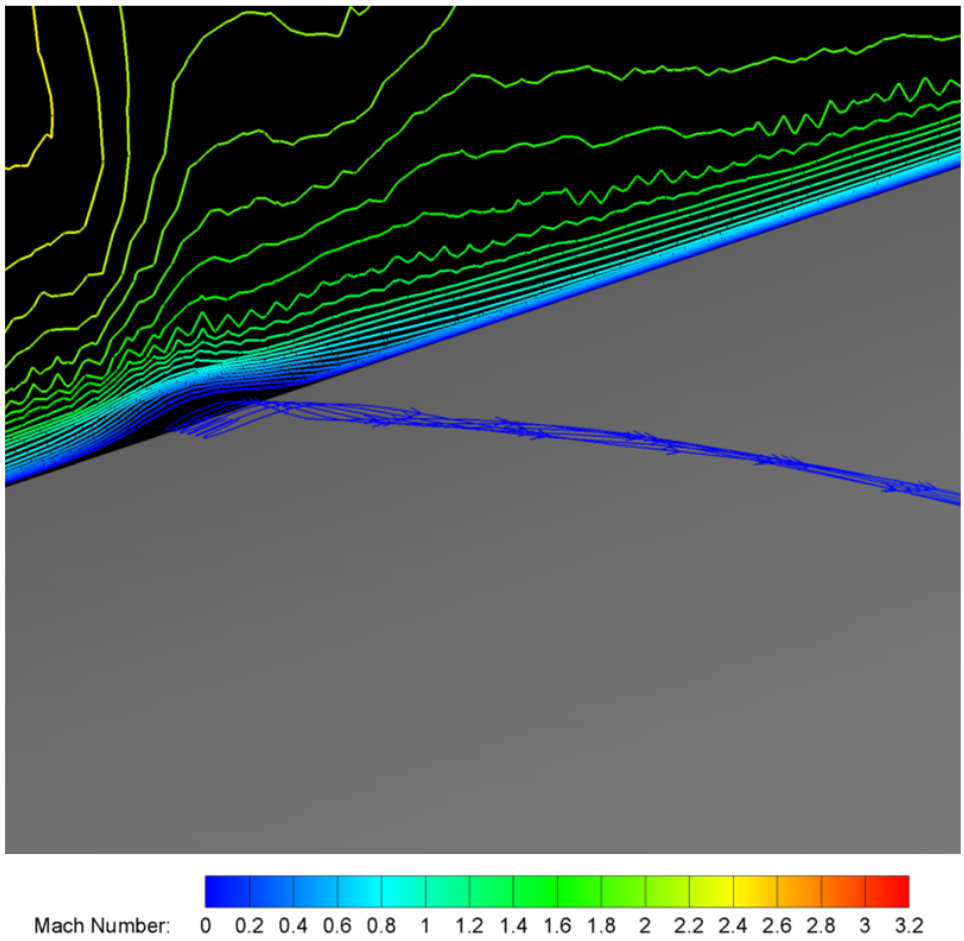


Figure 6.28: Streamlines within the separated region, Hemisphere

The surface flow patterns in Figure 6.17, Figure 6.20 and Figure 6.31 were generated using the transformer oil-based mixture described in section 4.1.3. This mixture was not suitable for post-wind tunnel blow down analysis with the hemispherical SWBLI generator as the wind tunnel shut down ruined the pattern; hence the images in Figure 6.31 were captured during a wind tunnel blow down. By using the paraffin-based mixture described in section 4.1.3 it was possible to analyse the surface flow patterns of the hemispherical SWBLI generator after the blow down (see Figure 6.24) in the same manner as the other profiles (Figure 6.17 and Figure 6.20).

The ogival SWBLI generator does not produce a shock wave of sufficient intensity to separate the flow yielding a surface flow pattern that is inline with characteristics shown in Figure 3.12. Figure 6.17 does not show a clean, dark horseshoe region on the surface of the cylinder symptomatic of a separated flow. This result is replicated in the numerical work shown in Figure 6.18 where instead of a dark horseshoe (indicative of a very low Mach number resulting from flow separation) on the surface, there is a yellow area which corresponds to a Mach number of 0.8 - 1.0. This region

corresponds to the subsonic layer within the SWBLI which is in direct contact with the surface of the cylinder itself.

For the conical (Figure 6.20 and Figure 6.21) and the hemispherical (Figure 6.24 and Figure 6.26) cases there is clear evidence of flow separation on the surface of the cylinder. In the surface flow patterns generated by the hemispherical SWBLI generator two separation lines are evident. This matches the work done by Brosh et al. (1985) with the exception of the persistance of the separation down the length of the leeward side of the cylinder. This discrepancy is due to the presence of the large expansion fan off the convex corner of the wedge used in the study by Brosh et al. The expansion fan in question was observed to straighten the flow leading to the disappearance of the separation lines. In the current study such an expansion fan is not present. For the conical case the flow features observed in the wind tunnel are well replicated by the CFD simulations with the separation bubble following the footprint of the incident shock wave on the surface of the cylinder. This is an expected and somewhat intuitive result since the impingement of the shock wave on the boundary layer is directly responsible for the separation of the boundary layer. The horseshoe shape and symmetry about the vertical plane of the separated region is clearly evident in both cases as is the path of the separated region around the circumference of the cylinder. The CFD simulation for the hemispherical SWBLI generator does not predict the secondary separation line. Both the conical and hemispherical surface patterns showed the presence of strong cross flows within the boundary layer. Although these cross flows are not clearly visible in Figure 6.20 and Figure 6.24 due to the limited contrast between the colour of the mixture and the surface of the cylinder, the lateral deflection of the surface streamlines in Figure 6.22 and Figure 6.27 is a direct consequence of the cross flows. For illustrative purposes the separation (S) and re-attachment (R) points on the surface flow patterns have been highlighted in Figure 6.29.

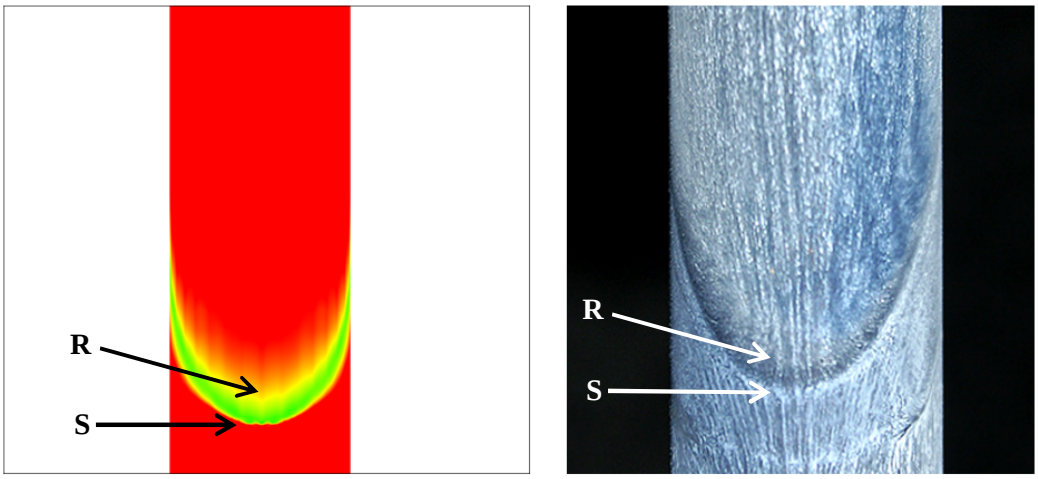


Figure 6.29: Separated region on the windward surface of the hemispherical SWBLI generator

The curved shape of the separated region is due to the conical nature of the incident shock wave impinging on the surface of the cylinder. Similar shaped separated region have been observed in other work involving similar geometries by Gai and Teh (2000), Panov (1968) and more applicably Kussoy et al (1980) and Brosh et al (Brosh et al., 1985). On the 0° meridian the axis of the separation bubble is normal to the axis of the cylinder and the direction of the freestream. Crossing the span of the cylinder the separated region begins to bend and ultimately becomes parallel to the direction of the free stream at the 90° meridian of the cylinder. Due to the conical shape of the incident shock wave and the curvature of the surface of the cylinder, the separated region reduces in size with increasing meridian angle, eventually disappearing around the 135° ray. This result matches that of Gai and Teh (2000) and Panov (1968) which yielded a separation bubble whose size diminished with increasing span wise position along the plate. The surface flow pattern observed in Figure 6.29 also has a lot in common with, both in terms of the nature of the SWBLI generator geometry and results, with the work undertaken by Kussoy et al (1980). The major separation along the 0° plane deteriorating until eventually disappearing around the 135° meridian mentioned above is a result that is strikingly similar to that of Kussoy et al in their work in 1980.

The streamline plots shown in Figure 6.19, Figure 6.22 and Figure 6.27 for the ogival, conical and hemispherical profiles respectively give a clearer insight into the nature of the flow along the surface in the vicinity of the SWBLI. The deflection of the streamlines shows the presence of the circumferential pressure gradient or cross-flows that are established within the boundary layer when acted upon by a shock wave (Brosh et al., 1985, Morkovin et al., 1952). The magnitude of the deflection is observed to increase with increasing shock wave intensity with the ogival SWBLI generator causing a noticeably smaller deflection than that of the hemispherical SWBLI generator. For the conical and hemispherical SWBLI generators the streamlines also show the pronounced sweeping around of the windward boundary layer to the lee-side of the cylinder. This is an important characteristic which will be further discussed in section 6.2.5.

The flow within the separated region has been shown numerically in Figure 6.23 and Figure 6.28 for the conical and hemispherical profiles respectively. A spiral vortex exists within the separated region as it (the separated region) wraps around the cylinder. No such flows exist for the ogival profile since the incident shock wave does not separate the flow. Figure 6.25 shows the flow within the separated region of the hemispherical SWBLI generator by means of oil flow visualisation. The oil mixture was only placed on the windward side of the cylinder and upstream of the SWBLI. Figure 6.23 and Figure 6.28 show the point of impingement of the incident shock wave on the windward side of the cylinder with the nose of the cylinder out of frame in the lower left hand corner. The spiral like trajectories of the flow within the separated region are a combination of the two main pressure gradients resulting from the SWBLI; the adverse pressure gradient across the incident shock wave and the

circumferential pressure gradient within the cylindrical boundary layer. These pressure gradients are illustrated schematically in Figure 6.30.

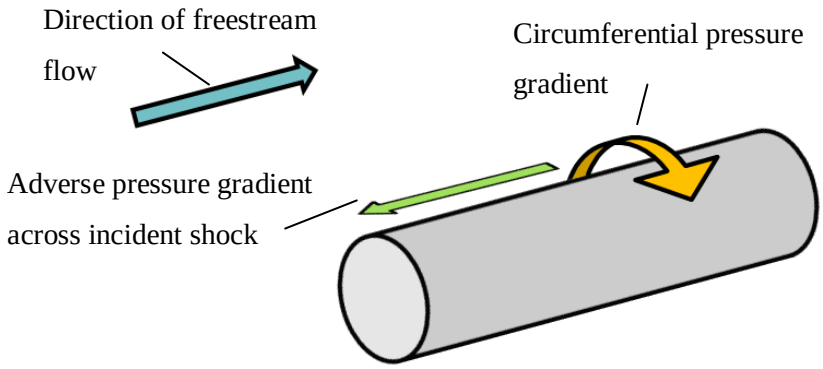
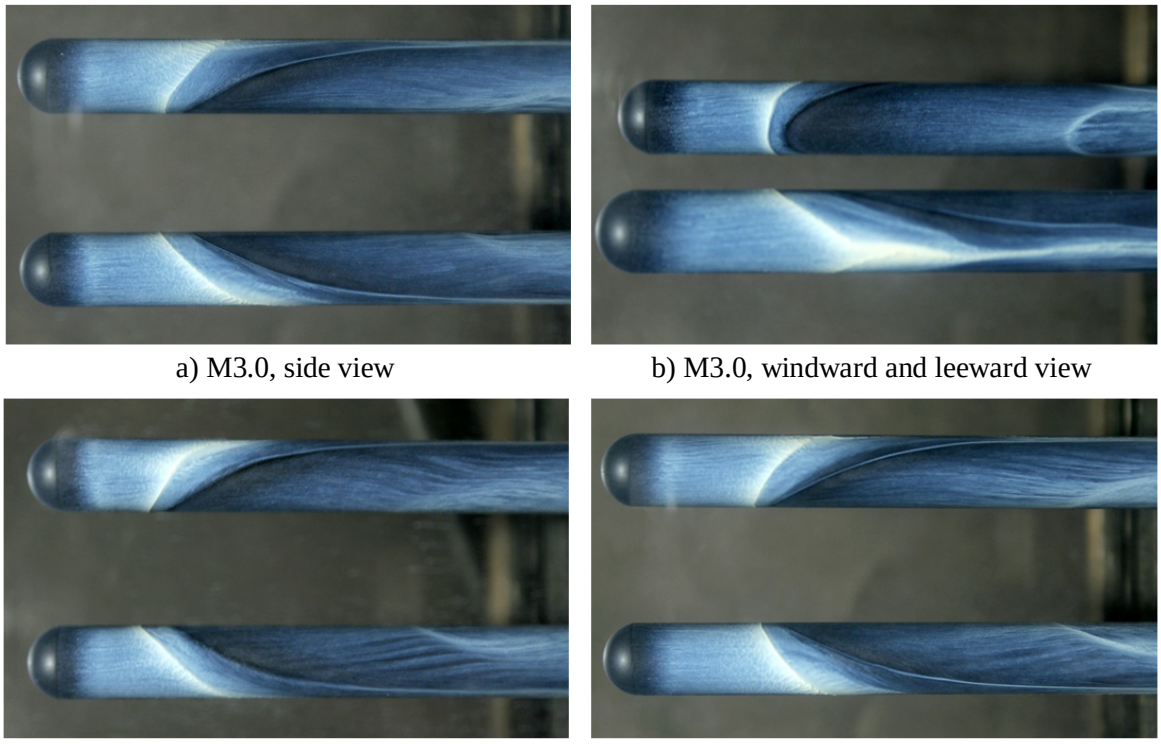


Figure 6.30: Schematic illustration of the pressure gradients resulting from the SWBLI

The adverse pressure gradient (the green arrow in Figure 6.30) causes the flow within the separated region to flow upstream until the point of boundary layer separation is reached. At this point the flow then turns around, due to the diminishing strength of the adverse pressure gradient, and flows downstream as normal. During this upstream propagation the flow has been acted upon by the circumferential pressure gradient (the yellow arrow in Figure 6.30) within the boundary layer and so has been circumferentially displaced away from the centre line of the cylinder. This process repeats until the pressure gradients are insufficiently strong to alter the trajectory of the flow within the separated region. The net result is a spiral like flow within the separated region which transports some of the air on the most windward side of the cylinder (0°) around the circumference. This is clearly evident in Figure 6.25 where the oil mixture that was originally along the 0° meridian has been displaced around the circumference by the flow within the separation bubble.

Due to the behaviour of the transformer oil-based surface flow visualisation mixture on the hemispherical SWBLI generator, several tests were run were the oil surface flow patterns were photographed during a wind tunnel blow down. These photographs are shown in Figure 6.31.



a) M3.0, side view

b) M3.0, windward and leeward view

c) M2.5, Side View

d) M3.2, Side View

Figure 6.31: Oil surface flow visualisation during a blow down, Hemisphere

The surface flow patterns shown in Figure 6.31 clearly show the existence of the two separation lines arising from the SWBLI. Analysis of Figure 6.24 and Figure 6.25 also show traces of the dual separation lines. These lines were evident in every wind tunnel test conducted using the hemispherical SWBLI generator and the transformer oil-based surface flow visualisation mixture. The behaviour of this feature was also investigated across a range of Mach numbers (M2.5, M3.0 and M3.2). The mixture would form the white line shown in Figure 6.31 throughout the duration of the blow down and as soon as the tunnel began to shut down, the mixture would be released from its suspension and run down the cylinder.

By superimposing an oil surface flow image onto a schlieren image (to scale) it is possible to further analyse the surface flow patterns generated by the hemispherical SWBLI. Figure 6.32 is a superposition of Figure 6.12b) and Figure 6.31a) and shows a noticeable relationship between the two separation lines and the thickening of the boundary layer upstream of incident shock wave impingement point. The boundary layer begins to thicken where the flow first separates from the surface of the cylinder upstream of the theoretical inviscid impingement point (Anderson, 2007) before the second separation occurs downstream of the intersection between the incident and separation shocks.

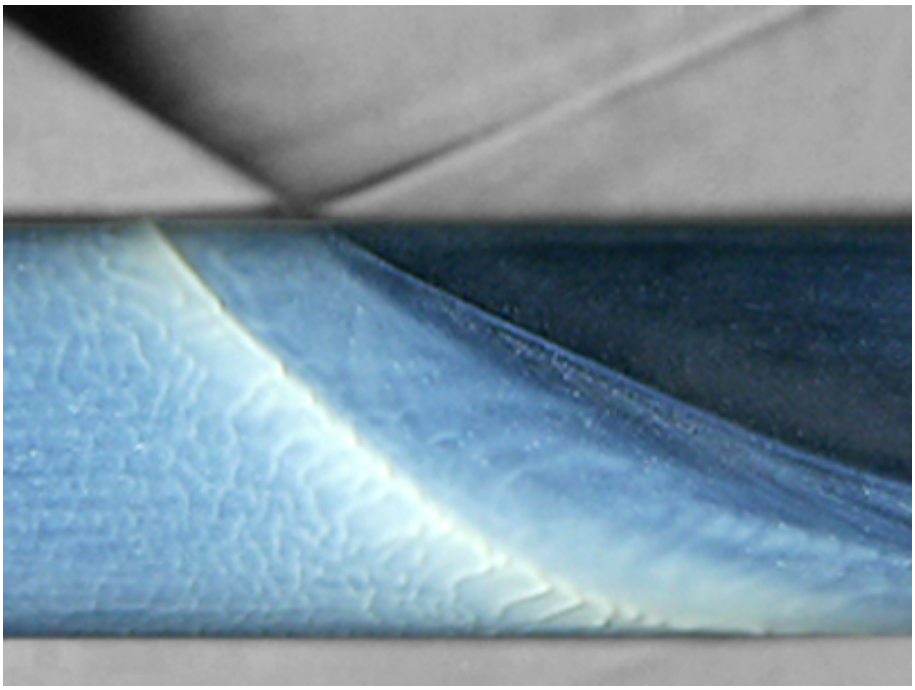


Figure 6.32: Superposition of schlieren and oil surface flow images, Hemisphere

It is also worth noting that the pair of separation lines was not explicitly predicted by the CFD simulation run for the hemispherical case. As a result a higher resolution CFD simulation was run - the full analysis of which is presented in 6.2.6.

6.2.4 Surface Pressure Measurements

Pressure measurements were taken from the surface of cylinders for each of the different nose profiles. These measurements were collected from the numerical data exclusively as it was not practicable to design an interaction grid of sufficient resolution to fit into the SWBLI generators. To fully capture the SWBLI the pitch between pressure orifices would need to be less than 2mm (as shown by Gai and Teh, 2000). This grid could compromise the cylindrical profile and smoothness of the surface and deform the boundary layer itself.

The surface pressure plots (Figure 6.33, Figure 6.34 and Figure 6.36) are taken along the length of the cylindrical section of the SWBLI at 30° intervals. The pressure is specified in terms of a pressure ratio which is the local pressure at each point normalised with respect to the free stream reference static pressure. From the surface pressure plots it is possible to calculate the co-ordinates of the separation and attachment lines and hence the length of the separated region.

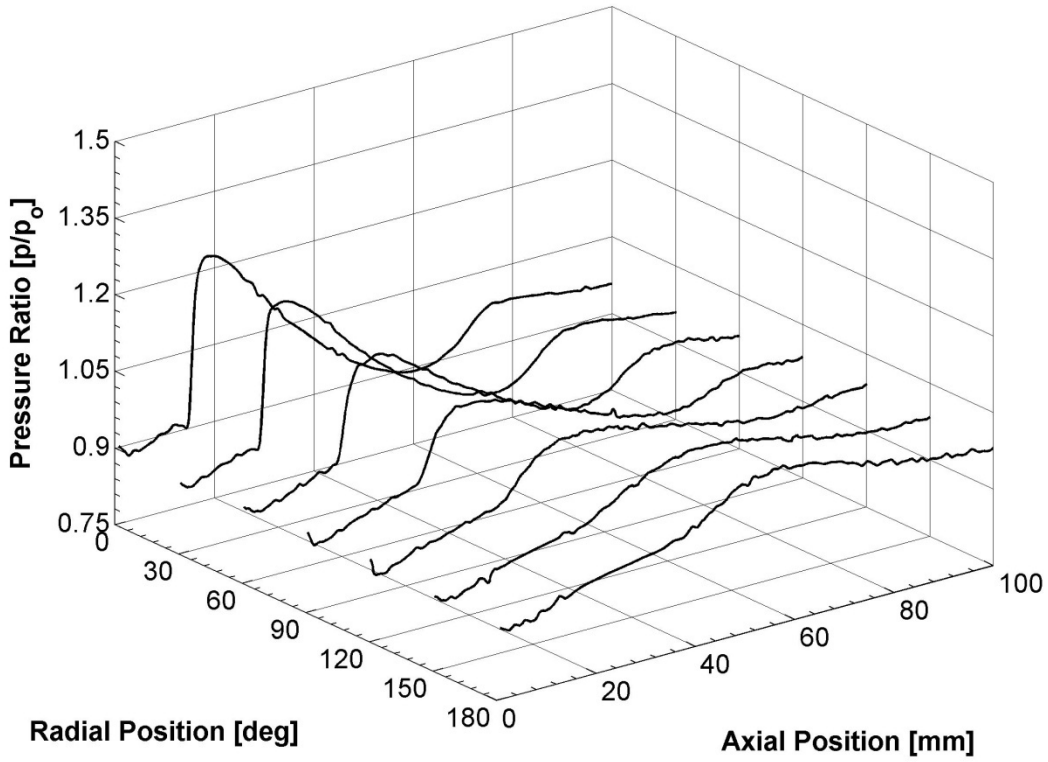


Figure 6.33: Surface pressure distribution, Ogive

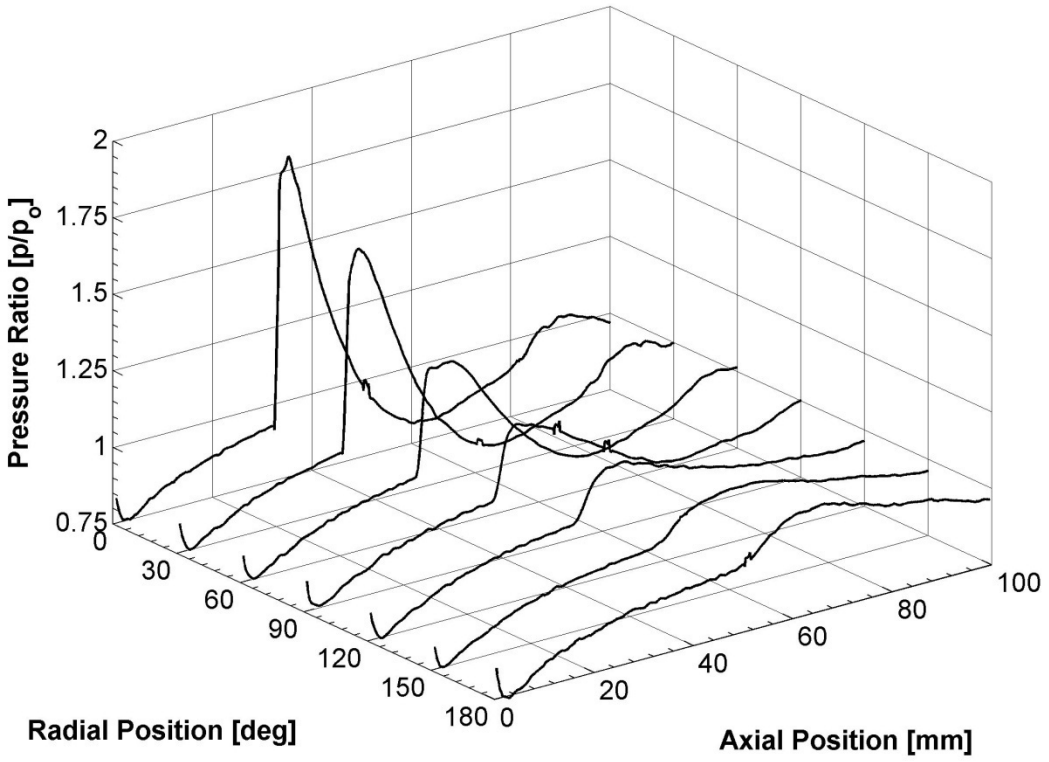


Figure 6.34: Surface pressure distribution, Cone

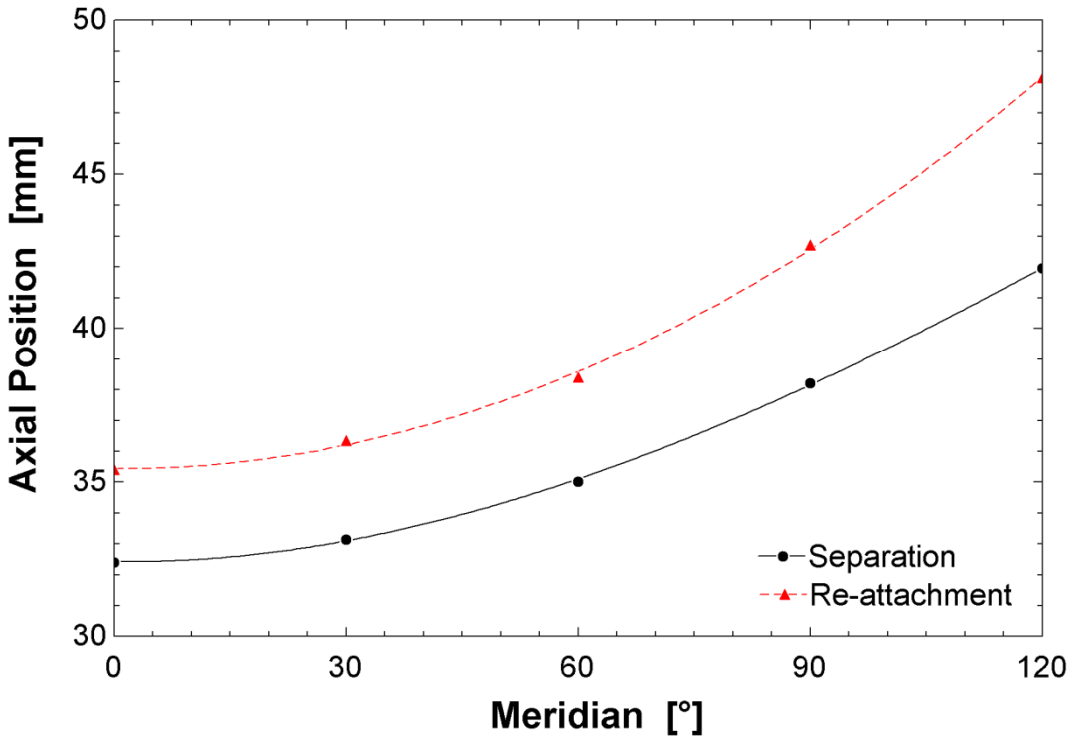


Figure 6.35: Separation and attachment co-ordinates for SWBLI, Cone

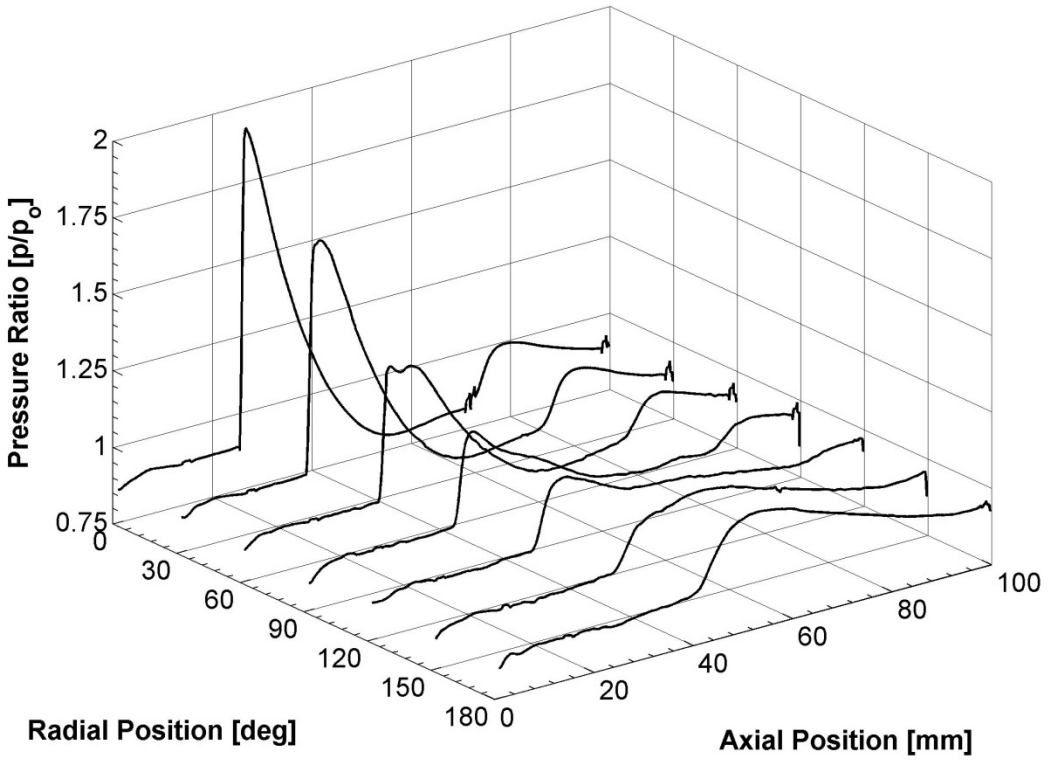


Figure 6.36: Surface pressure distribution, Hemisphere

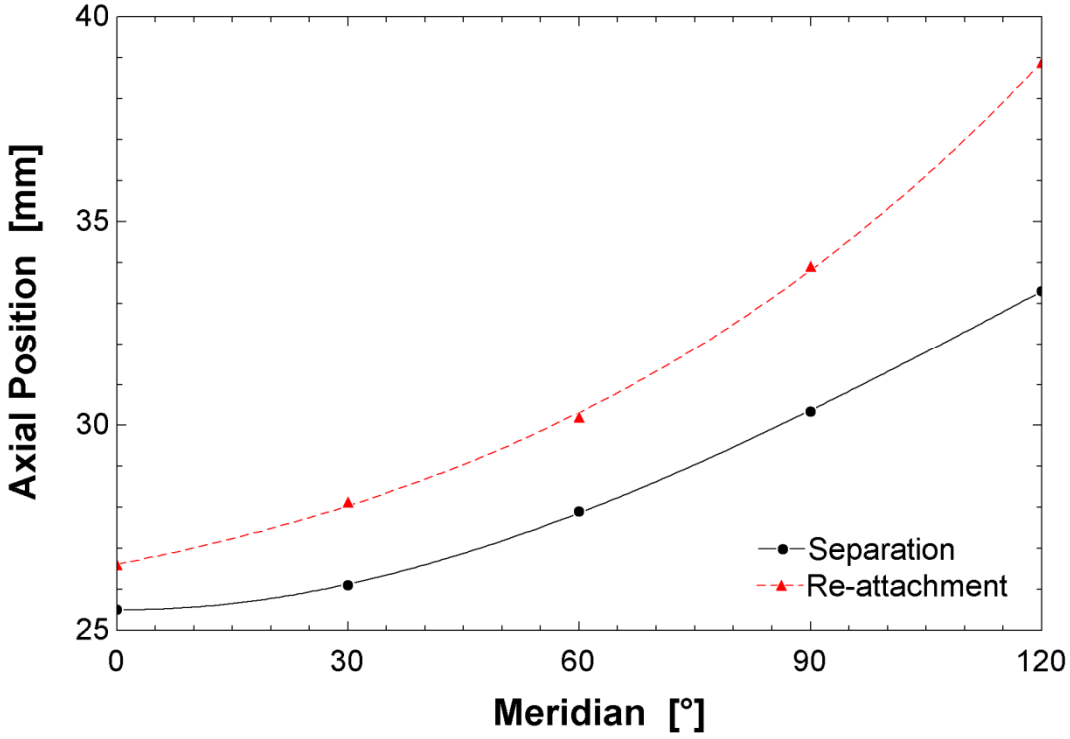


Figure 6.37: Separation and attachment co-ordinates for SWBLI, Hemisphere

Analysis of the surface pressure distribution plots show a distinct increase in pressure ratio that occurs further downstream with increasing meridian angle - a result of the incident shock wave sweeping around the cylinder. This result was noted in works by Gai and Teh (2000), Panov (1968), Kussoy et al. (1980) and Morkovin et al. (1952). Along each of the pressure traces a common trend is evident. Firstly there is a sharp increase in pressure ratio resulting from the separation of the boundary layer. Due to the compressive nature of the separation shock wave, the local pressure will increase at separation owing to the concave deflection of the flow. The pressure ratio then continues to rise until a maximum value is reached downstream of separation. This maximum value is in fact the point at which the boundary layer re-attaches itself to the surface of the cylinder. The re-attachment of the boundary layer forms a compressive shock wave which, as for the separation shock, serves to increase the temperature and pressure of the flow. After re-attachment the pressure ratio returns (decreases) to its original base value.

As the shock wave moves around the cylinder, so the maximum pressure ratio decreases due to the reduction in intensity of the SWBLI. The maximum pressure ratio value is located along the 0° (windward) meridian for each of the profiles although the value does differ due to strengths of the incident shock waves. For the ogival profile the maximum pressure ratio is around 1.2 (read off Figure 6.33), for the conical profile this value increases to 1.8 (Figure 6.34) and for the hemispherical profile the maximum value is observed to be 1.95 (Figure 6.36). The 0° meridian is the first intersection point between the incident shock wave and the surface (boundary layer). The shock wave at this point will be at its strongest and the induced velocity components within the shock will direct the flow directly onto the surface of the cylinder without any yawing of the flow. The conical nature of the incident shock wave means at any meridian angle other than 0° a velocity component that is perpendicular to the axis of the cylinder will exist. This lateral component serves to establish the cross flows found within cylindrical boundary layers and detracts from the axial adverse pressure gradient. An increase in meridian angle results in an increase in the yawing of the flow which is why the maximum pressure ratio decreases around the circumference of the cylinder. On the extreme leeward side of the cylinder ($|\varphi| > 150°$) a small increase in the surface pressure ratio is evident suggesting that the entire region is in a wake of separated flow (Brosh et al. 1985). The presence of cross flows within the boundary layer will cause the rise in pressure ratio in this region (Morkovin, et al., 1952).

For the ogival profile the pressure ratio upstream of the SWBLI remains fairly constant, while for the conical and to a lesser extent the hemispherical profile there is sharp decrease followed by a definite and gradual increase in the surface pressure along the surface of the cylinder. This is due to the fact that where the ogival, conical and hemispherical profiles intersect with the cylindrical section of the SWBLI, as circled in Figure 6.38, an expansion fan forms. As highlighted in section 3.2 an expansion fan will accelerate the flow while decreasing the static properties of the fluid, thus the downstream

pressure will be lower than the pressure upstream of the expansion fan. The end of the expansion fan, represented by the sharp decrease in pressure ratio, coincides with the beginning of the cylindrical section of the SWBLI generator. This location corresponds to the 0mm axial position shown on the axes of Figure 6.33, Figure 6.34 and Figure 6.36. The gradual increase in pressure that follows is due to the establishment of the boundary layer on the cylinder itself. This increase in pressure is far more obvious for the conical profile than for the hemispherical profile due to the strength of the expansion fan. For the hemispherical profile the expansion fan accelerates the flow to around Mach 2.4 (see Figure 6.11b)) while for the conical profile the Mach number behind the expansion fan is almost 3.0 (Figure 6.7b)). The lower Mach number in the hemispherical case is a direct result of the formation of a bow shock wave on the leading edge of the hemispherical profile.

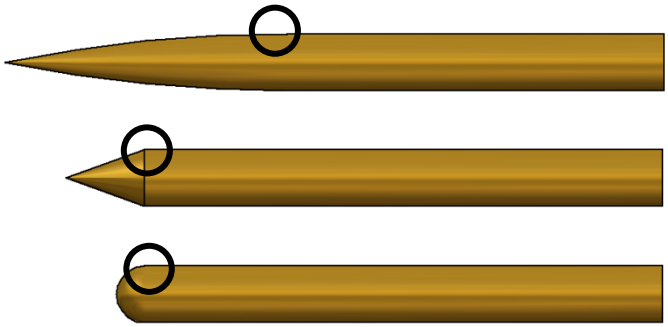
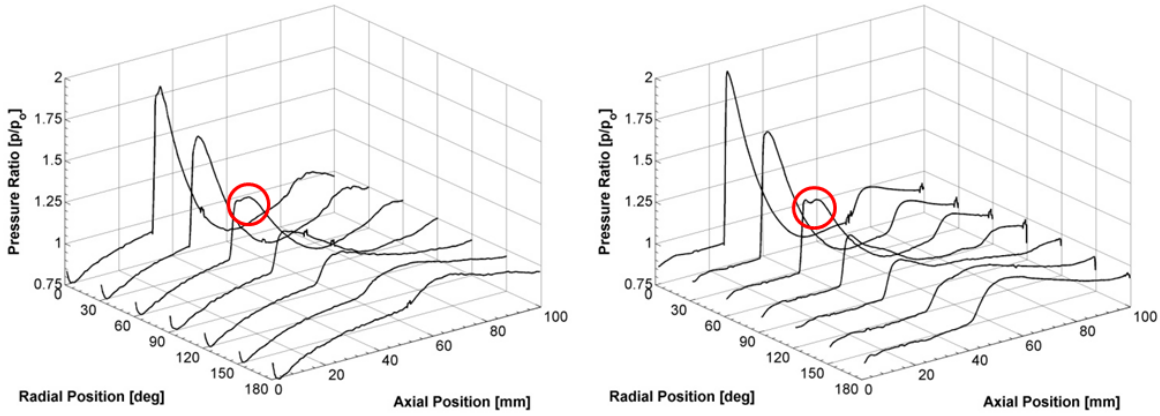


Figure 6.38: Intersection of nose profile and cylindrical section forming an expansion fan

The strength of the incident shock wave affects not only the maximum value of the pressure ratio, but also the extent of the SWBLI. For the conical and hemispherical profiles the SWBLI causes the boundary layer to separate as far as the 135° meridian, while for the ogival profile a smaller affected region is noted on the windward side of the cylinder only (as presented in section 6.2.2 and 6.2.3). This result is also evident in the pressure traces where the abrupt increase in pressure ratio (indicative of flow separation) is seen to flatten out as the value of φ increases. In Figure 6.33 the gradient of the pressure rise decreases notably from the 60° probe to the 90° probe indicating that separation is no longer occurring along the latter. This is known to be the case based on the flow visualisation data collected. The rise in pressure observed in the absence of separation is simply the adverse pressure gradient across the incident shock wave that is impinging on the boundary layer. For the cone (Figure 6.34) and the hemisphere (Figure 6.36) a similar phenomenon is evident, although the transition in these instances occurs between the 90° and 120° probes for the cone and between the 120° and 150° probes for the hemisphere. The very gradual increase and decrease of the pressure ratio along the 180° probe for all three of the profiles tested suggests that a portion of the boundary layer along the

windward side is being swept around to the lee-side of the cylinder. The lee-side effects will be fully addressed in section 6.2.5.

One aspect of the pressure distribution curves requires closer attention – the characteristic shape of the pressure distribution curves on the $\varphi = 60°$ meridian in Figure 6.34 and Figure 6.35. The exact context of these bumps has been highlighted in Figure 6.39. Along the 60° meridian there is the typical increase in pressure as the boundary layer separates, followed by a secondary bump in the pressure ratio. Certain studies (Gai and Teh, 2000) have proposed that the dip in pressure distribution after separation is possibly a secondary separation embedded within the primary separation of the boundary layer. A detailed examination of the reflected shock wave structure around the SWBLI provides an explanation for the double bump in the pressure curve. This analysis and explanation is presented at the end of section 6.2.5.



a) Cone b) Hemisphere

Figure 6.39: Secondary pressure bump location in pressure distribution curves

It is possible to calculate the separation and re-attachment points using the surface pressure data and the criteria governing the separation and re-attachment described above. Once these points are known, the length of the separated region can be calculated. A plot of the processed separation and re-attachment co-ordinates is given in Figure 6.35 for the conical profile and Figure 6.37 for the hemispherical profile. Each of the curves is made up of five discrete points, one for each of the meridian probes, and is fitted with a third order polynomial trend line with a co-efficient of determination exceeding 99.9%. Since the ogival profile did not separate the flow plotting a curve of the separation and re-attachment points would be trivial.

Initial inspection of the separation and re-attachment curves in Figure 6.35 and Figure 6.37 shows the separated region increasing in length with increasing meridian angle – an expected, if not immediately obvious, result given the horseshoe shape of the separated region. Figure 6.40 shows the horseshoe

shaped separated region (taken from the oil surface flow data from the conical profile) with the approximate locations of the windward pressure probes used to generate Figure 6.33 through Figure 6.37. As each of the superimposed meridian lines in Figure 6.40 is studied it is evident that as the meridian angle increases, so does the length of the separated region along the meridian line. This result reflected in the numerically generated separation and re-attachment curves of Figure 6.35 and Figure 6.37 and serves as another validation of the CFD simulations undertaken. Further analysis of the shock wave structure in the vicinity of the SWBLI (presented in a forthcoming section) will show that the separation of the boundary layer actually occurs upstream of the incident shock wave impingement point.

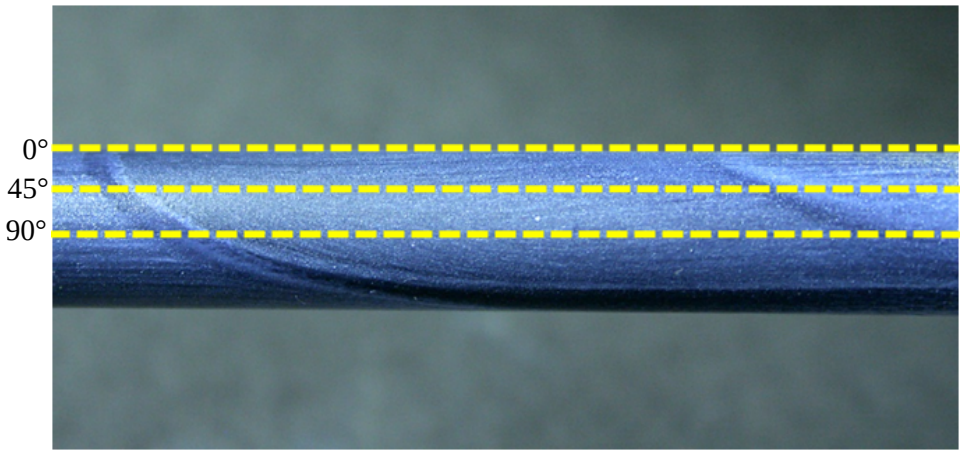


Figure 6.40: Separated region with meridian angles superimposed, Cone

6.2.5 Lee-side Effects and Reflected Shock Wave Phenomena

One of the most interesting phenomena that arises from the SWBLI in question is the behaviour of the flow on the leeward side of the cylinder ($90° < \varphi < 270°$) which is fundamentally different to that of the windward side ($|\varphi| < 90°$). This is best illustrated using the numerical data in the form of an iso-surface. Such surfaces are shown below in Figure 6.41 for the hemispherical case and Figure 6.42 for the ogival and conical cases. It should be noted at this stage that the patchy appearance of the iso-surfaces is the caused by the computational restrictions of the hardware (the graphics card of the computer) and software (Tecplot 360 2009) used for post-processing.

The behaviour of the (incident) shock wave reflecting off the surface of the boundary layer is also significant. Several contour plots and iso-surfaces (which will be expanded upon where required) have been generated to help clarify the nature of the flow in and around the SWBLI.

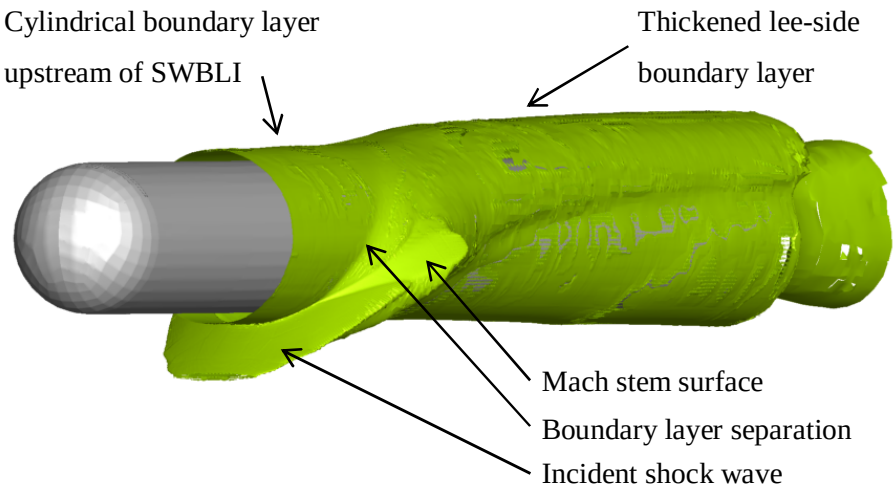
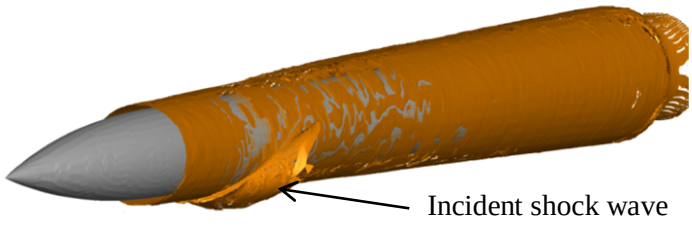
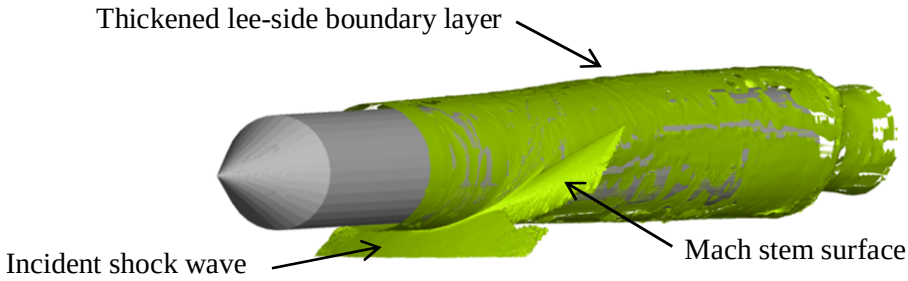


Figure 6.41: Annotated Mach Number (M = 2.4) Iso-surface, Hemisphere



a) Ogive, M = 2.8



b) Cone, M = 2.4

Figure 6.42: Mach number iso-surfaces

Figure 6.41 shows the flowfield around the cylinder resulting from the SWBLI with the incident shock wave propagating from the bottom of the frame. The thickening of the boundary layer is evident in the thickening of the iso-surface along the leeward side of the cylinder. The entire interaction follows the shape of the streamlines generated in Figure 6.27 and is more evidence of the windward-to-leeward surface flow has been established by the SWBLI. The feature labelled as the

‘Boundary layer separation’ is thought to correspond to the most upstream separation line visible in Figure 6.24, Figure 6.25 and Figure 6.31. The upstream separation line is visible in the iso-surface of Figure 6.41 although not in the surface patterns generated by the CFD. This is probably due to mesh refinement restrictions that were enforced in the region of the boundary layer of the flow domain. The planar shock surface that is visible in-between the incident shock wave and boundary layer separation is a Mach stem surface, the detailed structure of which will be discussed later. A Mach stem forms when the angle of incidence between the incident and reflected shock waves is too shallow to reflect off the boundary layer in a regular reflection configuration. Figure 6.42 shows iso-surfaces similar to that of Figure 6.41 for the ogival and conical SWBLI profiles. For the ogival case (Figure 6.42a)) the incident shock wave has relatively little effect on the surface flow of the cylinder and the lee-side boundary layer remains largely unchanged. No Mach stem surface is evident due to the weakness of the incident and reflected shock waves. The conical profile (Figure 6.42b)) results in a flow field similar, although less pronounced, to that shown in Figure 6.41. The boundary layer on the leeward side of the cylinder is visibly thicker than that of the windward side and a small Mach stem surface is also visible. The thickening of the lee-side boundary layer for the cone and hemisphere cases is also evident in the flooded contour plots of Figure 6.7 and Figure 6.11 respectively. Pronounced leeward boundary layer thickening has been noted in several other studies involving cylindrical geometries (Brosh et al. 1985, Morkovin et al., 1952)

On the windward side of the cylinder the incident shock wave induces velocities that are directed toward the surface of the cylinder, and it can be considered that required cancellation of these velocities (since the body is not accelerating) takes the form of the reflected shock wave. As the shock wave passes the 90° meridians the induced velocities from the incident shock wave now have a component away from the cylinder. The resultant flowfield is a lot less physically clear than that of the windward side of the body with the necessity for so-called ‘velocity cancellation’ not certain (Morkovin, et al. 1952). Should the outward component of the shock induced velocity need to be cancelled (either fully or partially) then the mechanism by which such a cancellation would occur would be that of an expansion fan forming along the line of intersection between the shock wave and the cylinder. The expansion fan would seek to turn the flow through a convex angle which would subsequently weaken the shock which generated it. The weakening of the shock wave would create a shadow region that was shielded from the oncoming shock and cause the shock to break up and re-generate some distance away from the body in the $\varphi = 180°$ plane as noted by Morkovin et al. (1952). Figure 6.43 illustrates the amalgamation of the shock wave away from the lee-side surface as well as the aforementioned shadow region very clearly by means of an iso-surface of the density gradient of the incident shock wave.

Figure 6.41 through Figure 6.43 do not show the reflected wave off the windward surface of the cylinder due to the nature of the parameter selected to generate the iso-surface and the position of the surface in the frame. Figure 6.44, showing iso-surfaces of density gradients as per Figure 6.43, is presented to show the reflected wave off the surface of the cylinder from three different angles, a) a plan view of the windward side of the cylinder, b) a plan view of the leeward side of the cylinder and c) a side-on view showing the reflection. This illustration is comparable to that of Figure 6.9 albeit for the hemispherical profile (as opposed to the conical profile of Figure 6.9). The shock wave reflecting off the surface of the cylinders in both cases shows good agreement. For both sets of data the reflected waves have a horseshoe shape to them and show the reflected wave comprising of the separation and re-attachment shock wave of the SWBLI. Due to the complex geometry of the reflected wave, a more thorough analysis is presented further on.

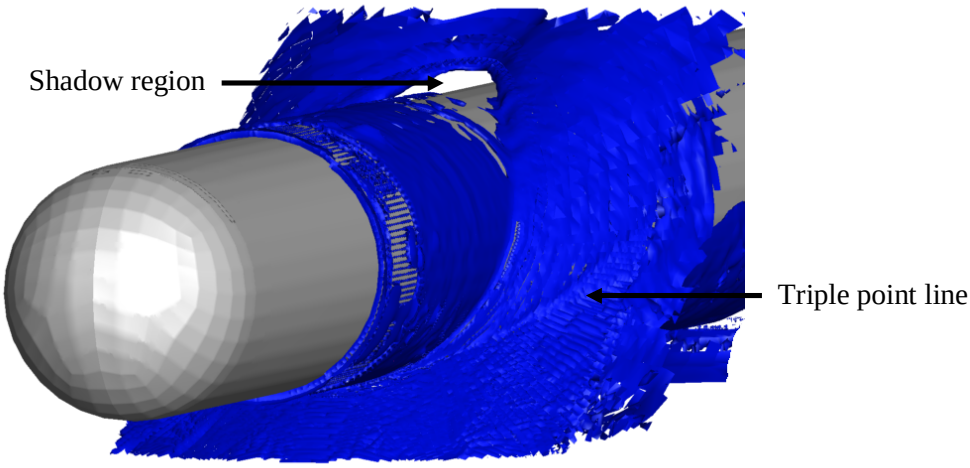


Figure 6.43: Viscous Simulation - Lee-side shock wave, Density gradient iso-surface, DG = 15000

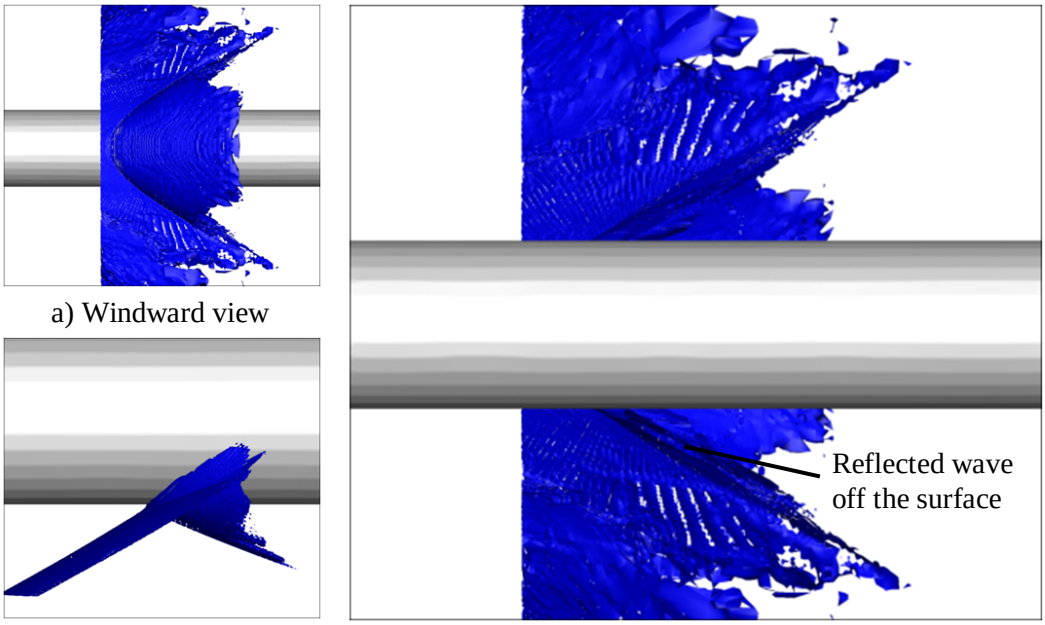
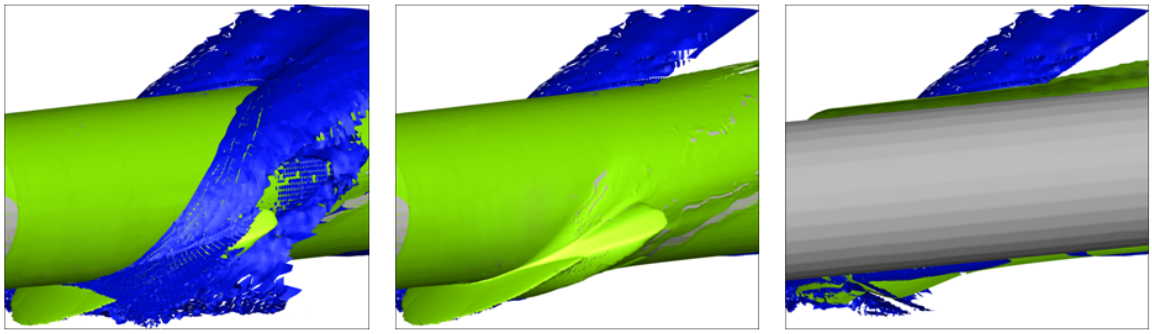


Figure 6.44: Viscous Simulation – Shock wave reflecting off surface of cylinder, Hemisphere

The shadow region shown in Figure 6.43 is caused by the thickening of the boundary layer on the lee-side of the cylinder (Morkovin et al., 1952). The thicker lee-side boundary layer is a combination of the original lee-side boundary layer and the low velocity air being swept in from the windward side of the cylinder – the latter can be seen in the streamlines shown in Figure 6.19, Figure 6.22 and Figure 6.27. This extra air is swept around the cylinder by the cross-flows that have been established within the boundary layer itself. The thickening of the boundary layer deflects the flow in a similar manner to that of a compression ramp causing a series of compression waves to form. These compression waves then coalesce developing into a shock wave away from the surface of the cylinder in the same way as in a two-dimensional SWBLI (Morkovin et al. 1952). The thickening of the lee-side boundary layer is also evident in the damping of the pressure spikes for $\pm 120° < \varphi < 180°$ in the pressure distribution curves in section 6.2.4 above.

In an effort to understand further the nature of the shadow region on the 180° meridian, and to confirm the mechanism by which the shock wave regenerates, the behaviour of the boundary layer in the vicinity of the shadow was investigated. This was achieved by superimposing the blue density gradient iso-surface (as seen in Figure 6.43) and the green Mach number iso-surface (shown in Figure 6.41) together. The resultant composition is shown in Figure 6.45. For the sake of clarity a series of sectioned views are provided. Both of the iso-surfaces are shown in Figure 6.45a), while in Figure 6.45b) the density gradient iso-surface has been cut along the vertical plane of symmetry of the cylinder. In Figure 6.45c) both iso-surfaces have been cut along the symmetry plane to show their position relative to the surface of the cylinder. What is evident from the images in Figure 6.45 is that

the deformed boundary layer and the shadow region in the shock wave fit together perfectly. It is therefore reasonable to assume that the thickened lee-side boundary layer causes the shock wave to re-form some distance away from the surface of the cylinder itself as noted by Morkovin et al. (1952).



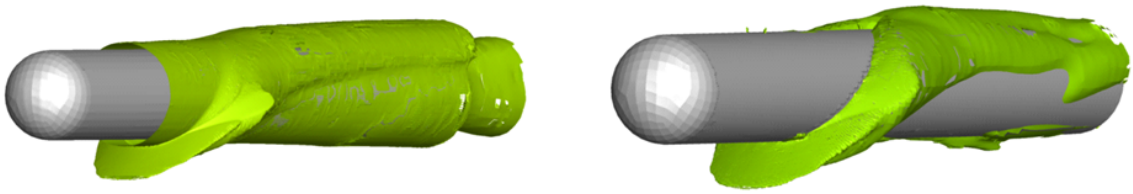
a) Both iso-surfaces visible

b) Density gradient iso-surface cut away

c) Both iso-surfaces cut away

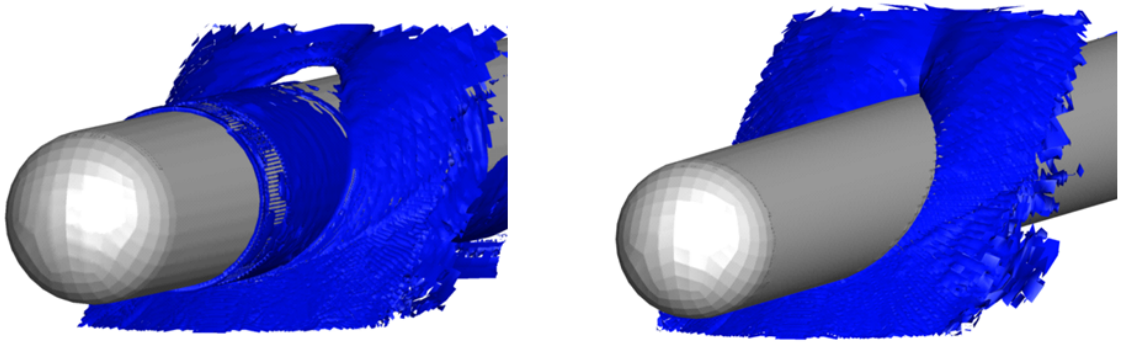
Figure 6.45: Sectioned iso-surfaces, Hemisphere

To further quantify the behaviour of the SWBLI on the leeward section of the cylinder, a CFD simulation was run under inviscid flow conditions. It was decided that the hemispherical SWBLI generator should be utilised as it provided the most pronounced SWBLI of all the geometries tested. All of the mesh and flow conditions were exactly the same as for the viscous cases investigated and described in section 4.2. A series of iso-surfaces and contour plots are presented in Figure 6.46 through Figure 6.50 detailing the differences between the viscous and inviscid solutions.



a) Viscous Simulation – Mach Number Iso-surface, M = 2.4

b) Inviscid Simulation – Mach Number Iso-surface, M = 2.4



c) Viscous Simulation – Density Gradient Iso-surface, DG = 15000

d) Inviscid Simulation – Density Gradient Iso-surface, DG = 15000

Figure 6.46: Effects of viscosity on the lee-side SWBLI, Hemisphere

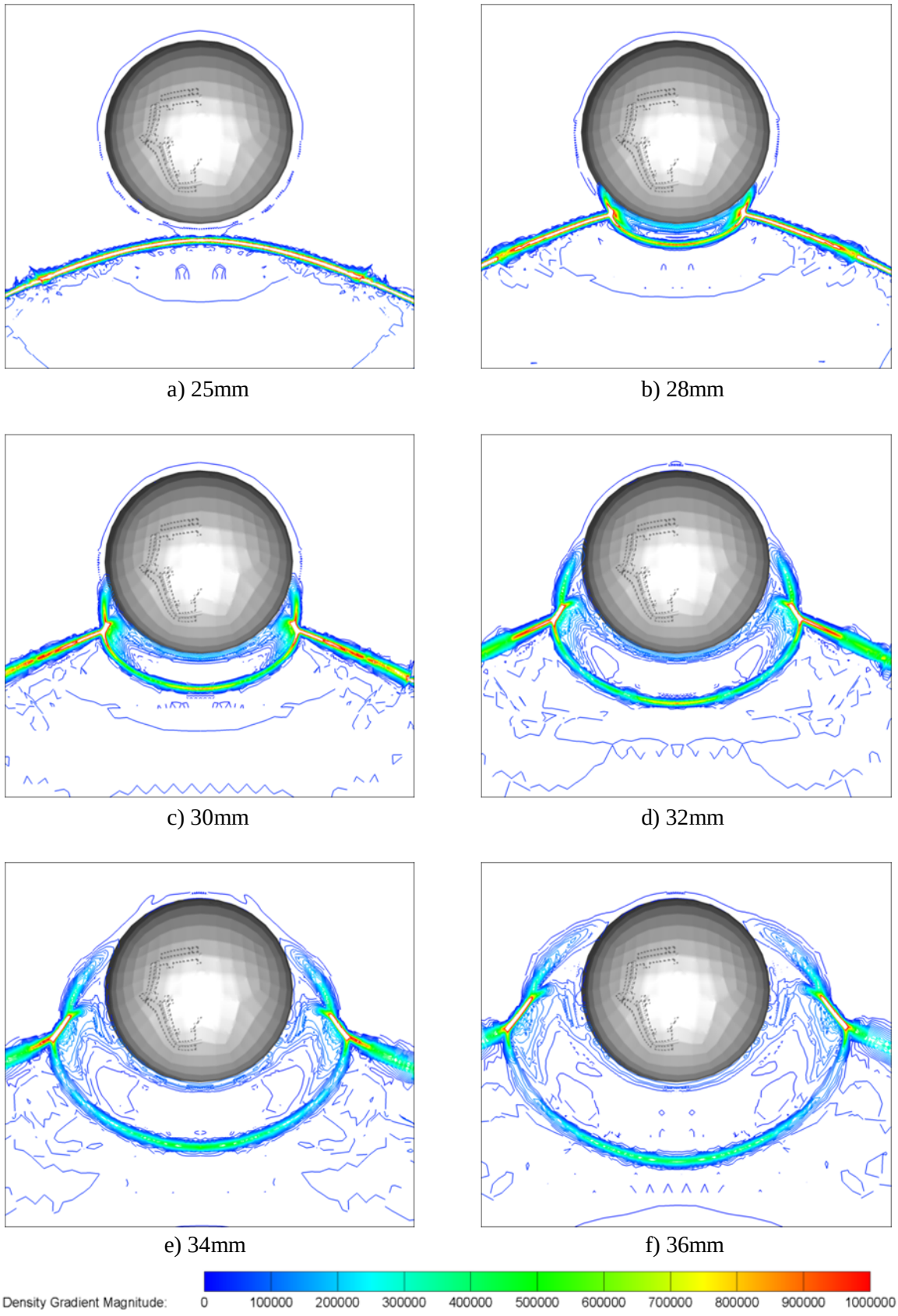
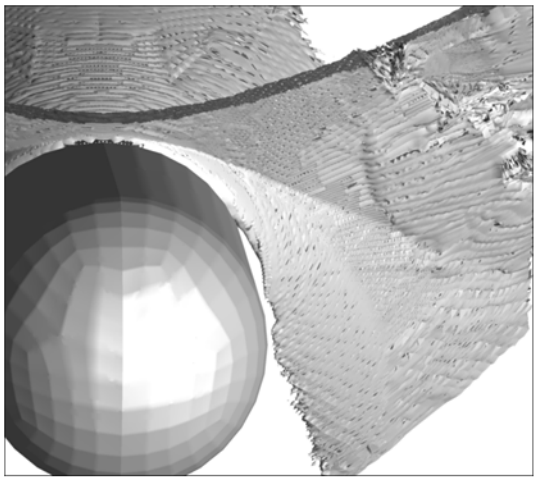
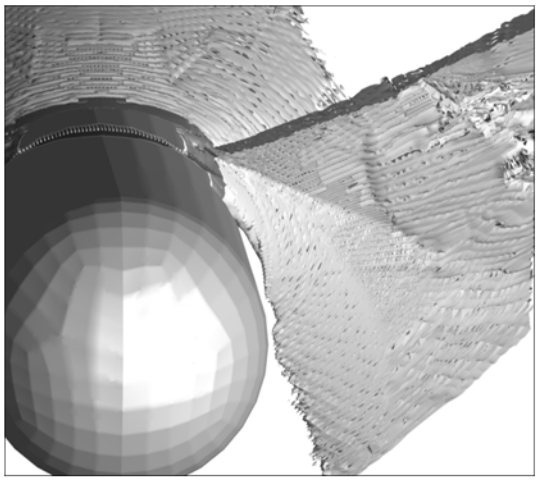


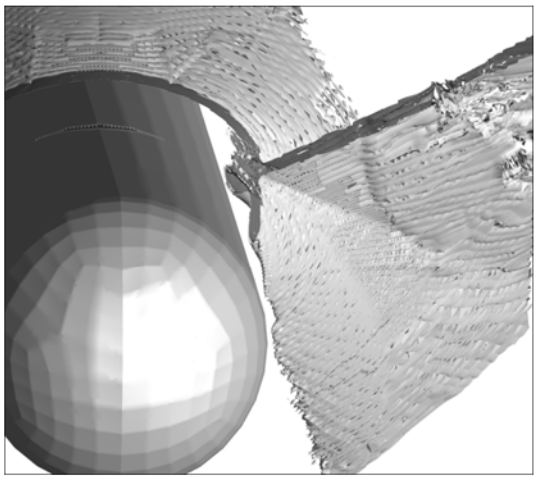
Figure 6.47: Viscous simulation - density gradient contour lines



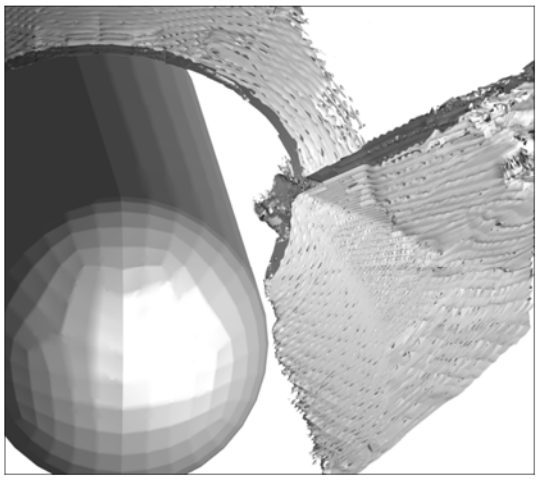
a) 25mm



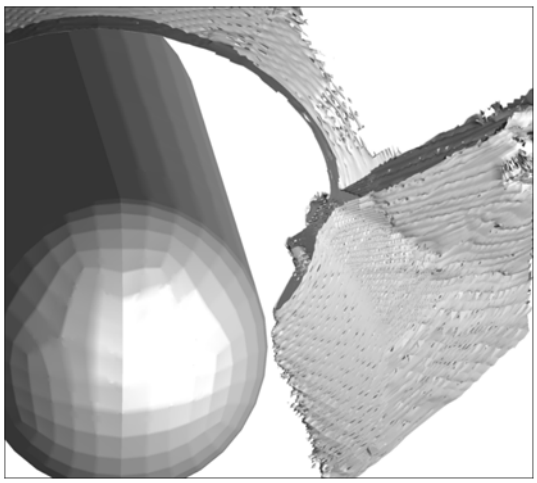
b) 28mm



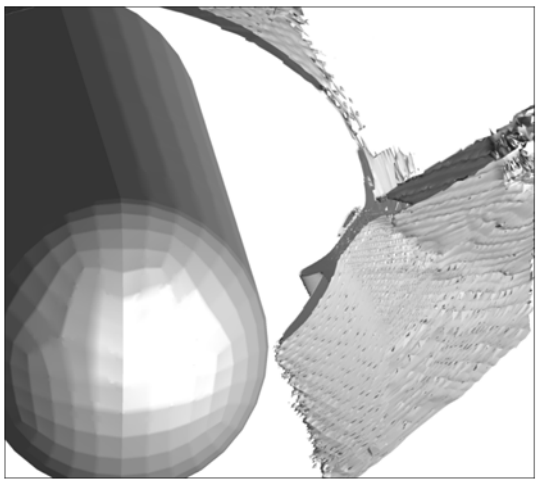
c) 30mm



d) 32mm



e) 34mm



f) 36mm

Figure 6.48: Viscous Simulation - sectioned density gradient iso-surfaces, DG = 10000

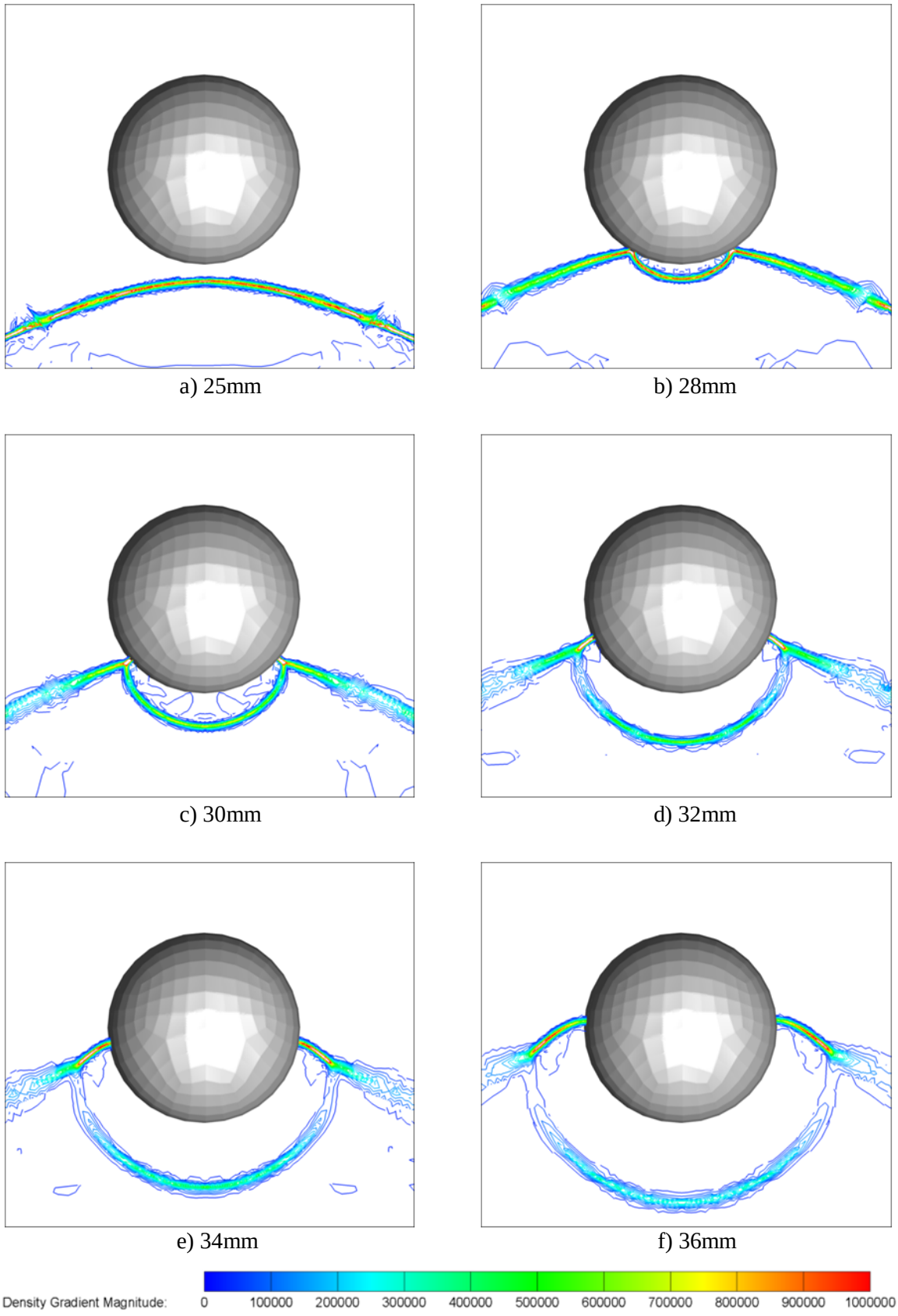
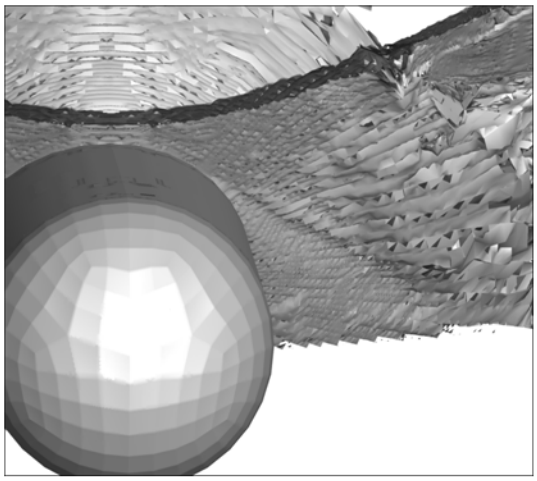
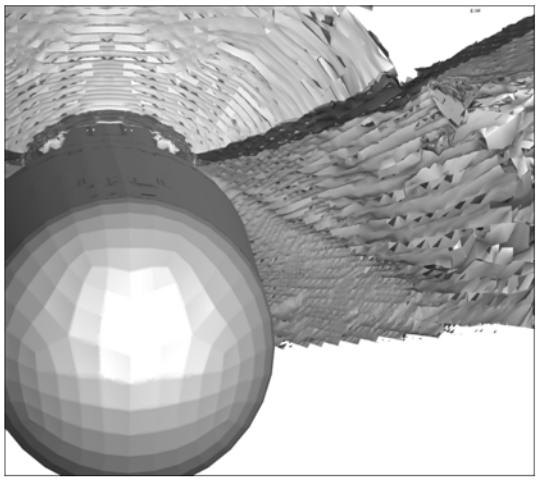


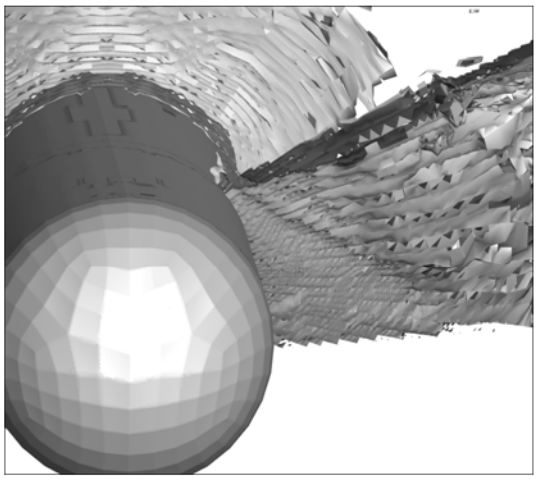
Figure 6.49: Inviscid simulation - density gradient contour lines



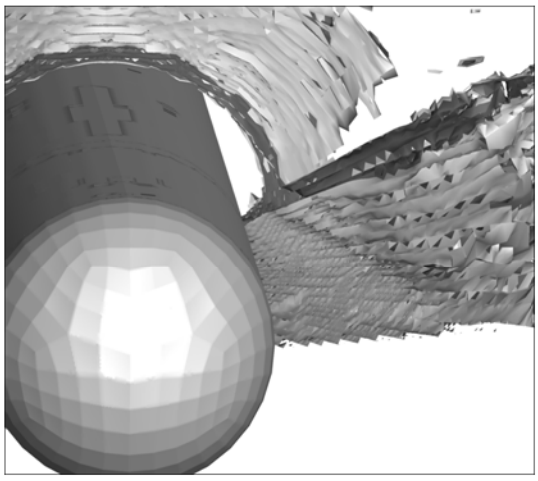
a) 25mm



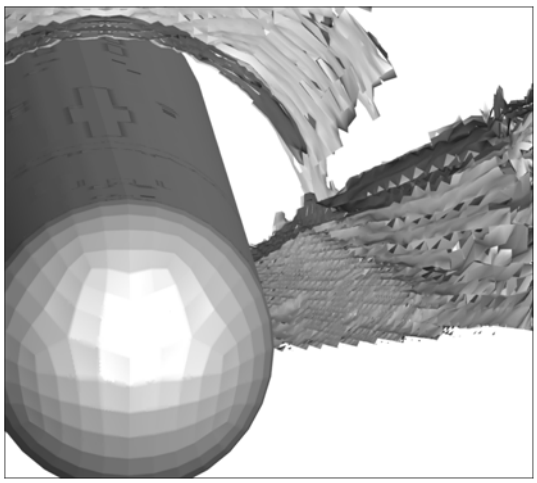
b) 28mm



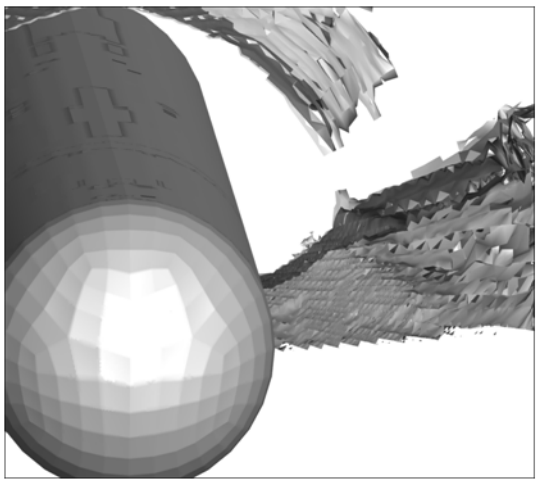
c) 30mm



d) 32mm



e) 34mm



f) 36mm

Figure 6.50: Inviscid Simulation - sectioned density gradient iso-surfaces, DG = 10000

Figure 6.46 shows two sets of identical iso-surfaces, one for the viscous case and one for the inviscid case. Figure 6.47 and Figure 6.49 (a front view of the cylinder with the windward side at the bottom of the frame) show the development of the incident and reflected shock waves by means of density gradient contour plots around the cylinder at specific axial positions denoted in the sub-captions. These contour plots provide a clearer insight into the formation of the shock waves shown in the iso-surfaces in Figure 6.41, Figure 6.42 and Figure 6.46. Sectioned density gradient iso-surfaces are shown in Figure 6.48 and Figure 6.50 (corresponding to Figure 6.47 and Figure 6.49 respectively) and provide a three-dimensional perspective of the structure of the shock waves and are oriented with the windward side of the cylinder in the top of each frame (i.e. are upside down relative to Figure 6.47 and Figure 6.49) thereby displaying the internal structure of the shock wave reflections. Selected frames from the density gradient plots have been rotated, enlarged and annotated in Figure 6.51 and Figure 6.52 for the viscous and inviscid simulations respectively.

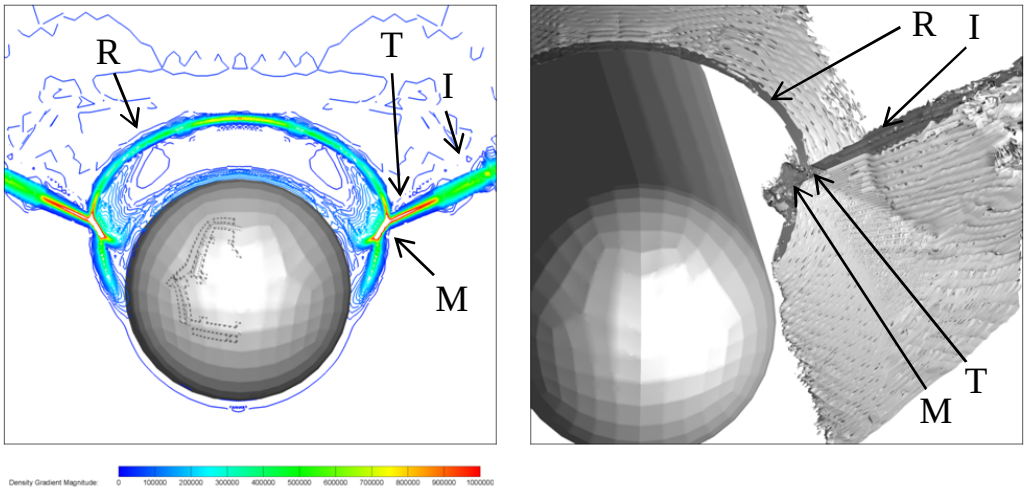


Figure 6.51: Viscous Simulation - Annotated shock reflection structure, 32mm

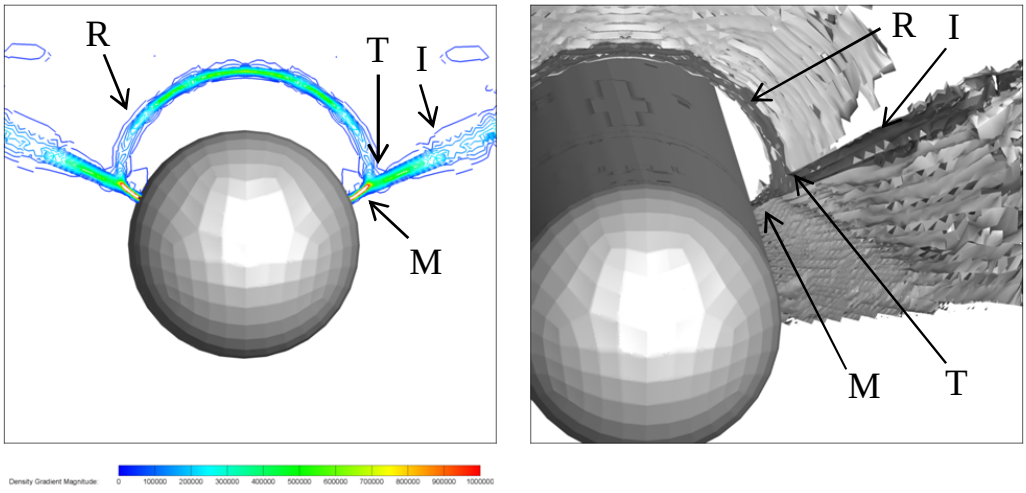
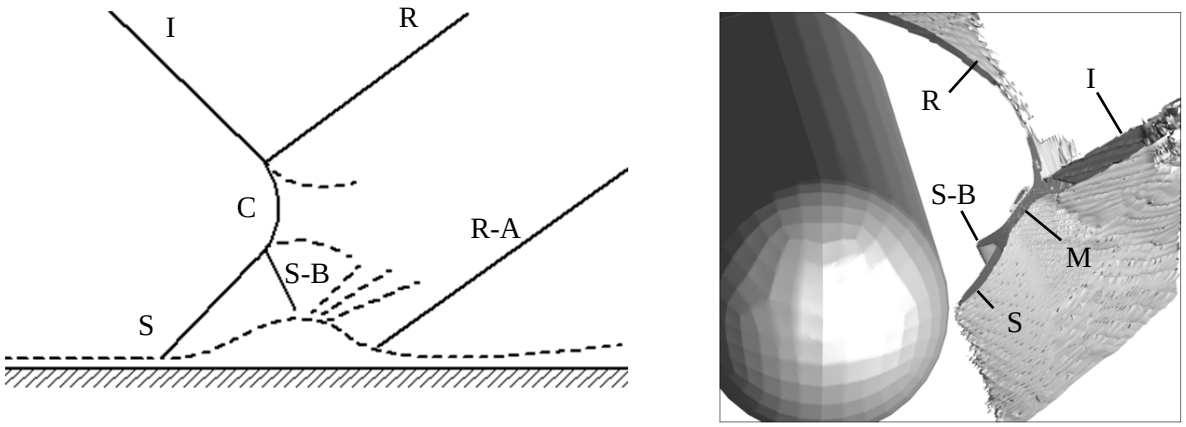


Figure 6.52: Inviscid Simulation – Annotated shock reflection structure, 32mm

The most obvious difference between the two cases is the absence of a boundary layer on the cylinder for the inviscid case. It may seem trivial to analyse the results of a SWBLI without a boundary layer, however the inviscid results can clarify which of the flow features in Figure 6.41 and Figure 6.42 are caused by the incident shock wave wrapping around the cylinder and which are a result of the SWBLI itself. The absence of the boundary layer on the cylinder results in an inability for the pressure behind the shock wave to feed upstream, a mechanism that occurs due to the subsonic portion of the boundary layer. It is for this reason that the incident shock wave affects the flow field around the cylinder further downstream in Figure 6.46b) compared to Figure 6.46a). The nature of the flow along the 180° meridian is also affected by the viscosity of the air. For the viscous case a seam of low energy air runs along the 180° meridian of the cylinder made up of the lee-side boundary layer as well as the air swept in from the windward side of the cylinder as described earlier on. This air is responsible for the ridge that runs along the top of the cylinder in Figure 6.46a), and for the shadow region in the shock wave in Figure 6.46c). For the inviscid case there is no boundary layer and hence the flow along the 180° is simply the result of the amalgamation of the original incident shock wave (Figure 6.46d)).

The shock wave reflection off the cylinder is also affected by the presence of the boundary layer. Regular and Mach reflection is observed for the inviscid simulation as seen in Figure 6.49 and Figure 6.50. Initially the reflection pattern that exists is a simple incident-reflected arrangement (Figure 6.49b)) but as the incident shock wave moves around the cylinder the angle between the incident shock wave and the surface is such that Mach reflection occurs (Figure 6.49c) – f)). All of the salient features of a Mach reflection are evident, namely the incident (I) and reflected (R) shock waves, Mach stem surface (M) and the triple point (T) as highlighted in Figure 6.52. The triple point trajectory is visible as a crease in the iso-surfaces in Figure 6.41 and Figure 6.43 and is initially tangential to the surface of the cylinder. The Mach stem surface is found to curve with increasing axial position (i.e. moving further downstream) so as to meet the surface of the cylinder at a right angle and is visible as the bulge in the shock wave front in Figure 6.46b) and Figure 6.46d). All of these phenomena were noted by Timofeev et al (1997) in a study into the interaction of a moving shock wave with an oblique cylinder as illustrated in Figure 3.10. It is important to note at this stage that the numerical work carried out in said study was performed using an **inviscid** Eulerian gas model due to the high Reynolds numbers of the flow. Timofeev et al (1997) found the shocked flow around the cylinder was highly three-dimensional with Mach and regular reflections taking place simultaneously due to the complex geometries involved. The regular reflection was found to occur during the early stages of the interaction when the incident shock wave made initial contact with the cylinder (on the windward side of the cylinder). Mach reflection was found to take place as the interaction moved around the cylinder towards the leeward side. These results, as mentioned previously, are very similar to those shown in Figure 6.49 albeit at a specific instant in time in an unsteady flow.

For the viscous case the shock wave configuration substantially differs from the inviscid simulation. The nature of the work of Timofeev et al was such that even if viscosity had been included in the simulations, very little (if any) change would have been noted since the boundary layer only appears behind the shock wave. The net result is a simple Mach reflection forming, similar to that on a wedge. In the current SWBLI study all of the elements involved are steady by nature allowing the boundary layer to fully develop over the course of a wind tunnel test. Figure 6.47 shows that the typical Mach reflection configuration found in the inviscid simulation (shown in Figure 6.49) does not occur when the viscous effects are accounted for. Instead of a three shock structure forming as for the inviscid case, a fourth shock wave is now present. The density gradient iso-surfaces of Figure 6.48 provide a useful insight into the nature of this fourth shock wave. Figure 6.48a) shows the incident wave impinging on the windward surface of the cylinder. Figure 6.48b) and Figure 6.48c) show the regular reflection of the incident wave off the surface of the boundary layer while in Figure 6.48d) a Mach stem is beginning to form. The Mach stem then interacts with the SWBLI as shown in Figure 6.47d) – f). This interaction creates the reflected wave off the surface of the separated region and is particularly evident as the small shock waves at the bottom of the Mach stem in Figure 6.48e) and Figure 6.48f). This configuration closely resembles the gas dynamic structure of that noted by Panov (1968), as compared in Figure 6.53 below:



a) Panov (1968) b) Current study

Figure 6.53: Comparison of SWBLI shock structure

Figure 6.53 shows the shock wave structure resulting from a SWBLI consisting of an incident (I), reflected (R), separation (S), separation bubble (S-B) and re-attachment (R-A) shock wave. Panov noted that in certain instances a central (C) shock wave would develop, akin to the Mach stem (M) in Figure 6.53b). This central shock wave was found to form when i) the spacing between the shock wave and the boundary layer generators was less than some definite value, or ii) when the intensity of the incident shock wave was suitably high. Given the strength and intensity of the bow shock that

forms off the hemispherical profile it is likely that the latter holds true for the current study. The central shock wave in Figure 6.53a) has a curved profile, whereas the comparable feature, labelled as the Mach stem surface, noted in the current study is planar in form as can be seen in Figure 6.47 and Figure 6.48. The position of both shock waves (C and M in Figure 6.53a) and b) respectively) as well as the conditions behind their formation suggests that they are ultimately the same flow feature just labelled differently.

One important aspect of Figure 6.47 and Figure 6.48 is the trajectory of the two separation shock waves. These shock waves propagate down and around the cylinder in a similar manner to the separation lines noted in the oil-flow surface patterns for the hemisphere. They also fit the iso-surface in Figure 6.41 indicating that while the surface flow contour plots generated by the initial CFD simulation did not show the two separation shock waves, they are present in the flowfield nonetheless.

A combination of Mach number (yellow) and density gradient (green) iso-surfaces are presented in Figure 6.54 and Figure 6.55 which provide an insight into the structure and development of the aforementioned induced shock wave respectively. The viewing plane of Figure 6.54 and Figure 6.55 is taken normal to the cross-section through the shock waves in Figure 6.48 and Figure 6.50. The density gradient iso-surface in Figure 6.54 has been sectioned along the vertical plane of symmetry of the flowfield (as shown in Figure 4.16) for the sake of clarity. The mosaic of images in Figure 6.55 show the density gradient iso-surface sectioned at various axial positions, the exact locations of which (measured relative to the leading edge) are given in the sub captions. The Mach number iso-surface represents the separated flow on the surface of the cylinder caused by the SWBLI.

The density gradient and Mach number iso-surfaces in Figure 6.54 are merely a more complex, three-dimensional version of the basic anatomy of the SWBLI shown schematically in Figure 3.11, similar to that of Figure 6.53. The incident shock wave impinges on the boundary layer, separates the flow causing an induced separation and a re-attachment shock wave to form. The separation shock wave intersects the shock wave reflecting off the upper boundary of the separation bubble. The high pressure behind the separation bubble shock wave propagates through the boundary layer and causes the flow to separate upstream of the shock impingement point creating the induced separation shock labelled as the such in Figure 6.54.

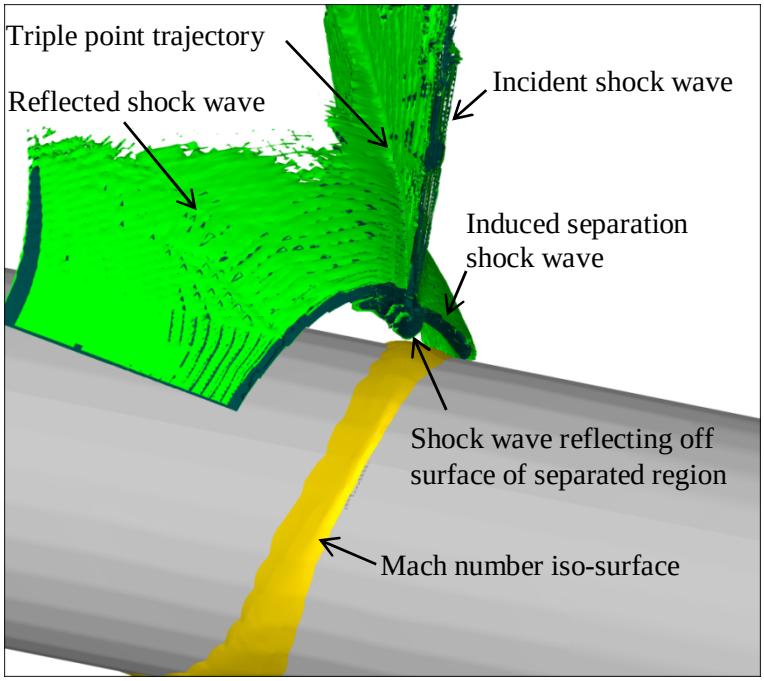
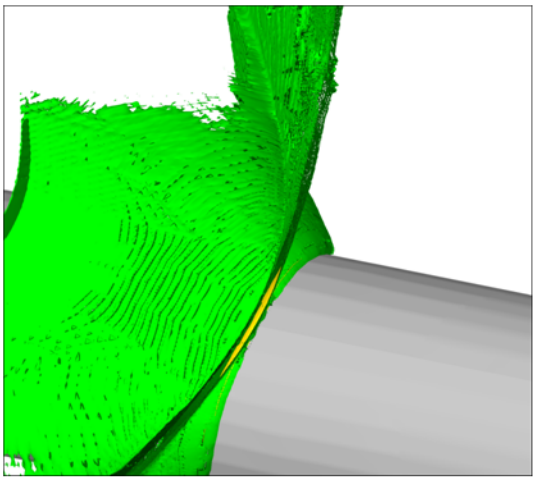
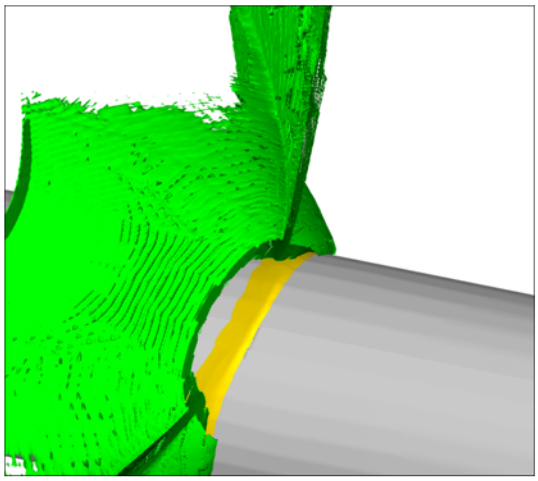


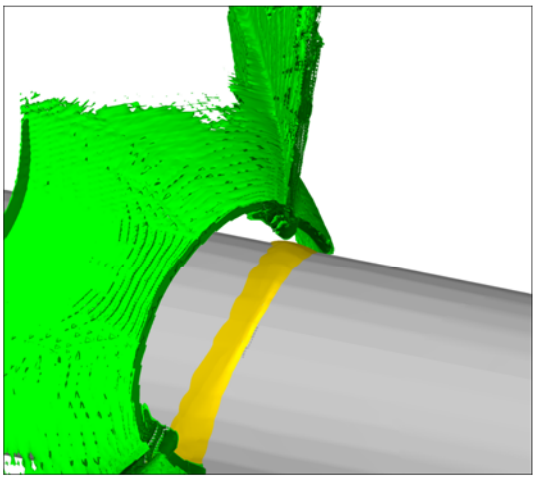
Figure 6.54: Viscous Simulation – annotated Mach number and density gradient iso-surfaces, Hemisphere, 30mm



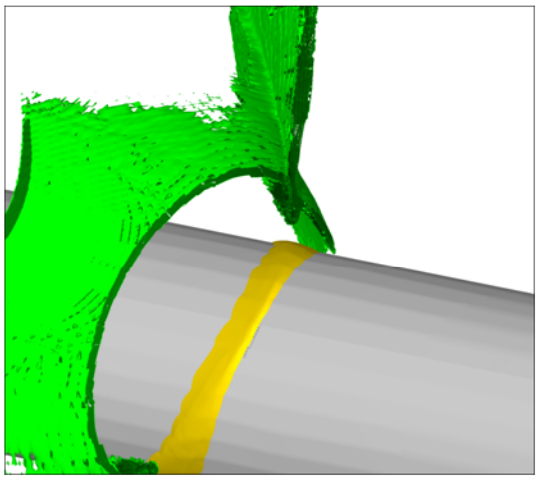
a) 25mm



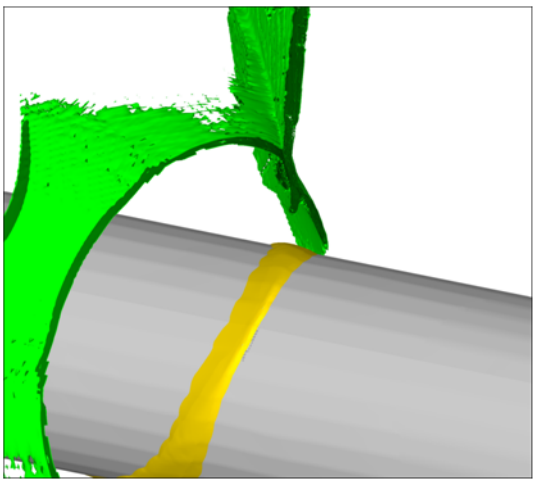
b) 28mm



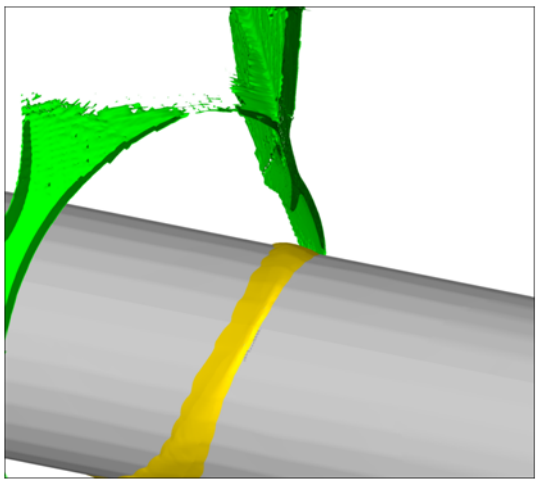
c) 30mm



d) 32mm



e) 34mm



f) 36mm

Figure 6.55: Viscous simulation - Mach number (M = 0.9) and sectioned density gradient (DG = 10000) iso-surfaces, Hemisphere

Figure 6.56 shows the surface pressure distribution along the 180° meridian of the cylindrical section of the hemispherical SWBLI (as per Figure 6.36) for a viscous and an inviscid case. The most notable difference between the two curves is the axial position of the main pressure rise. For the inviscid simulation the pressure rise occurs approximately 52mm downstream from the hemisphere-cylinder intersection. When viscosity is accounted for this pressure rise is found to occur approximately 42mm downstream from the hemisphere-cylinder intersection. This 10mm shift in pressure rise is a direct result of the upstream influence that is commonplace in SWBLI (Anderson, 2007). Another difference between the two curves is the maximum pressure ratio value that is reached. For the inviscid case the maximum value is approximately 1.17, while for the viscous solution the maximum pressure ratio lowers to 1.13. The shearing of the layers within the fluid for the viscous case will provide resistance to the effects of the pressure rise, hence reducing the magnitude of the pressure ratio compared to the inviscid case. The axial distance over which the pressure rise takes place is also larger for the viscous solution. This reduced pressure gradient represents a dampening of the interaction for the viscous case. The most likely cause of this dampening is the shock wave reforming away from the surface of the cylinder on the lee-side due to the compression waves forming off the thickened boundary layer. In the inviscid simulation the boundary layer is absent and the shock wave simply reforms on the lee-side surface of the cylinder.

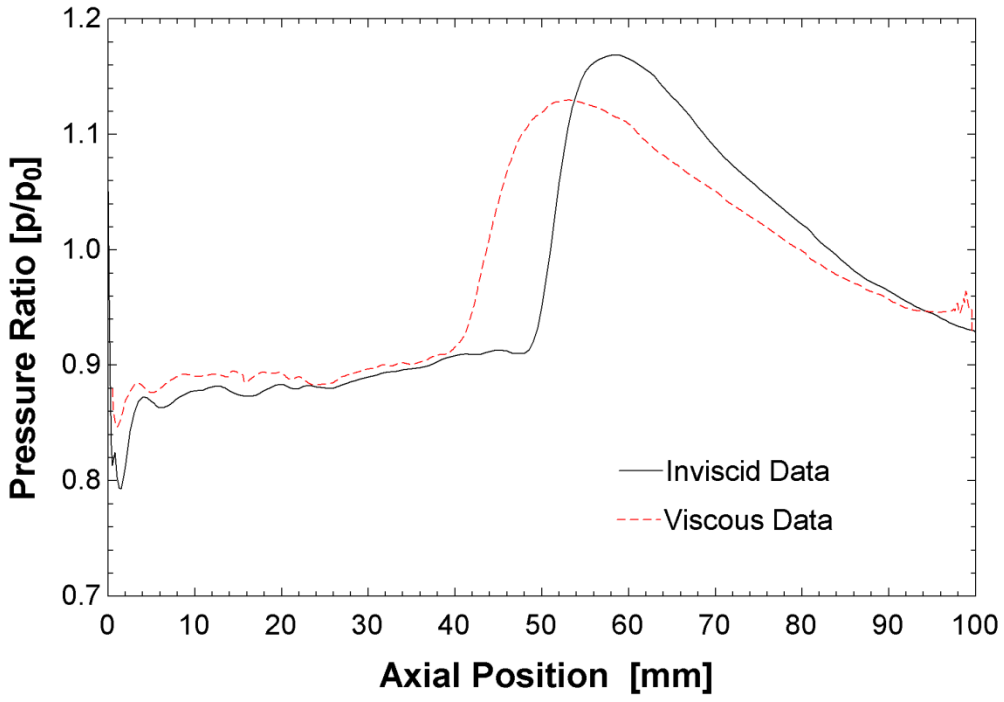


Figure 6.56: Lee-side (180° meridian) pressure distribution, Hemisphere

Returning to the un-finished analysis of the pressure distribution curves in section 6.2.4, it is now possible to explain both the double bump noted along the 60° meridian (refer back to Figure 6.39) as well as the separation and re-attachment curves of Figure 6.35 and Figure 6.37. Starting with the double bump; the 60° meridian coincides with the location of the first clearly formed Mach stem (see Figure 6.47c)). The Mach stem, being a shock wave, causes a rapid rise in surface pressure which is evident in the pressure distribution curves as the double bump. This result also holds true for the conical SWBLI generator as a Mach stem is evident in Figure 6.42b) meaning a Mach stem must exist. The double bump is not as evident as the meridian angle increases (90°, 120°...) due to the Mach stem not impinging as prevalently on the surface of the cylinder as for the 60° case. The most likely cause of this is insufficient mesh resolution as the maximum refinement level had already been reached in the region in question.

The separation and re-attachment curves are also affected by the differing types of shock wave reflection. Both of the re-attachment curves in Figure 6.35 and Figure 6.37 have a more pronounced curvature past the 60° meridian compared to the locus of the separation points. The flattening out of the separation curve can be accounted for when the four shock structure shown in Figure 6.54 is considered. The upstream leg of the lambda shaped shock structure (labelled as the secondary induced separated shock wave in Figure 6.54) causes the boundary layer to separate upstream of the incident shock wave impingement point. As the interaction moves around the circumference of the cylinder this affect becomes more pronounced (as shown in Figure 6.55) and hence the separated region grows in size as per Figure 6.35 and Figure 6.37.

The effects of the lee-side behaviour is plain to see, the SWBLI has fundamentally altered the entire boundary layer and hence the aerodynamic profile of a cylinder from an axisymmetric profile to a profile with only a single plane of symmetry. The practical consequences of this alteration could include a change (increase) in the drag co-efficient of the body as well as a change in the aerodynamic loading on the body itself – both of which are known consequences of a SWBLI (Delery, 2001). The changes in the aerodynamic profile of the body may lead to reduced or impaired performance of the body when compared to the exact same configuration in an inviscid case. Consider the case of a supersonic missile which fairly well approximates a cylinder with a conical or spherical nose. During carriage onboard an aircraft travelling at supersonic velocities, shock waves emanating from the aircraft itself may well intersect with the missile itself setting up a situation very similar to that presented in this study. The non-axisymmetric profile of the missile resulting from the SWBLI could potentially lead to loading or buffeting issues on the storage pylon which may ultimately damage the aircraft or missile itself. The behaviour of the missile must also be considered upon release from the aircraft. In the situation presented in Figure 6.41, it would be expected that a pitching moment would be induced on the body as a result of the increased thickness of the boundary layer on the leeside.

Should the pitching moment be strong enough, the missile could potentially collide with the aircraft from which it has just been released. It may be worthwhile to note at this stage that all of the work undertaken in this study is done at a zero degree angle of attack to the oncoming free stream. The distortion in the drag profile of the body may well change as the profile increase its inclination to the free stream flow.

Another application that is relevant to the current study is that of the engine intakes of supersonic aircraft. While flying at supersonic speeds, a SWBLI similar to the case presented here may develop in the engine intake. Such an occurrence would affect the operating efficiency of the engine by means of altering the temperatures and pressures of the air within the intake itself (Anderson, 2007).

6.2.6 High Resolution CFD – Hemisphere

The pair of separation lines generated by the hemispherical SWBLI generator are clearly visible in the wind tunnel data, yet were not evident in the initial CFD simulations undertaken. Therefore it was decided to carry out a high resolution CFD simulation on the hemispherical SWBLI generator, the details of which were presented in section 4.2.

Figure 6.57 through Figure 6.62 represent a series of processed images from the high resolution CFD simulations including Mach number contour plots, pressure contour plots and streamlines.

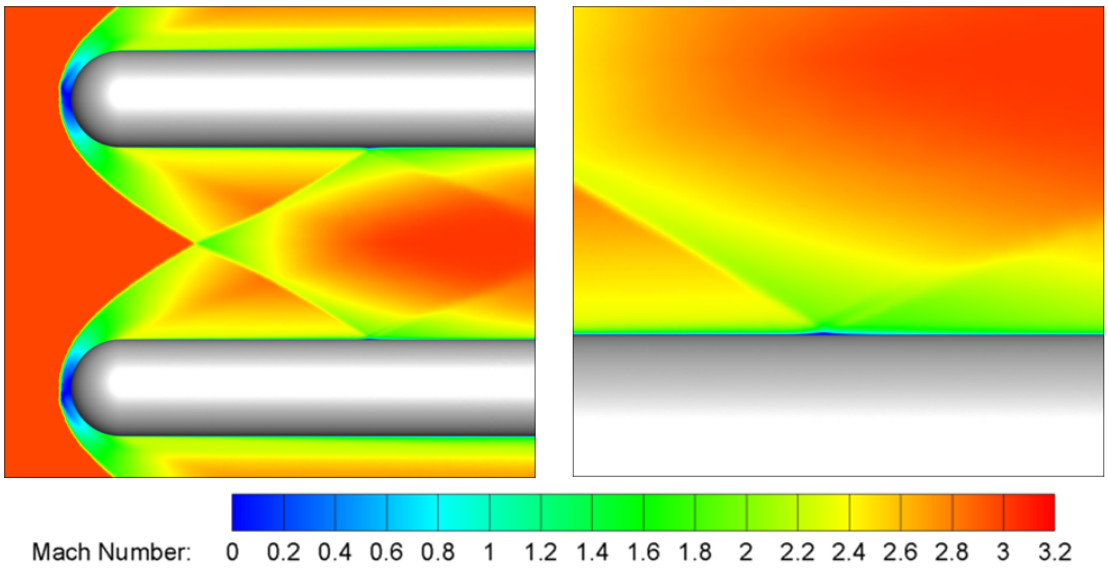


Figure 6.57: High resolution CFD SWBLI overview, Hemisphere

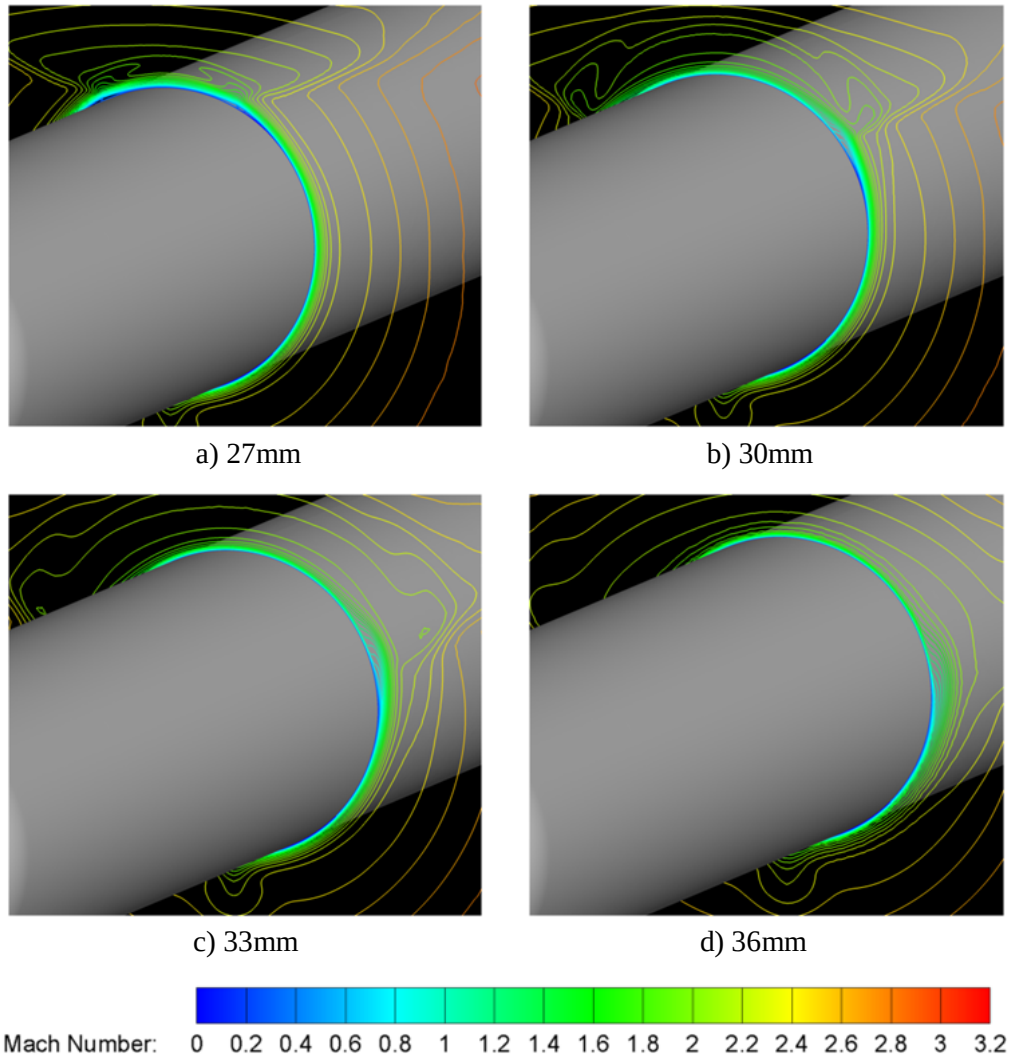


Figure 6.58: High resolution CFD Mach number contour line plots transverse to the axis of the cylinder, Hemisphere

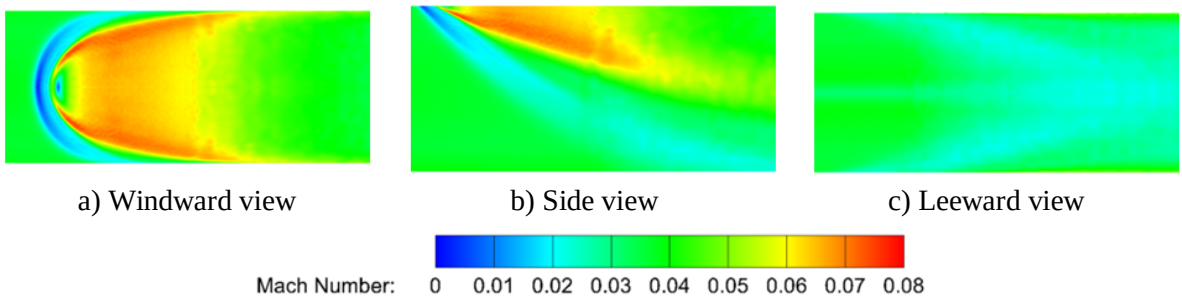


Figure 6.59: High resolution CFD surface flow patterns, Mach number contours, Hemisphere

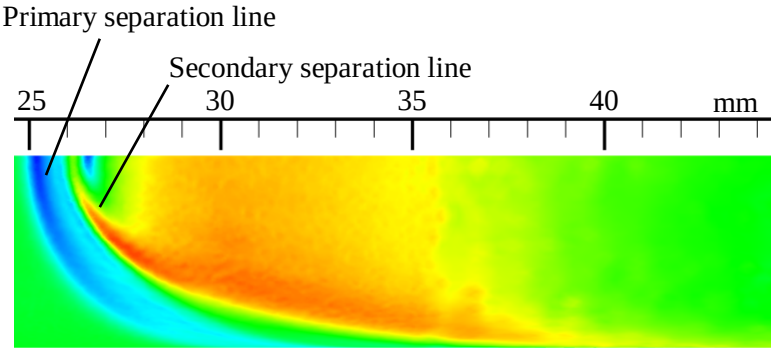
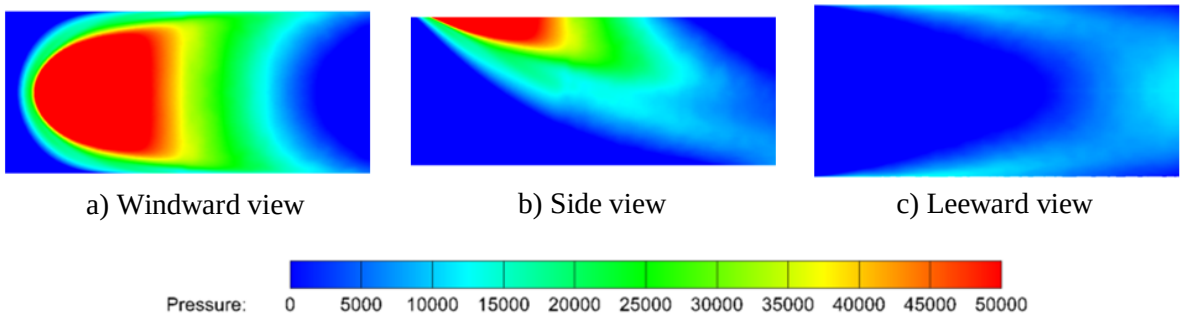


Figure 6.60: High resolution CFD annotated surface flow patterns, Mach number contours with measurement scale, Hemisphere



a) Windward view b) Side view c) Leeward view

Figure 6.61: High resolution CFD surface flow patterns, Pressure (Pa) contours, Hemisphere

The images presented in Figure 6.57 through Figure 6.61 mirror those of the regular CFD simulation presented previously showing all of the salient features of a SWBLI generated by the hemispherical nose profile. The two separation lines are inferred by the surface Mach number contour plots of Figure 6.59 and Figure 6.60, as well as the pressure contour plot of Figure 6.61. The upstream influence of the SWBLI is also visible in the aforementioned contour plots.

Having performed the higher resolution simulation it was decided to analyse some of the more interesting features identified for the hemispherical SWBLI generator previously. Figure 6.62 in particular shows the complex nature of the flow within the SWBLI itself by means of streamlines within the separation bubble. The vertical structure that is evident in the separation bubble is, as explained in section 6.2.3, a combination of the axial adverse pressure gradient and the circumferential pressure gradient (cross-flows) arising out of the SWBLI. What is more apparent in Figure 6.62 (compared to the lower resolution CFD case of Figure 6.28) is how the flow away from the surface of the cylinder does not re-circulate within the separation bubble itself and instead travels down the windward surface of the cylinder.

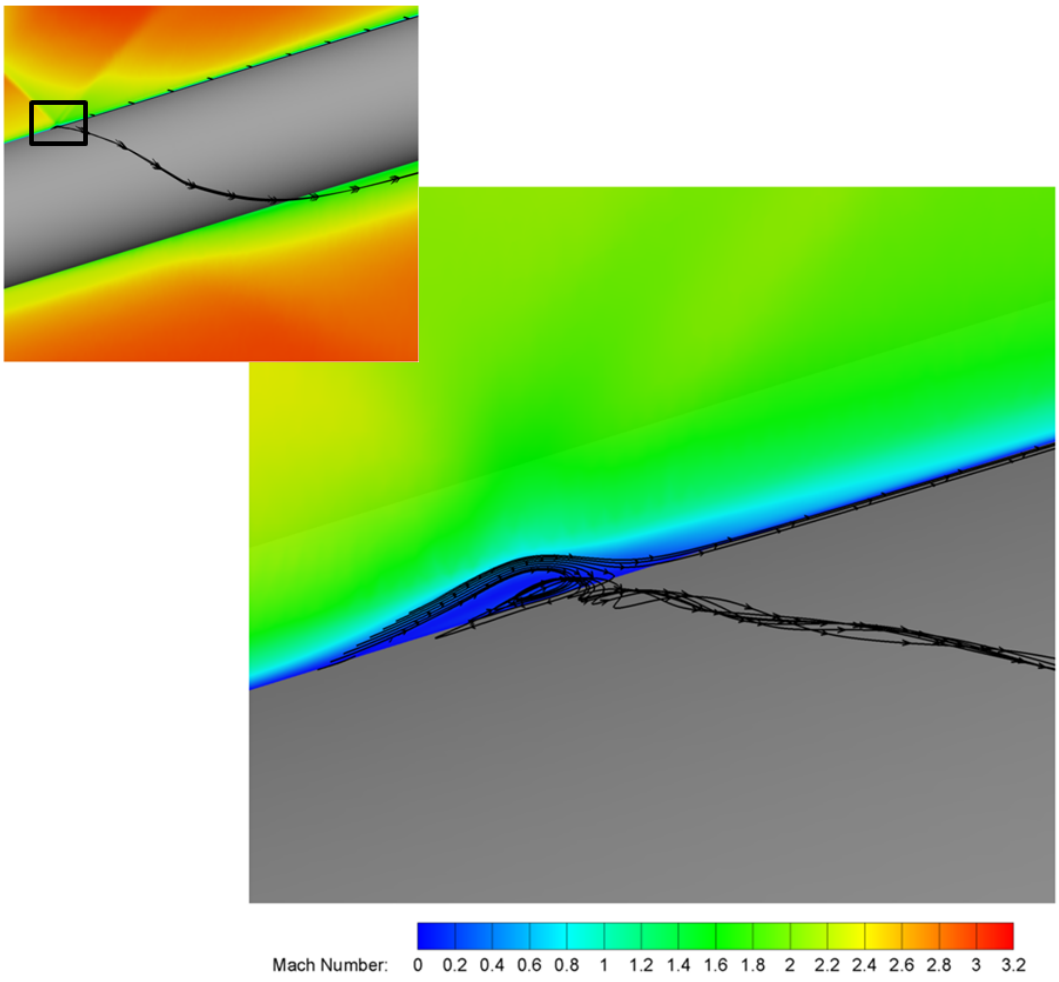


Figure 6.62: High resolution CFD streamlines within separated region, Hemisphere

With the presence of the two separation lines detected in the modified CFD simulations, attention was turned to the flow in the core of the boundary layer in the vicinity of the SWBLI. Line probes were placed at various heights above the surface of the cylinder upstream of the shock wave impingement point along the windward surface, 45° and 90° meridians. The data collected from the line probes is presented in Figure 6.63 through Figure 6.66 below.

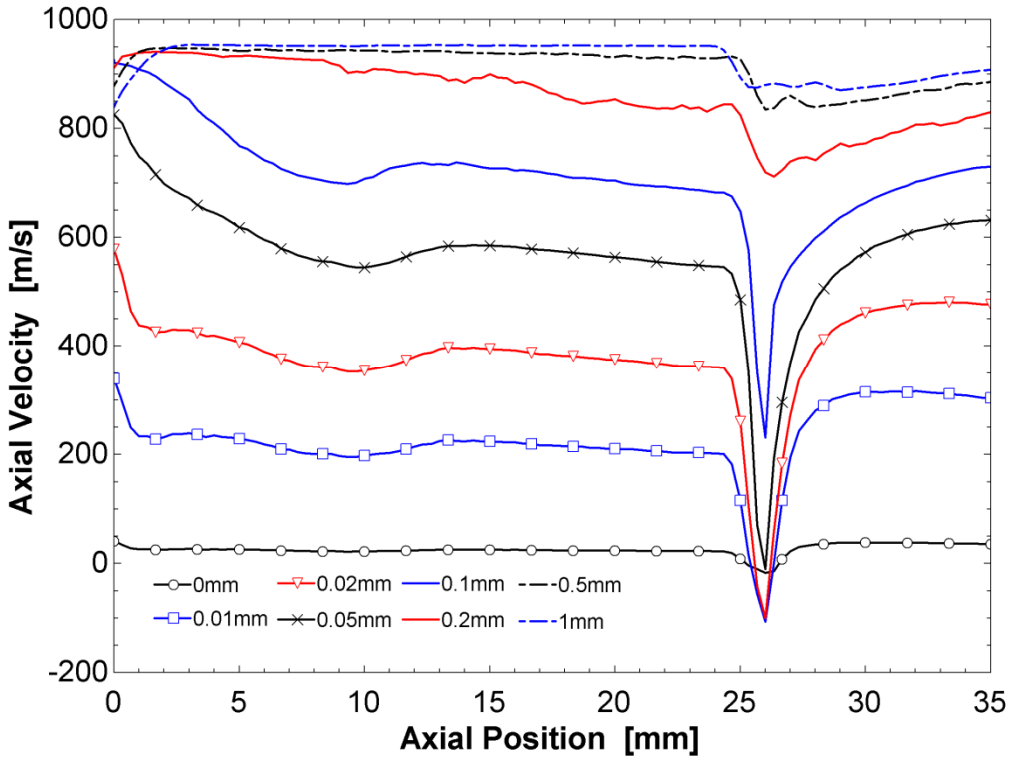


Figure 6.63: Axial velocity variation within the boundary layer, 0° meridian, Hemisphere

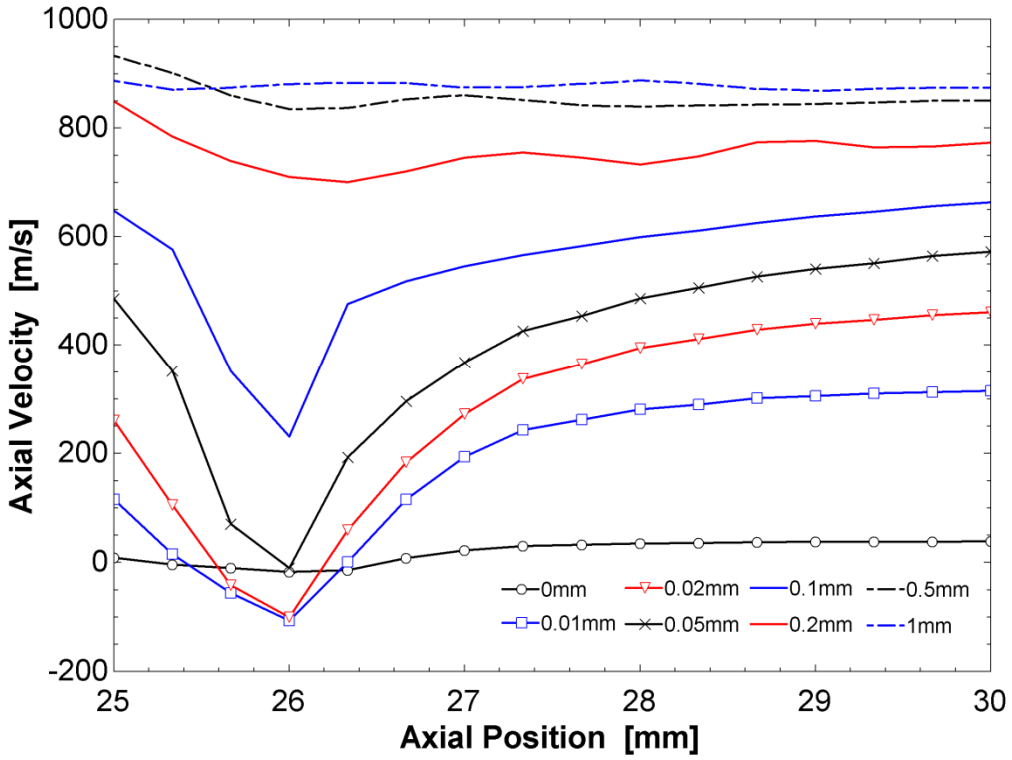


Figure 6.64: Axial velocity variation within the boundary layer in the immediate vicinity of the SWBLI, 0° meridian, Hemisphere

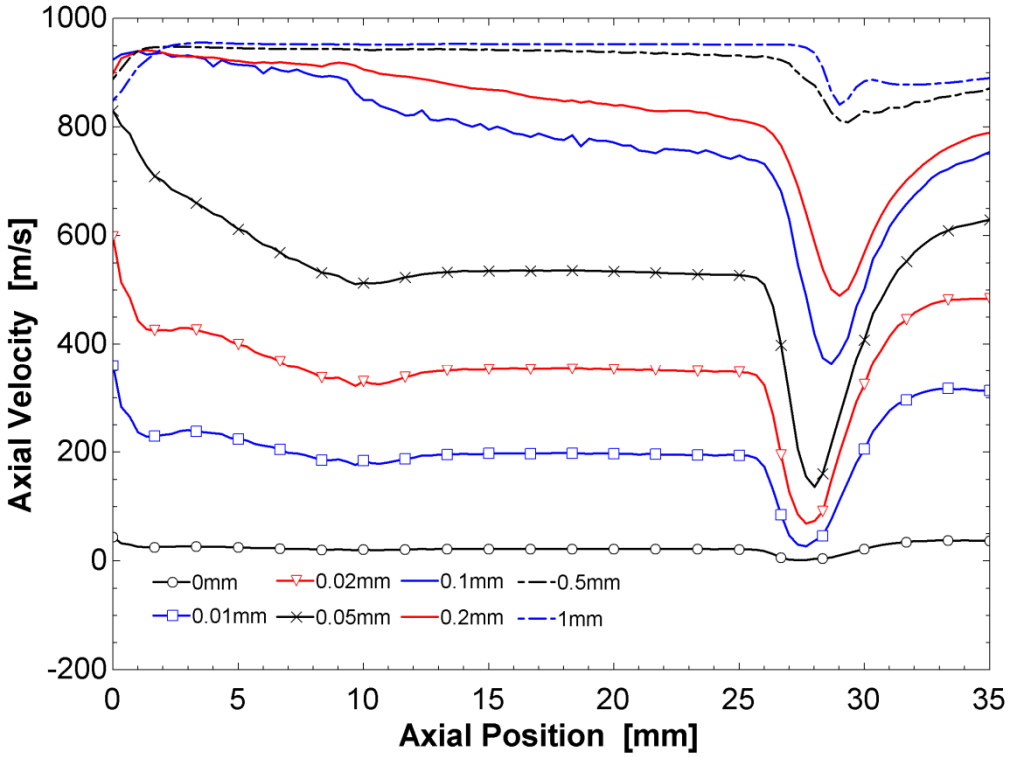


Figure 6.65: Axial velocity variation within the boundary layer, 45° meridian, Hemisphere

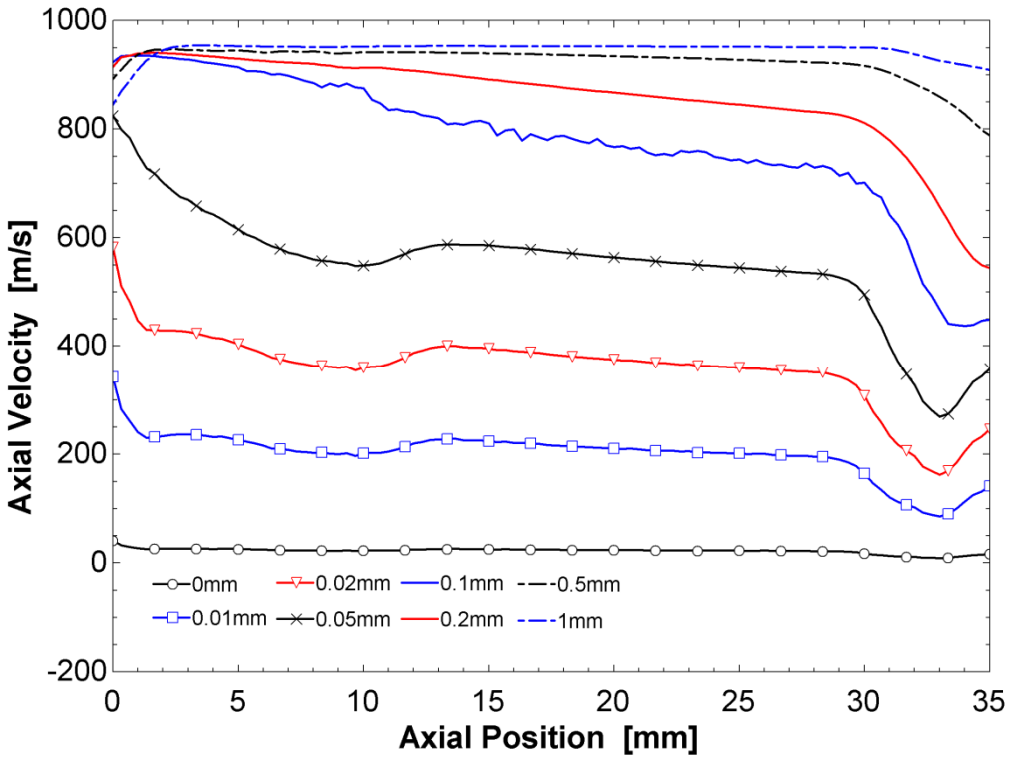


Figure 6.66: Axial velocity variation within the boundary layer, 90° meridian, Hemisphere

The axial velocity plots presented above show the characteristic decrease in velocity through the boundary layer from the free stream value at the outer edge to zero at the wall. In the vicinity of the SWBLI (approximate axial positions of 26mm, 28mm and 32mm for the 0°, 45° and 90° meridians respectively) a sharp decrease in velocity is evident. All of the probes located along the wall (i.e. 0mm above the surface of the cylinder) show only a minor change in axial velocity. This small velocity exists because the layer in contact with the wall should be at zero velocity relative to the wall itself due to the no-slip condition. Moving away from the surface to the probe located 0.01mm above the wall a larger decrease in velocity is noted. This decrease in velocity is magnified as the location of the probes moves further away from the surface until the outer deck is approached (the 0.5mm and 1mm probes). The 0.01mm and 0.02mm probes located on the windward surface (Figure 6.63) also show signs of flow reversal between the 26mm and 27mm axial positions. Due to the viscous effects that dominate the inner deck of the boundary layer flow, the rapid decrease in velocity is caused by the shearing of the layers within the fluid. Returning to the structure of the flow within the boundary layer shown in Figure 3.9, the inner deck is defined as the viscous layer in contact with the wall that is required to decelerate the non-viscous flow to the velocity of the no-slip wall. Further away from the wall in the middle deck the flow can be considered inviscid but rotational when examined over a streamwise distance of several boundary layer heights. The decrease in velocity in this region is more abrupt due to the inviscid nature of the fluid. The shearing between the layers of the fluid will create friction and drag and render the flow less responsive to any rapid change in velocity brought about by a change in pressure gradient. Moving away from the surface further still, the outer-most layer of the boundary layer is reached – the inviscid, irrotational upper deck. The probes that are 0.5mm and 1mm above the surface of the cylinder show signs of being located within this layer due to their initial free stream velocities which are approximately equal to that of the free stream behind the bow shock generated by the hemispherical nose profile.

For the probes along the 45° meridian the gradient of the change in velocity is smaller than the gradient of the velocity of the 0° meridian. For the 90° meridian this gradient is smaller still. The reason behind this decrease in intensity is the reduction in the strength of the incident shock wave as it moves around the circumference of the cylinder (as explained in the previous sections).

On the windward surface of the cylinder the incident shock wave impingement point is located 26mm (see Figure 6.60 and Figure 6.64) from the start of the cylindrical section with the separation occurring 1mm upstream of that (25mm). The upstream influence of the SWBLI is evident in the axial velocity plots where the decrease in velocity is evident 2mm upstream of the shock wave impingement point, along the 0° meridian. Along the 45° and 90° meridians the upstream influence is also evident albeit at differing axial positions due to the geometry of the SWBLI.

Evidence from the wind tunnel test data (Figure 6.31) shows the oil mixture collecting at a stagnation point caused by the stagnation of the mixture resulting from the separation of the boundary layer. This is illustrated schematically in Figure 6.67 and Figure 6.68 and indirectly by the vortex streamlines of Figure 6.62.

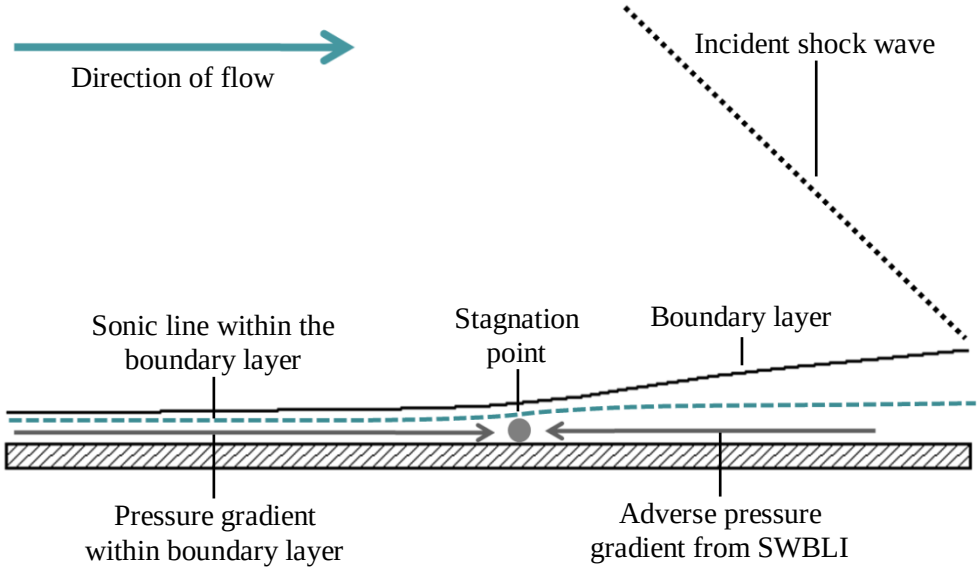


Figure 6.67: Stagnation point caused by upstream influence

The streamlines in Figure 6.62 show both an upstream and a downstream flow within the separation bubble at various points along their trajectories. This change in direction of the flow must involve a stagnation point (zero velocity) such as the one shown in Figure 6.67. The magnitude and direction of the pressure gradient(s) acting within the boundary layer will correspond to the velocity of the flow within the boundary layer. From the literature it is well known that even though the free stream velocity may be supersonic, there exists a subsonic region of flow within the boundary layer itself allowing the higher pressure behind the incident shock to propagate upstream through the boundary layer (Anderson, 2007). The upstream propagation is a direct result of the adverse pressure gradient shown in Figure 6.67.

Figure 6.68 is a not-to-scale superposition of Figure 6.62 and Figure 6.67 to highlight the relationship between the flow within the separated region and stagnation points within the boundary layer. As can be seen from the streamlines only the flow within the low Mach number region (separated region) re-circulates, while the flow in the transonic and supersonic region of the boundary layer passes over the separation bubble and moves down the length of the cylinder. The change in direction of the streamlines within the separated region must be facilitated by a stagnation point. The change in direction from positive axial velocity to negative axial velocity can only occur once zero has been crossed. This result is evident in the axial velocity plots of Figure 6.63 and Figure 6.64 where the

abscissa (corresponding to zero axial velocity) is intercepted twice by the 0mm through to the 0.05mm probes.

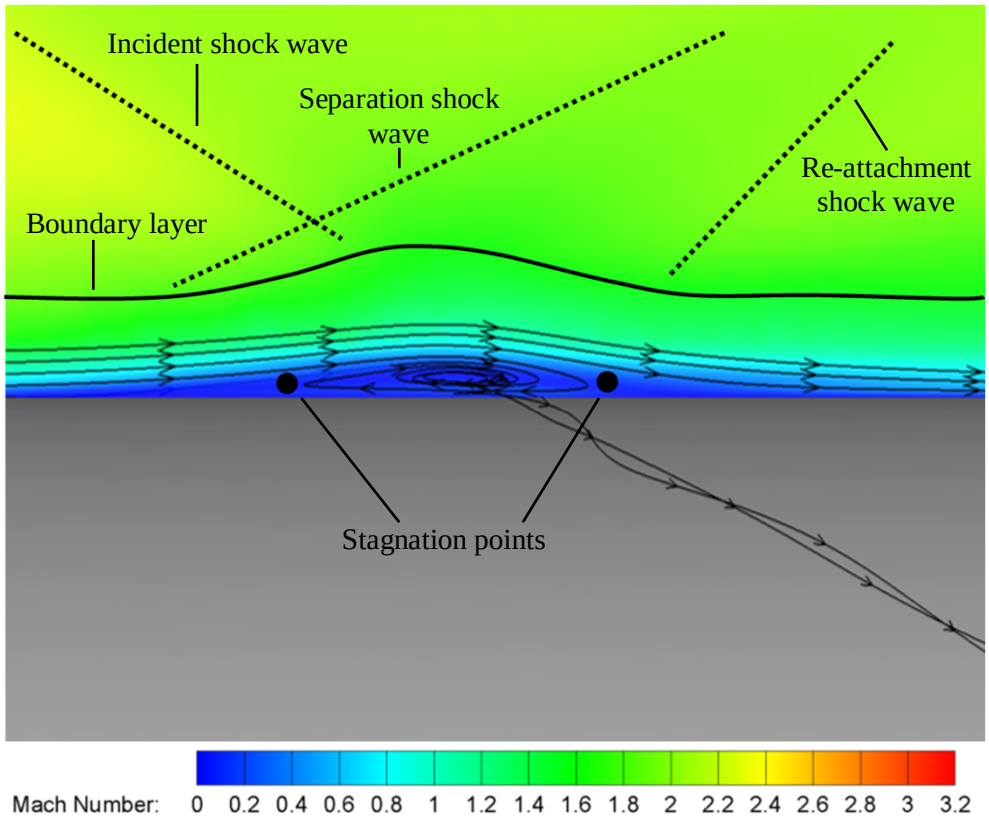


Figure 6.68: Superposition of the stagnation points and the flow within the separated region

The production of vorticity within the boundary layer is also responsible for the location of the spiral-like flow within the separation bubble. As noted in the triple deck structure of the boundary layer (Delery and Dussauge, 2009) the middle deck is a rotational layer and therefore able to produce vorticity, whereas the innermost layer is a viscous dominated region and the outer most layer is an irrotational layer. This is another reason for the re-circulation in the separation bubble only occurring in the lower Mach number region of the flow.

7 Conclusions

The interaction between a curved shock wave and cylindrical boundary layer has been investigated. The curved nature of the incident shock wave and boundary layer represents the most general case of an SWBLI. Three different nose profiles mounted to the leading edge of a cylindrical body were used to generate the incident shock waves; an ogival profile providing the weakest SWBLI, a hemispherical profile providing the strongest SWBLI and a conical profile as an intermediary case. An experimental and numerical investigation was carried out on the three SWBLI generators. All of the numerical and experimental work was undertaken at a free stream Mach number of 3.0 with the axes of the two SWBLI generators spaced 30mm apart.

For all three of the SWBLI generators the wind tunnel test data closely matched that of the CFD simulations, and was also comparable to the data available in the literature. All of the fundamental features of a shock wave/boundary layer interaction were present and identifiable. A horseshoe shaped interaction which was at its most intense on the windward side of the cylinder was observed. The strength of the interaction was seen to reduce with increasing meridian angle. For the conical and hemispherical cases a separation bubble was observed on the surface of the cylinder which, in conjunction with the interaction, dissipated with increasing radial position before disappearing entirely at approximately the 135° meridian ray. This result has been noted in other works involving comparable geometries. The hemispherical SWBLI generator produced two separation lines, a result that was not explicitly evident in the surface flow data from the corresponding CFD simulation. The ogival SWBLI generator created an incident shock wave that lacked the strength to separate the boundary layer. In the absence of a separation bubble a notable region of subsonic flow was observed on the windward side of the cylinder between the meridian angles of 0° and 90°. This subsonic portion of the flow had the same horseshoe shape as that of the separation bubble for the conical and hemispherical cases. In contrast to the ogival case, the hemispherical SWBLI generator created the strongest incident shock wave that produced the most distinct interaction. Due to the strength of the incident and reflected shock waves for the conical and hemispherical cases a Mach stem surface was observed reflecting off the SWBLI. This Mach stem surface was absent for the ogival profile due to the weak nature of the shock waves generated.

Surface pressure plots were also generated and processed to give a more exact location of the separation and re-attachment of the flow. The basic form of these traces was found to match similar curves generated in other studies and further illustrated the development of the SWBLI around the circumference of the cylinder. A clear sweeping of the flow from the windward to the leeward side of

the cylinder was noted for all three profiles tested by means of surface streamlines from both the oil surface flow visualisation and the numerical data.

Selected aspects of the SWBLI generated by the hemisphere profile were focussed on, namely the reflection off the boundary layer and the flow on the leeward side of the cylinder. The reflection of the incident shock wave off the surface of the cylinder was initially of the regular type, transitioning to a modified Mach reflection type 3mm downstream of the incident shock wave impingement point. The Mach stem created an adverse pressure gradient causing the boundary layer to separate upstream of the point of contact between the Mach stem and the boundary layer. The separation shock wave in turn interacted with the Mach reflection, hence the description of the reflection as a modified Mach reflection. The lee-side boundary layer was found to thicken downstream of the SWBLI due to the flow within the boundary layer sweeping around the cylinder from the windward side to the leeward side. This flow is caused by the circumferential pressure gradient that develops within the cylindrical boundary layer. As a result of the boundary layer thickening, the incident shock wave (made up of a series of compression waves caused by the boundary layer thickening) was observed to re-form some distance away from the surface of the cylinder. The thickening of the boundary layer on the lee-side of the cylinder was less prominent in the conical case and negligible in the case of the ogival SWBLI generator.

An inviscid numerical simulation was performed for comparative purposes on the hemispherical SWBLI generator. The shock wave reflection observed in the inviscid case was a simple Mach reflection configuration due to the absence of the boundary layer and its associated flow features (in a SWBLI sense). The deformation of the boundary layer and the detached re-formation of the shock on the lee-side of the cylinder were found not to occur in the absence of viscous forces thus highlighting the effect the boundary layer has on the overall flowfield. The viscous data also emphasised the upstream propagation of the adverse pressure gradient across the incident shock wave through the subsonic portion of the boundary layer. This flow reversal results in the effects of the SWBLI being felt upstream of the point of shock impingement in the classical, inviscid analysis of the problem.

Another numerical simulation was performed (on the hemispherical SWBLI generator) so as to account for the two separation lines that were not evident in the initial numerical simulations performed. This new simulation consisted of a finer mesh immediately upstream of the SWBLI so as to capture the effects of the boundary layer separation. Axial velocity data was collected from various heights within the boundary layer and showed a deceleration, and when very close to the surface, a partial reversal of the flow upstream of the shock wave impingement point. This reduction in the axial velocity is an effect of the mechanism that generates the upstream influence – the adverse pressure

gradient within the boundary layer. The two separation lines were also more prevalent in the higher resolution simulation.

The deformation of the boundary layer is of sufficient magnitude that it could potentially affect the aerodynamic behaviour of the body on which the interaction takes place. The thickening of the lee-side boundary layer would increase the profile drag of the body in question in a non-axisymmetric manner. This could lead to the creation of a pitching moment and adversely affect the performance of the vehicle or body in question.

8 Recommendations

In the event of any future work on this topic, the following recommendations should be taken into account:

- Employ more sophisticated flow visualisation techniques when collecting data from the supersonic wind tunnel. A laser vapour sheet technique (for example) would be able to capture the flowfield transverse to the axis of the SWBLI generators aiding in the conceptualisation of the entire SWBLI.
- Investigate the effect on the SWBLI by orienting the generators at an angle of attack and/or an angle of yaw to the free stream. It may also prove useful to investigate what effect varying the free stream Mach number or distance between the cylinders has on the SWBLI.
- Focus more attention onto the leeward side of the cylinder and the interaction that takes place there.
- Perform a new CFD simulation using the hemispherical SWBLI generator so as to fully predict the behaviour of the two separation shock waves resulting from the interaction.

9 References

Anderson, J D. (1995) *Computational Fluid Dynamics*. McGraw-Hill.

Anderson, J D. (2007) *Fundamentals of Aerodynamics*. pp. 606-609. McGraw-Hill.

Baldwin, B S, and Lomax, H. (1978) Thin Layer Approximation and Algebraic Model for Separated Turbulent flows. *AIAA*, no. 78-257.

Ben-dor, G, Igra O, and Elperin, T. (2001) Chap. 8.1 in *Handbook of Shock Waves Volume 2 - Shock Wave Interactions and Propogation*, Academic Press.

Brosh, A, Kussoy, M I, Hung, C M. (1985) Experimental and Numerical Investigation of a Shock Wave Impingement on a Cylinder, *AIAA*, no. 6, pp. 840-846.

Delery, J M. (2001) Shock Wave/Boundary Layer Interactions, Chap. 8.3 in *Handbook of Shock Waves Volume 2 - Shock Wave Interactions and Propogation*, by Ben-dor, G, Igra O, and Elperin, T, 205-264.

Delery, J, and Dussauge, J. (2009) Some physical aspects of shock wave/boundary layer interactions. *Shock Waves* (Springer Berlin) 19, no. 6, pp. 453-468.

Dolling, D S. (2001) Fifty Years of Shock-Wave Boundary Layer Interaction Research: What Next? *AIAA Journal* 39, no. 8, pp. 1517-1531.

Dupont, P, Haddad, C, Ardissone, J P and Debieve, J F. (2005). Space and Time Organisation of a Shock Wave/Turbulent Boundary Layer Interaction. *Aerospace Science and Technology* 9, pp. 561-572.

Dussauge, J-P and Piponniau, S. (2008) Shock/Boundary-Layer Interactions: Possible Sources of Unsteadiness." *Journal of Fluids and Structures* 24, pp. 1166-1175.

Gai, S L, and The, S L. (2000) Interaction Between a Conical Shock Wave and a Planar Boundary Layer. *AIAA Journal* 38, no. 5, pp. 804-811.

Irving Brown, Y A. (2002) *Three-Dimensional Shock Wave Reflections.* PhD Thesis, University of the Witwatersrand, Wits University Press.

Kussoy, M I, Brown, J D, Brown, J L, Lockman, W K, and Horstman, C C. (1988) *Fluctuations and massive separation in three-dimensional shock-wave/boundary-layer interactions*. Ames Research Center, NASA.

Kussoy, M I, Viegas, J R, and Horstman, C C. (1980) Investigation of a Three-Dimensional Shock Wave Separated Boundary Layer. *AIAA Journal* 18, no. 12, pp. 1477-1484.

Migotsky, E, and Morkovin, M V. (1951) Three-Dimensional Shock-Wave Reflections. *Journal of the Aeronautical Sceinces* 18, no. 7, pp. 484-504.

Morkovin, M K, Migotsky, E, Bailey, H E, and Phinney, R E. (1952) Experiments on Interaction of Shock Waves and Cylindrical Bodies at Supersonic Speeds. *Journal of the Aeronautical Sciences* 19, no. 4, pp. 237-248.

Morrison, R B. (1962) *Design Data for Aeronautics and Astronautics*. John Wiley and Sons, Inc.

NACA. (1953) *Report 1135 - Equations, tables, and charts for compressible flow.* Ames Research Center, NASA, p. 12-19.

Panov, Y A. (1968) Interaction of Incident Three-Dimensional Shock with a Turbulent Boundary Layer. *Fluid Dynamics* 3, no. 3, pp. 158-161.

Sawchuk, S P, and Zamir, M. (1992) Boundary Layer on a Circular Cylinder in Axial Flow. *International Journal of Heat and Fluid Flow* 13, no. 2, pp. 184-188.

Scott, D M. (1994) *Investigation of the Mach Reflection Phenomenon in Steady Supersonic Flows.* MSC Dissertation, University of the Witwatersrand, Wits University Press.

Settles, G S. (2001) *Schlieren and Shadowgraph Techniques.* Springer-Verlag.

Timofeev, E V, Takayama, K, Voinovich, P A, Sislian, J, and Saito, T. (1997) Numerical and experimental study of a three-dimensional unsteady shock wave interaction with an oblique cylinder. *21st International Symposium on Shock Waves.* Great Keppel Island.

Tutty, O R, Price, W G, and Parsons, A T. (2002) Boundary layer flow on a long thin cylinder. *Physics of Fluids* 14, no. 2, pp. 628-637.

Wilcox, D C. (2004) *Turbulence Modelling for CFD.* 2nd Edition. DCW Industires.

Zucrow, M, and Hoffman, J. (1976) *Gas Dynamics (Vol. 1).* New York: John Wiley and Sons.

Appendix A: Wind Tunnel Overhaul

Previous work carried out by the author using the supersonic wind tunnel (SST) at The University of the Witwatersrand revealed the flow through the test section was heavily turbulent, and as a result the images gathered from the wind tunnel were extremely poor (see Figure A 1). Therefore it was decided that an internal inspection and subsequent dismantling of the tunnel all the way back to the pilot valve was required. This was the first time such an extensive inspection had been carried out on the wind tunnel since its installation and commissioning in the early-1960s.

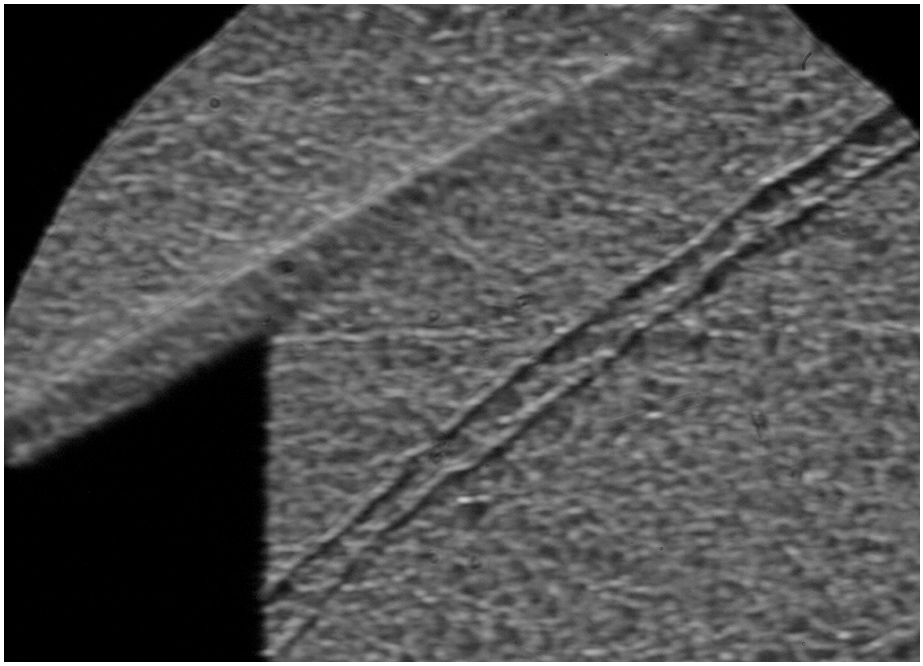


Figure A 1: Sample image of the turbulent flow

A.1 February 2008

Once the wind tunnel had been dismantled it was discovered that two of the three so-called turbulence-reducing screens, located immediately upstream of the settling chamber, had partially broken loose of their brackets. The turbulence-reducing screens are necessary to smooth the flow before it (the flow) enters the contraction of the first throat. All three of the screens, which are made from stainless steel mesh, were then removed from their brackets and replaced with new mesh, specified below:

Table A 1: Mesh specifications for turbulence reducing screens

Material	Mesh	Aperture	Wire Diameter [mm]
Stainless Steel	20	0.82	0.45

While the screens were being replaced, it was decided that the baffle cone, the inside of the expansion cone, the entire settling chamber and the entrance cone joining the settling chamber and the side plates of the tunnel should be re-painted. The baffle cone, settling chamber and entrance cone were sent for external sandblasting, while the expansion cone (which remained in situ) was cleaned using a pneumatically driven rotating wire brush. All of the aforementioned components were then primed internally and externally using a red oxide coating. The baffle cone and entrance cone were then painted using a two-part epoxy sealant, as were the insides of the expansion cone and settling chamber. The latter pair was painter externally with polyvinyl acetate paint. In addition to the components discussed formerly, the inside of the main air reservoir was also scraped down and re-painted where necessary using the same epoxy based sealant.

The gaskets located between the expansion cone and settling chamber and the settling chamber and the flange which joins to the remaining downstream section of the wind tunnel were also replaced.

A.2 May 2008

Upon completion of the re-assembly of the tunnel, the turbulent flow had reduced significantly and a marked improvement in the quality and clarity of the images was noted. In spite of these improvements a decision was made to modify the optics setup so as to further improve the quality of the shadowgraph and schlieren images. The original light source used was a xenon flash lamp, with an exposure time of the order of a few microseconds. This small exposure time highlighted the remaining turbulent flow (as shown in Figure A 2) and thus a decision to switch to continuous light source was made.

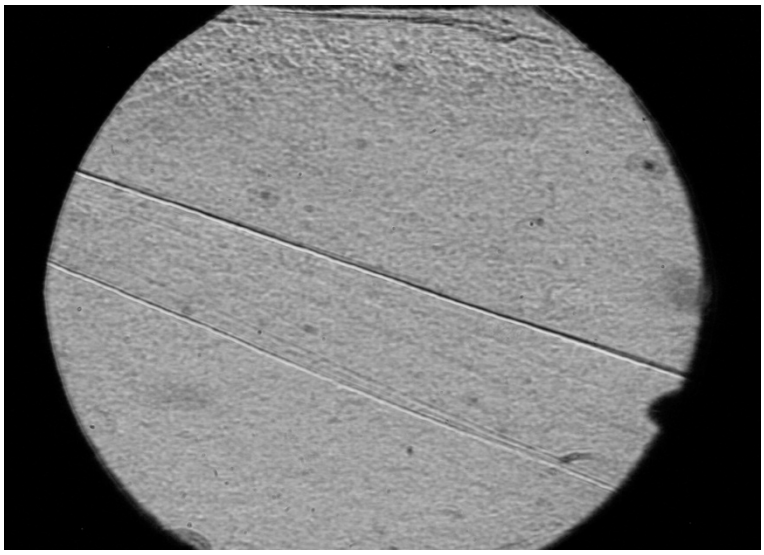


Figure A 2: Sample image (shadowgraph) from xenon flash lamp

The continuous light source comprises of a General Electric 650W Halogen projector bulb that illuminates the test section for the duration of the test. The camera is then set to as short an exposure time as possible and triggered during the tunnel's run. The shortest exposure time of the camera is of the order of milliseconds effectively superimposing 1000 of the xenon flash lamp's images on top of each other which in turn averaged out the turbulent flow in the background of the images without compromising on the accuracy of the important flow features present.

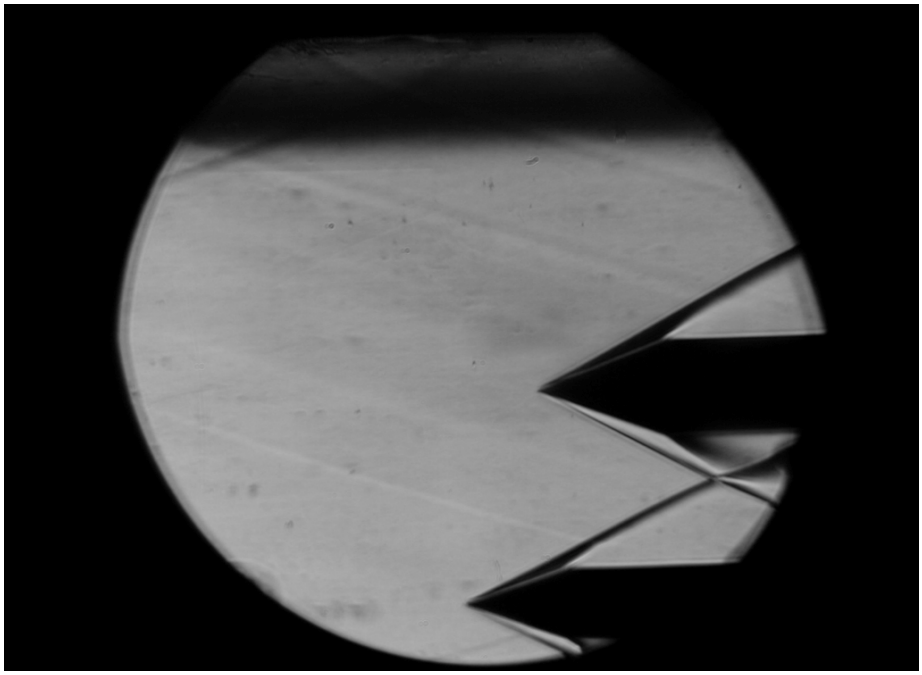


Figure A 3: Sample image from continuous projector lamp

A.3 July 2008

With the quality of the flow in the images deemed to be satisfactory, calibration of the wind tunnel was undertaken. By 'tripping up' the flow (simply utilising a piece of cello tape located on the floor of the test section, perpendicular to the axis of the SST) and creating a Mach line, the Mach number can be calculated by means of the Mach angle equation. The Mach number of the flow in the test section is varied by changing the size of the first throat via the sliding floor of the tunnel (see section 4.1.1 for full details). The throat was opened and closed by a predetermined value for each test and the resultant Mach number was plotted a function of the throat veeder counter value, generating a calibration curve.

During the calibration process the wind tunnel began to choke with an empty test section at a Mach number of around 2.18. This is considerably higher than the certified minimum operational value of

the wind tunnel (Mach 1.5). Owing to time constraints to have the wind tunnel operational for other work, a temporary operational range of Mach 2.5 – 3.4 was imposed upon the wind tunnel.

A.4 October 2008

Based on the erratic and unsatisfactory behaviour of the wind tunnel, it was decided that another internal inspection should be carried out. A faulty gasket seal between the settling chamber flange and the side walls of the tunnel was suspected as the cause of the premature choking of the test section. The gasket seal was removed and replaced. The floor of the wind tunnel had become quite pitted over the years due to various models separating from their mountings during tests. As a result of these pits, any images taken during a test would be littered by Mach lines and transverse waves. These pits were cleaned and sanded out, and then filled with aluminium filler and finally sanded down ensuring a smooth surface on the floor of the test section.

Upon re-assembly of the wind tunnel another Mach number – veeder counter calibration was carried out. As with the previous calibration, the wind tunnel choked prematurely, this time at a Mach number of 2.12 (compared with 2.18 for the calibration carried out in July 2008). Overall the calibration curves (see Figure A 4) from July and October 2008 bear a striking resemblance suggesting that the problem was not rectified with the installation of the new gasket.

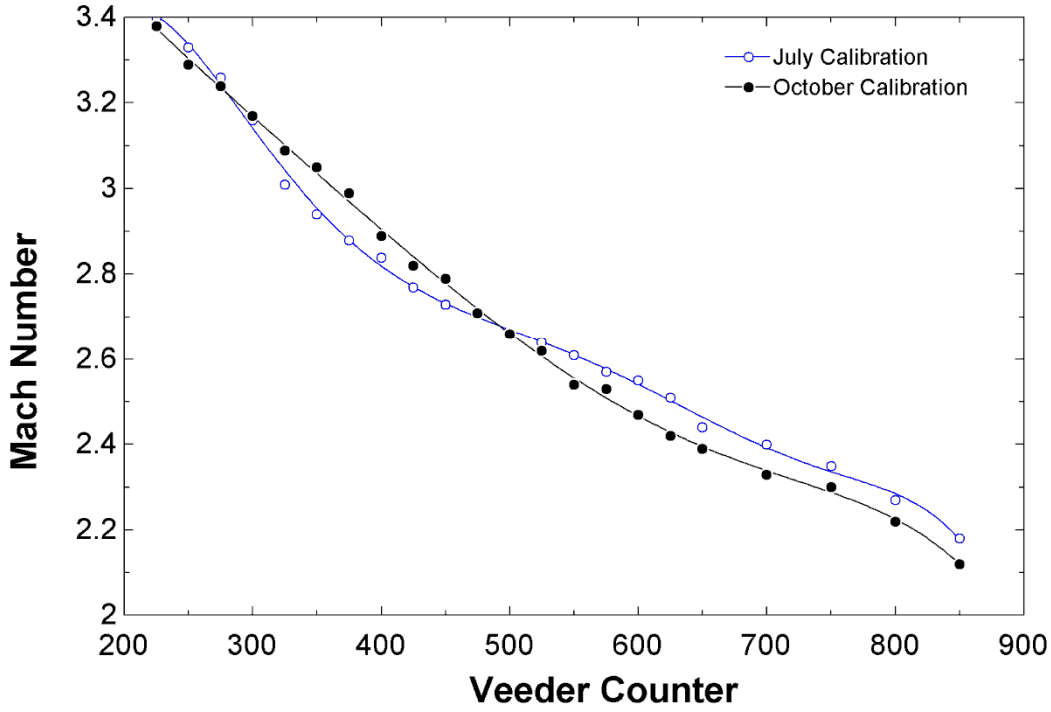


Figure A 4: Mach number – throat veeder counter calibration curves

An interesting point to note at this stage is that after the re-assembly test runs were conducted with the twin cone apparatus in situ, in addition to the calibration runs. Several anomalies were noted during these runs, the most significant of which being the pronounced vibration of the tunnel during a test. Furthermore, certain tests when the main air reservoir was full (1.5 MPa), at a Mach number of 3.2 the tunnel would operate normally and the flow through the test section would be supersonic. With the exact same geometry and the exact same Mach number set, however with the main air reservoir only at 1.2 MPa the tunnel would choke and test section would only be subsonic. For this reason it was suspected that the pressure control system was faulty.

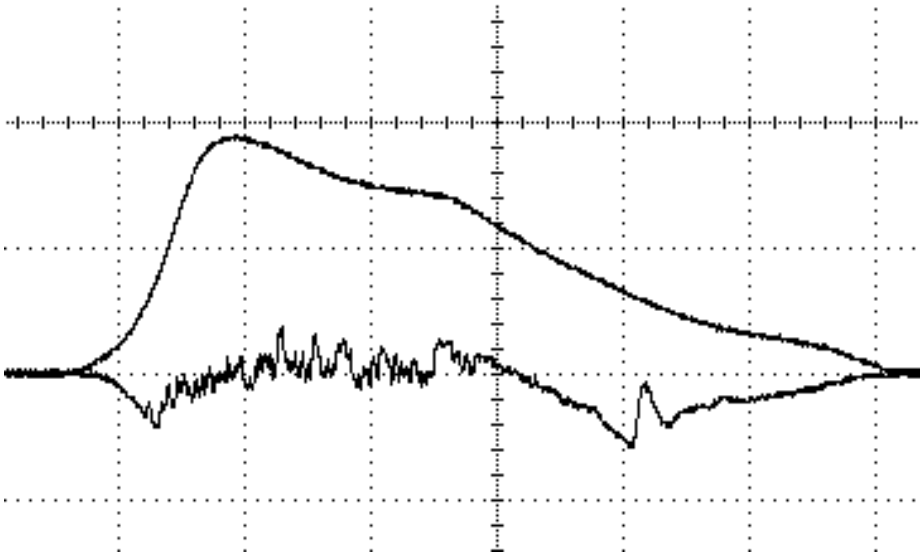


Figure A 5: Pressure trace from an unsuccessful test

Figure A 5 shows an unprocessed, unfiltered pressure trace from an unsuccessful test conducted after the re-assembly. As can be seen, the lower curve (representing the static pressure measured in the test section) fluctuates wildly instead of remaining constant over the duration of the test. This fluctuation (the cause of the tunnel vibration) supports the theory that the pressure control system is not operating correctly.

A.5 December 2008 – January 2009

Based on the inconsistency of the wind tunnel's operation it was decided that both the main valve (which sits immediately downstream of the main air reservoir) and the pilot valve (located immediately upstream of the expansion cone) should be examined. The function of the pilot valve is to maintain a constant pressure in the test section by governing the extent to which the main valve opens during a test (as explained in Section 4.1.1). A spare pilot valve, which was replaced in August 1992, was sent away for inspection and, if required, servicing, while the main valve was opened up

and examined internally. The integrity and operation of the main valve was found to be satisfactory with no visible signs of breakage of any of the main components. The pilot valve was returned by specialist without servicing and was reported as working normally.

A.6 March 2009

The pilot valve that was hitherto attached to the wind tunnel was replaced with the valve that had returned from the specialist. The resultant test runs displayed no significant changes from the previous runs conducted. It was therefore decided that either the pilot valve or the solenoids controlling the pilot valve should be replaced. According to original documentation, the 3-way safety solenoid valve (located at the main control valve) and the safety switch in situ were last replaced in early 1983, whereas the pilot valve was replaced in August 1992 (according to information from the wind tunnel's logbook) because of a constant pressure overshoot and oscillation during tests. Based on the relative ages of the components (the pilot valve and solenoids) it was decided that the solenoid valves should be replaced before the pilot valve. The specifications of the solenoid valves were noted from their data plates (see Table A 2 and Table A 3) and new valves sought.

Table A 2: Safety Solenoid Specifications (Circa 1982)

Manufacturer	Serial Number	Catalogue Number
ASCO	4275SA	8321A42A
Supply Voltage [V / Hz]	Power [W]	Differential Pressure [kPa]
220 / 50	6	70-1400
Pipe Diameter [in]	Orifice Size [mm]	
0.375	7	

Table A 3: Pilot Valve Solenoid Specifications

Manufacturer	Serial Number	Catalogue Number
ASCO	80823S	8320A103
Supply Voltage [V / Hz]	Power [W]	Differential Pressure [psi]
220 / 50	15.4	0-250
Pipe Diameter [in]	Orifice Size [mm]	
0.250	1.6	

Based on the age of the solenoids (manufactured in 1982) some of the specifications have changed on the replacement parts. These changes are minor and mostly confined to part/catalogue numbers and unit consistency (imperial to metric)

Table A 4: Solenoid Specifications (Circa 2009)

Manufacturer	Serial Number	Catalogue Number
ASCO	98527SA	SC B321A002
Supply Voltage [V / Hz]	Power [W]	Differential Pressure [kPa]
230 / 50	6	70-1400
Pipe Diameter [NPT]	Orifice Size [mm]	
3/8	7.1	

Table A 5: Pilot Valve Solenoid Specifications (Circa 2009)

Manufacturer	Serial Number	Catalogue Number
ASCO	98515SA	SC B320A182
Supply Voltage [V / Hz]	Power [W]	Differential Pressure [kPa]
230 / 50	11.2	0-1700
Pipe Diameter [NPT]	Orifice Size [mm]	
¼	1.6	

In addition to fitting the new solenoid valves the pilot valve was switched back to the newer unit since the older valve provided no tangible difference in the operation of the tunnel. The resulting tests showed no change in the pressure fluctuation, and the pronounced vibration of the wind tunnel persisted. Although no details (frequency, magnitude etc.) were given on the exact nature of the pressure oscillations that led to the replacement of the pilot valve in August 1992, it was thought to be a similar problem described above and hence the decision was made to replace the pilot valve.

A.7 August 2009

The replacement of the pilot valve returned to SST to (consistent) supersonic operations, however the excessive vibration noted at the start of each test persisted. Figure A 6 is a processed portion of a pressure trace showing the oscillation of the pressure in the settling chamber during the initial stages of the test. The portion in question is taken from the maximum value on the stagnation pressure rise.

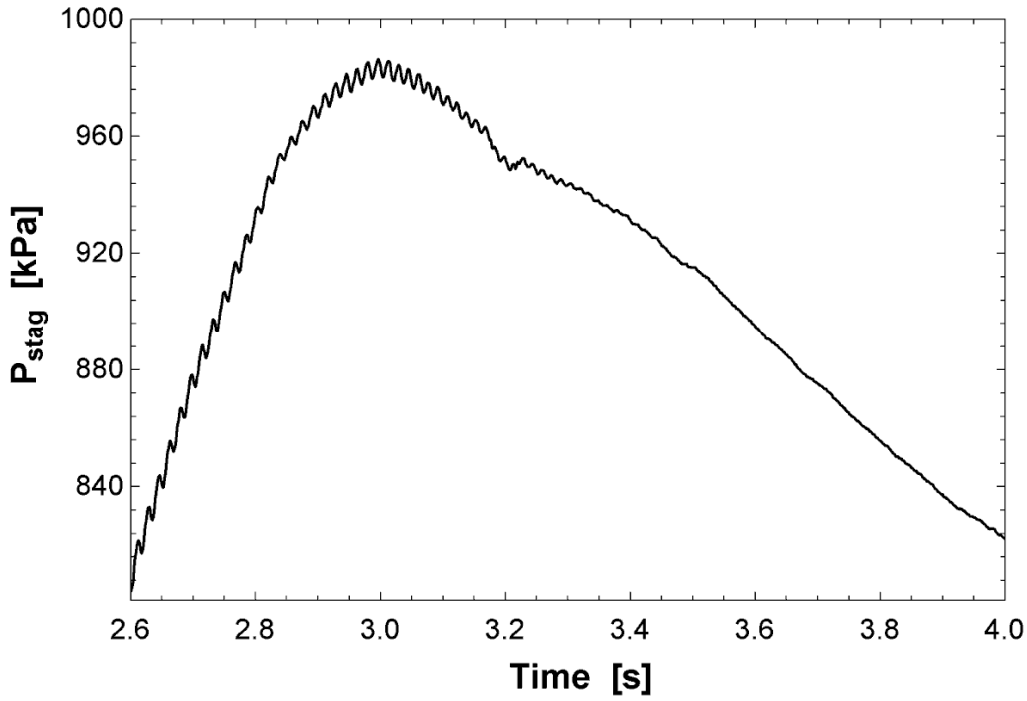


Figure A 6: Pressure trace showing vibration (August 2009)

The oscillation of the pressure in the settling chamber was thought to be caused by the main control valve attached to the pressure reservoir. The oscillations indicate that the valve may be 'sticking' when opening thus not providing a constant supply of air to the settling chamber and thus causing the SST to vibrate. An overhaul of the main valve was carried out by replacing several internal components within the valve itself. The details of the parts replaced in the overhaul are included in Table A 6.

Table A 6: Repair Kit Contents for Main Control Valve

Part Name	Material
Gasket	Non-Asbestos
Stem Nut	Steel
Disc	Stainless Steel
Seat Ring	Stainless Steel
Stem	Stainless Steel
HP Spring	Steel
Dowel Pin	Steel
Pressure Plate	Cast Iron
Diaphragm	Stainless Steel

A.8 December 2009

The installation of the repair kit rectified the oscillation detected in the settling chamber – a result verified by comparing the pressure traces pre- and post-repair kit installation (Figure A 6 and Figure A 7 respectively).

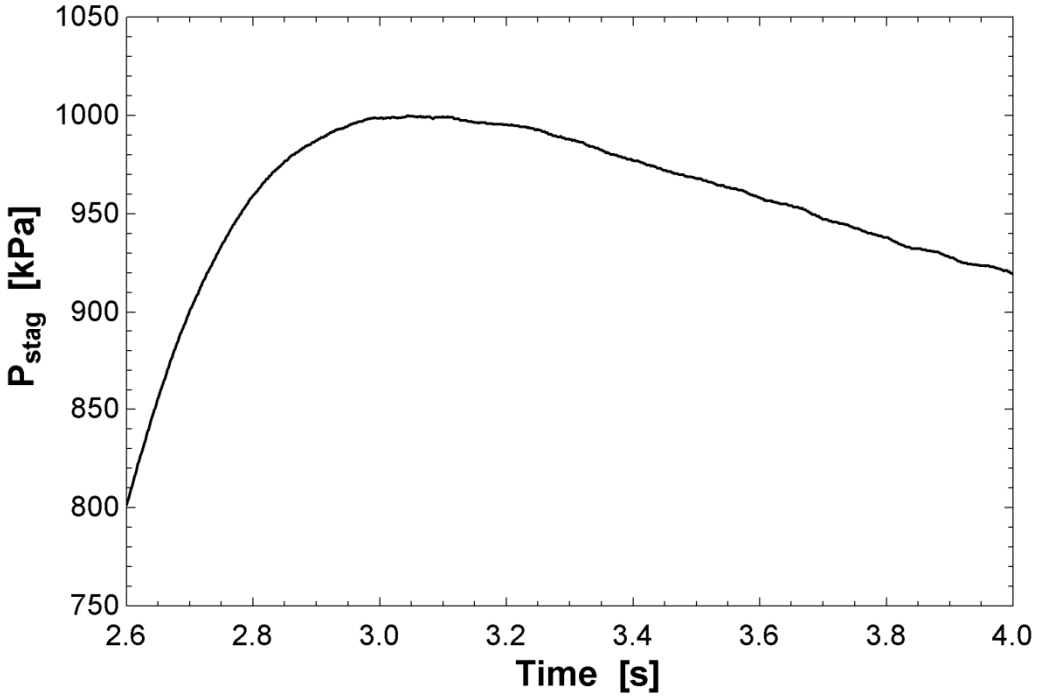


Figure A 7: Pressure trace showing vibration (December 2009)

By processing the data from the wind tunnel's pressure transducers, conditions inside the settling chamber and the test section can be observed. Figure A 8 shows the pressure variation throughout a successful test. The pressure in the settling chamber is seen to rise and fall smoothly, while the pressure in the test section remains almost perfectly constant over the duration of the entire blow-down, unlike the test run shown in Figure A 5. Using the pressure data the Mach and Reynolds numbers can be calculated (for the duration of a test) and are plotted in Figure A 9. The most noticeable features on this curve are the minimal variation of Mach number over time and the steady decrease in Reynolds number with time. Focussing on the latter, the shape of the Reynolds number curve in Figure A 9 compares favourably with that of the settling chamber pressure in Figure A 8 – an expected result given the dependence of the Reynolds number on the settling chamber pressure shown in equation [6.2].

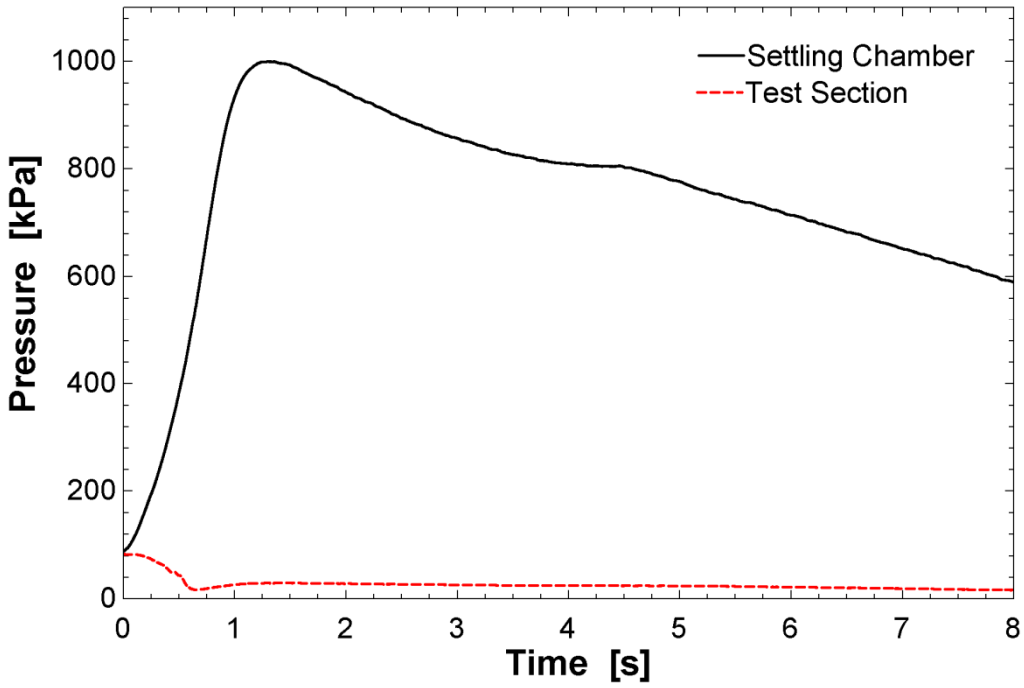


Figure A 8: Processed pressure trace from successful wind tunnel test, Mach 3.0

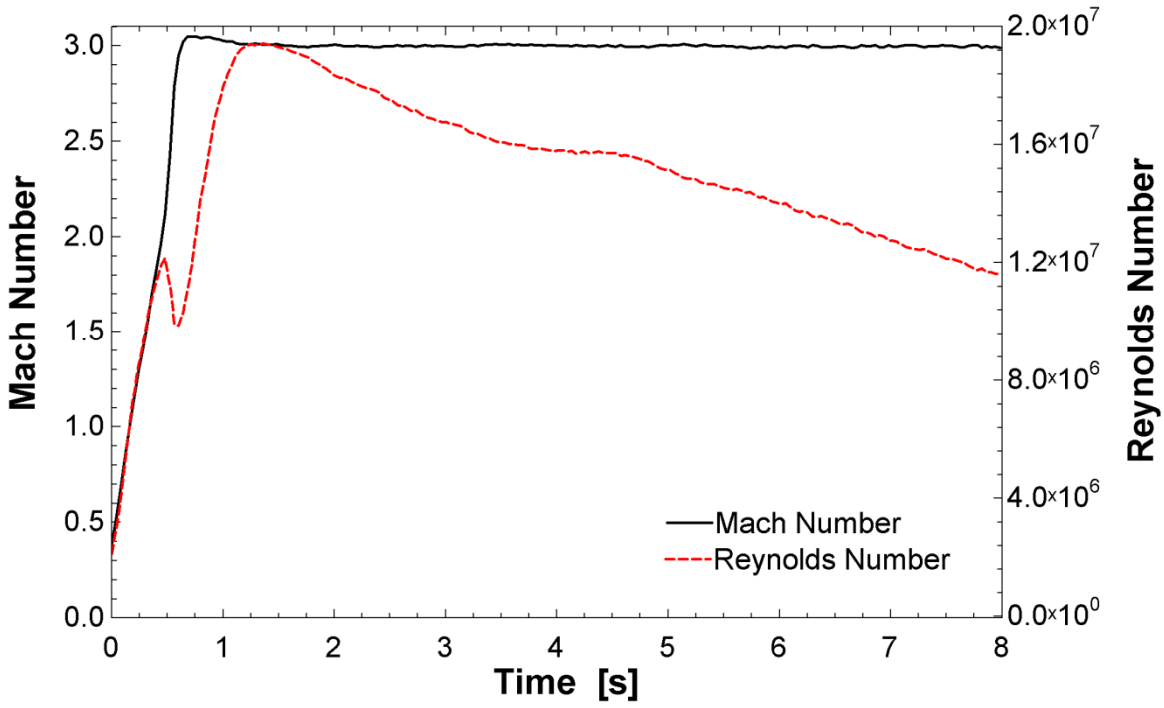


Figure A 9: Mach and Reynolds number variation during a wind tunnel test, Mach 3.0

A full veeder counter – Mach number calibration was not performed for the following reasons:

i. Selected veeder counter values were spot tested using the cello tape method explained previously. The results from these tests were found not to vary significantly from the previous calibration data (shown in Figure A 4).
ii. The processed pressure trace data showed strong agreement with the incumbent calibration data.

Appendix B: Derivations

All of the various symbols used for the various parameters in the following work are defined in the list of symbols at the beginning of this report.

B.1 Derivation of Wind Tunnel Mach Number

The following derivation will seek to relate the test section Mach number of the wind tunnel to the pressure values measured during a test (NACA ,1953), (Scott, 1994).

There exist two formulae for the definition of the stagnation enthalpy of a fluid:

$$h_T = h + \frac{1}{2}V^2 \qquad [B.1]$$

$$h_T = h + C_P\left(T_T - T\right) \qquad [B.2]$$

Combining these two equations:

$$\frac{1}{2}V^2 = C_P\left(T_T - T\right)$$

$$\therefore T_T = T + \frac{V^2}{2C_P}$$

But, for a perfect gas:

$$C_P = \frac{R\gamma}{\gamma - 1}$$

$$\therefore T_T = T + \frac{V^2\left(\gamma - 1\right)}{2\gamma R}$$

The equation for Mach number is:

$$M = \frac{V}{a}$$

Where $a = \sqrt{\gamma RT}$

$$\therefore M = \frac{V}{\sqrt{\gamma RT}} \rightarrow M^2 = \frac{V^2}{\gamma RT}$$

$$\frac{V^2}{\gamma R} = M^2 T$$

Substituting this last expression back into the equation for T_T:

$$T_T = T + \frac{(\gamma - 1)}{2} M^2 T$$
$$= T\left(1 + \frac{(\gamma - 1)}{2} M^2\right) \qquad \text{[B.3]}$$

Now, for an isentropic process:

$$\frac{P_T}{P} = \left(\frac{\rho_T}{\rho}\right)^{\gamma} \rightarrow \frac{\rho_T}{\rho} = \left(\frac{P_T}{P}\right)^{\frac{1}{\gamma}}$$

Combining this result with the equation of state:

$$\frac{\rho_T}{\rho} = \left(\frac{P_T}{P}\right)^{\frac{1}{\gamma}} = \frac{P_T}{P} \cdot \frac{T}{T_T}$$

$$\rightarrow \left(\frac{P_T}{P}\right)^{\frac{1-\gamma}{\gamma}} = \frac{T}{T_T}$$

$$\rightarrow \left(\frac{P_T}{P}\right)^{\frac{\gamma-1}{\gamma}} = \frac{T_T}{T}$$

$$\rightarrow \frac{P_T}{P} = \left(\frac{T_T}{T}\right)^{\frac{\gamma}{\gamma-1}}$$

Substituting this result into [B.3]:

$$\frac{P_T}{P} = \left(1 + \frac{(\gamma - 1)}{2} M^2\right)^{\frac{\gamma}{\gamma-1}} \qquad \text{[B.4]}$$

Finally, by manipulating and re-arranging equation [B.4] the relationship between pressures and Mach number is given:

$$M = \left(\frac{2}{\gamma - 1} \left[\left(\frac{P_T}{P} \right)^{\frac{\gamma - 1}{\gamma}} - 1 \right] \right)^{\frac{1}{2}} \qquad [B.5]$$

Equation [B.5] can now be used to convert the stagnation pressure in the settling chamber (P_T) and the static pressure in the test section (P), recorded during a test, into Mach number of the flow in the test section.

B.2 Derivation of Wind Tunnel Reynolds Number

The following derivation will seek to relate the test section Reynolds number of the wind tunnel to the pressure and temperature values measured during a test (NACA ,1953), (Scott, 1994).

The well known formula defining the Reynolds number of a flow is:

$$\mathrm{Re} = \frac{\rho V d}{\mu} \qquad [B.6]$$

Each of the terms of this equation must now be expanded to give an expression in terms of the pressures measured during a test. Starting with the density term, ρ , and using the perfect gas law:

$$\rho = \frac{P}{RT} \qquad [B.7]$$

The temperature term above can now also be expanded using the equations from the Mach number derivation above as follows:

$$\frac{T}{T_T} = \left(\frac{P_T}{P} \right)^{\frac{1-\gamma}{\gamma}}$$

$$\therefore T = T_T \left(\frac{P_T}{P} \right)^{\frac{1-\gamma}{\gamma}}$$

It is worthwhile noting at this stage that the stagnation temperature of the wind tunnel, T_T , can be approximated to be the ambient temperature in the storage vessel of the wind tunnel, T_A , giving:

$$T = T_A\left(\frac{P_T}{P}\right)^{\frac{1-\gamma}{\gamma}} \qquad [B.8]$$

Substituting this result back into equation [B.7]

$$\rho = \frac{P}{RT_A\left(\frac{P_T}{P}\right)^{\frac{1-\gamma}{\gamma}}}$$

$$\rightarrow \rho = \frac{P^{\frac{1}{\gamma}}}{RT_A P_T^{\frac{1-\gamma}{\gamma}}} \qquad [B.9]$$

$$\rightarrow \rho = \frac{P^{\frac{1}{\gamma}} P_T^{\frac{\gamma-1}{\gamma}}}{RT_A}$$

For velocity, V, the Mach number relationship can be used to give:

$$V = M\sqrt{\gamma RT}$$

Substituting the results of equations [B.5] and [B.8] into the above equation:

$$V = \left[\frac{2}{\gamma-1}\left(\left(\frac{P_T}{P}\right)^{\frac{\gamma-1}{\gamma}} - 1\right)\right]^{\frac{1}{2}} \times \sqrt{\gamma R} \times \left[T_A\left(\frac{P_T}{P}\right)^{\frac{1-\gamma}{\gamma}}\right]^{\frac{1}{2}}$$

$$= \left[\left(\frac{2\gamma RT_A}{\gamma-1}\right)\left(\left(\frac{P_T}{P}\right)^{\frac{\gamma-1}{\gamma}} - 1\right)\left(\frac{P_T}{P}\right)^{\frac{1-\gamma}{\gamma}}\right]^{\frac{1}{2}} \qquad [B.10]$$

The value for d in the equation for Reynolds number is a constant (with respect to pressure and temperature) and therefore all that remains is the relationship for the viscosity of the fluid (μ). The function that relates the viscosity and temperature for air is given by the following equation:

$$\frac{\mu_2}{\mu_1} = \left(\frac{T_2}{T_1}\right)^{\frac{3}{4}}$$

$$\rightarrow \frac{\mu}{\mu_0} = \left(\frac{T}{T_1}\right)^{\frac{3}{4}}$$

Where the value for μ in air at $T_1 = 0°C = 273\,\text{K}$ is $\mu_0 = 1.714 \cdot 10^{-5}$ $\text{kgm}^{-1}\text{s}^{-1}$. Substituting the above equation into [B.8] for temperature:

$$\mu = \mu_0 \left(\frac{T_A \left(\frac{P_T}{P}\right)^{\frac{1-\gamma}{\gamma}}}{T_1} \right)^{\frac{3}{4}} \qquad [B.11]$$

$$= \mu_0 T_A^{\frac{3}{4}} \left(\frac{P_T}{P}\right)^{\frac{3(1-\gamma)}{4\gamma}} T_1^{-\frac{3}{4}}$$

At this stage all of the parameters for Reynolds number are now in terms of pressures and constants, therefore equations [B.9], [B.10] and [B.11] may be substituted into equation [B.6]. Combining and then reducing the resultant formula then gives:

$$\text{Re} = \frac{P^{\frac{5-\gamma}{4\gamma}} P_T^{\frac{5(\gamma-1)}{4\gamma}} d T_1^{\frac{3}{4}}}{\mu_0 T_A^{\frac{5}{4}}} \times \left[\left(\frac{2\gamma}{R(\gamma-1)} \right) \times \left(\left(\frac{P_T}{P}\right)^{\frac{\gamma-1}{\gamma}} - 1 \right) \right]^{\frac{1}{2}} \qquad [B.12]$$

Equation [B.12] can now be used to calculate the free stream Reynolds number of the flow in the test section of the wind tunnel during a blow down, by recording only the stagnation pressure in the settling chamber (P_T) and the static pressure in the test section (P). The other required parameters are the reference length (d) and the ambient temperature (T_A) - both of which remain constant throughout the duration of a test. All the other terms are constant and are given.

Appendix C: Test Model Manufacturing Drawings

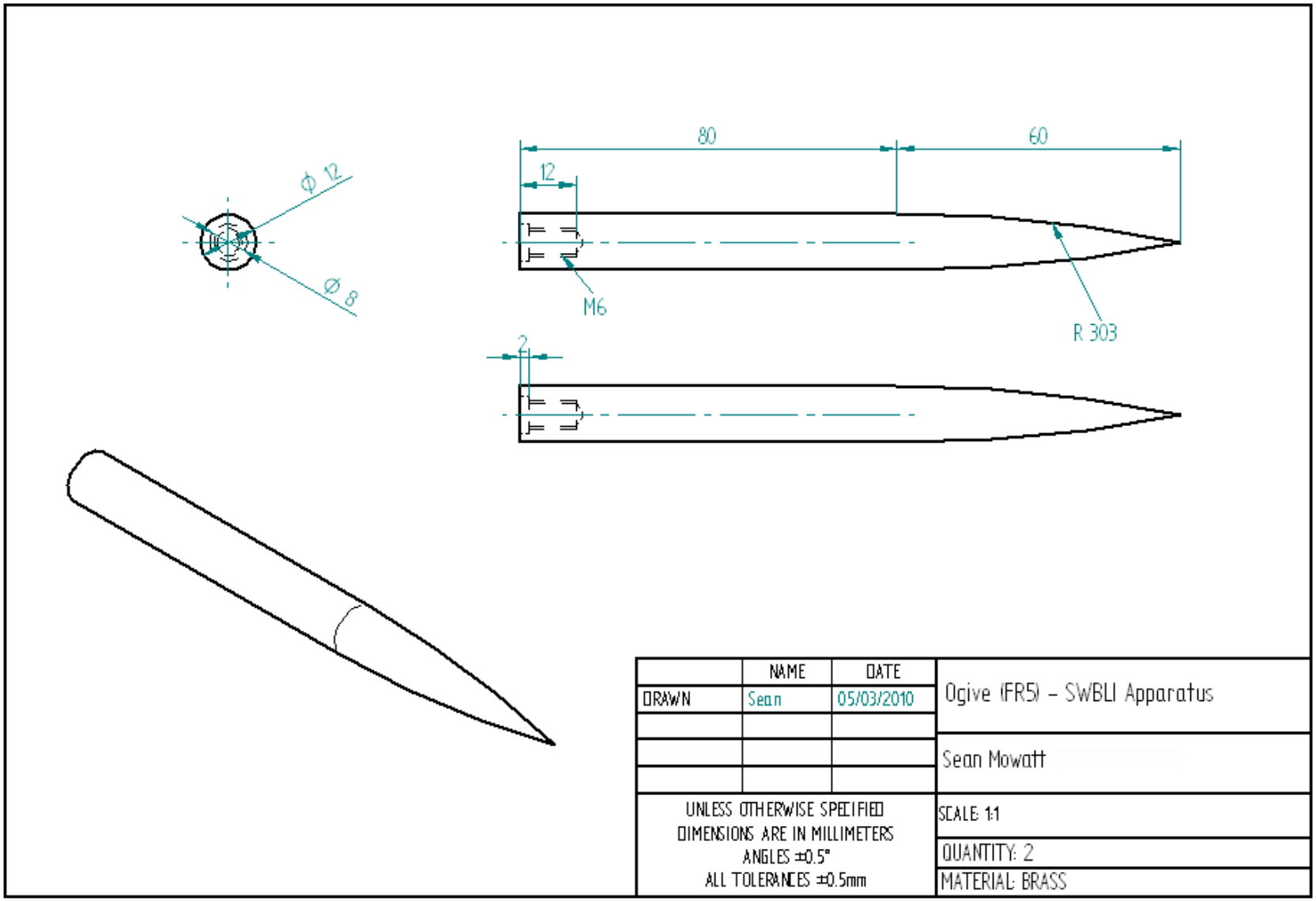


Figure C 1: Manufacturing drawings for the ogival SWBLI generator

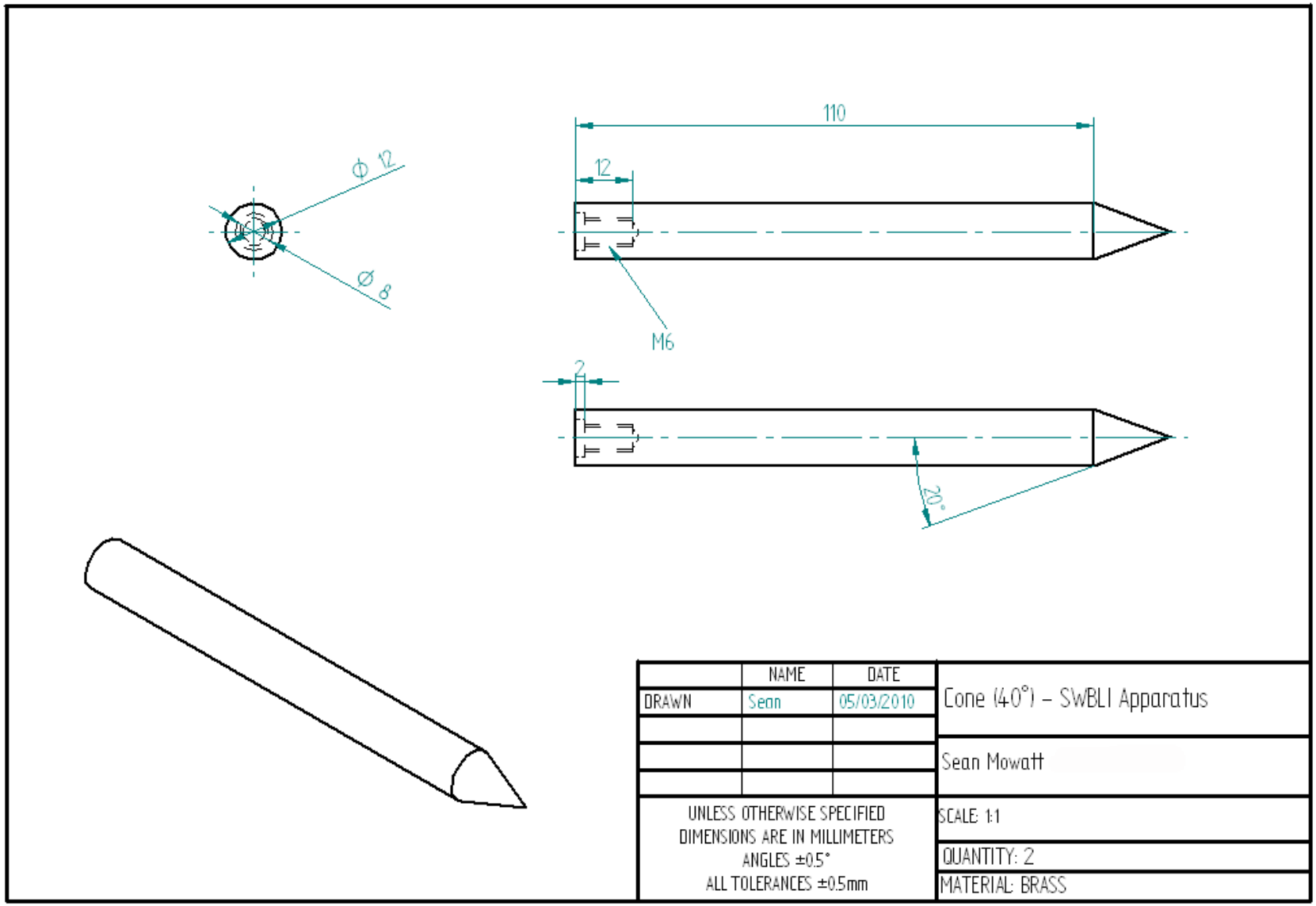


Figure C 2: Manufacturing drawings for the conical SWBLI generator

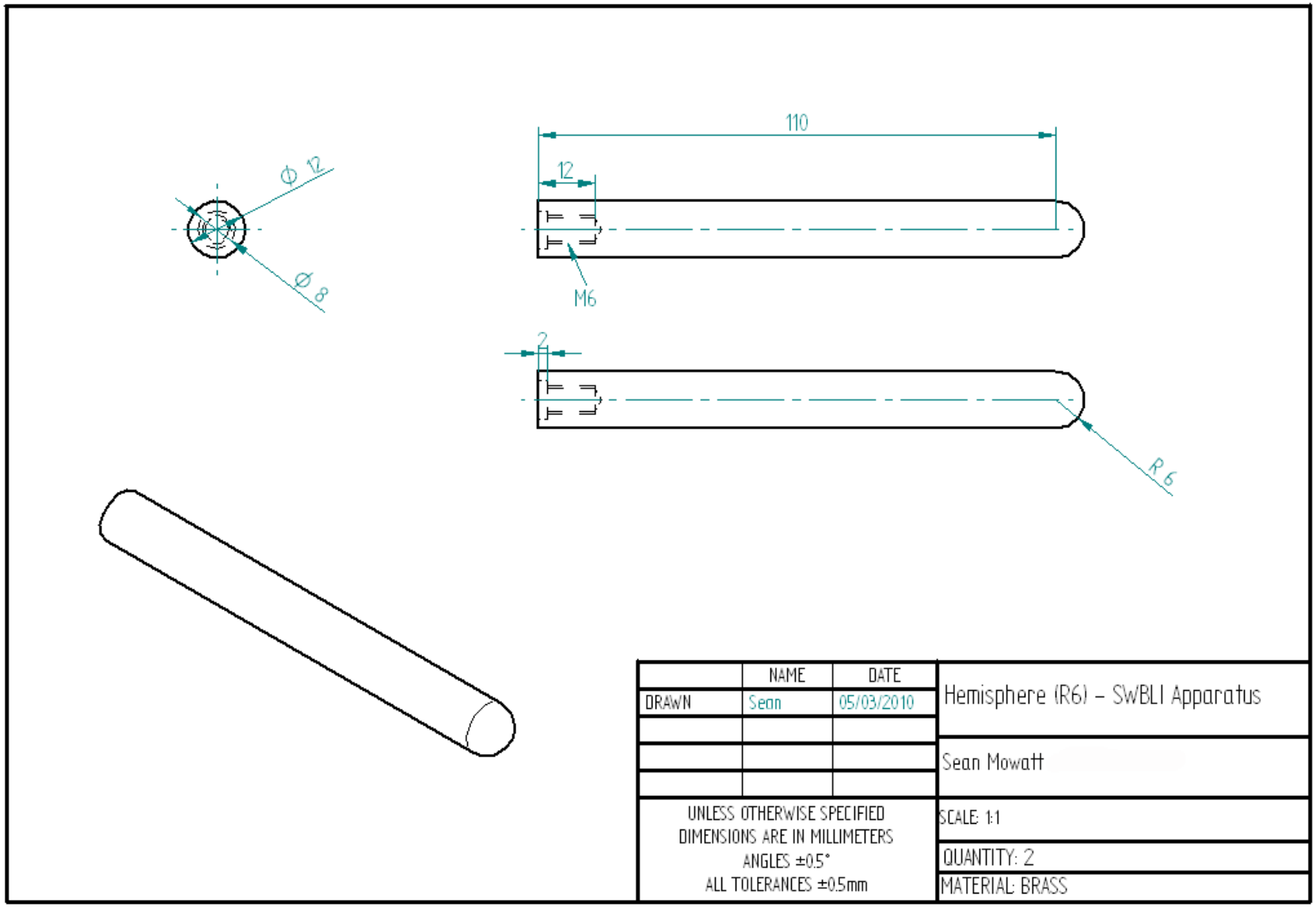


Figure C 3: Manufacturing drawings for the hemispherical SWBLI generator